12-2017

Angle-Resolved Observation of X-Ray Second Harmonic Generation in Diamond

Björn Senfftleben
University of Nebraska-Lincoln, bjoern.senfftleben@huskers.unl.edu

ANGLE-RESOLVED OBSERVATION OF X-RAY SECOND HARMONIC GENERATION IN DIAMOND

by

Björn Senfftleben

A THESIS

Presented to the Faculty of

The Graduate College at the University of Nebraska

In Partial Fulfilment of Requirements

For the Degree of Master of Science

Major: Physics & Astronomy

Under the Supervision of Professor Matthias Fuchs

Lincoln, Nebraska

December, 2017

ANGLE-RESOLVED OBSERVATION OF X-RAY SECOND HARMONIC GENERATION IN DIAMOND

Björn Senfftleben, M.S.

University of Nebraska, 2017

Adviser: Matthias Fuchs

This thesis reports angularly-resolved observation of X-ray second harmonic generation (XSHG) in diamond at several phase-matching geometries. The XSHG signal was produced by ultra-short, highly intense X-ray pulses with a photon energy of 9.831 keV generated by a free-electron laser. In some geometries for high pulse energies more than 10 second harmonic photons per pulse were generated.

Different phase-matched geometries were used for XSHG to investigate the angular dependence of the efficiency of the process. Furthermore, for each phase-matching condition, the quadratic dependence for second harmonic generation at each geometry was verified and the crystal rocking curves were measured. The results for the angular dependence of the efficiency are in good agreement with the theory as shown by simulations (done by Priyanka Chakraborti).

Improved interpretations of the data are enabled by a new analysis algorithm (developed within the framework of this thesis) that interprets the detected photon signal using a deeper understanding of the used 2D detector. Further an extensive analysis on established interpretation methods is presented.

ACKNOWLEDGMENTS

I would like to thank all who contributed to this project and all who supported me and my work. You enabled me to accomplish my goals in this project and to finish this thesis.

Special thanks are due to my adviser, Prof. Matthias Fuchs, who provided excellent support while giving me much freedom in my work. I value the many, often long and intense, discussions that drove the project forward, step by step. When I needed his advice, he was there. Especially, I want to thank him for the quick corrections and feedback in the final phase of the thesis and particularly in the very last hours and days before the thesis was due. Furthermore, he enabled me to gather additional experience by participating in two more beamtimes at the Linac Coherent Light Source. I had a great time working with him.

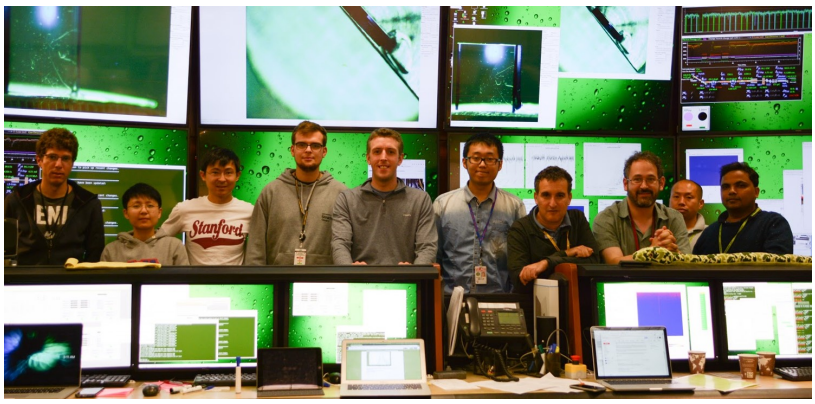

Figure 1: The team that conducted and enabled the experiment. On the photo from left to right: C. Weninger, Y. Sun, D. Zhu, B. Senfftleben, B. Kettle, H. Liu, S. Shwartz, D. Reis, T. Sato and S. Ghimire; Not on the photo: M. Fuchs, S. Teitelbaum, P. Bucksbaum, J. Hastings, S. Nelson, M. Trigo, J. Defever and G. Carini;

I also want to thank all people that conducted and enabled the experiment. Their knowledge and their helpfulness allowed me to understand many details of the experimental setup, to gain some more in-depth understanding crucial for the data analysis

and to resolve many issues raised within that project. Special thanks go to Silke Nelson and Dilling Zhu for their support with their knowledge and with the discussions we had during the period after the conduction of the experiment. That beamtime was a highlight, not only concerning this project, but concerning the whole time I spent in the USA.

I want to thank Priyanka Chakraborti for her excellent work and all the effort she put into writing simulations for the X-ray second harmonic process. Her work made it possible to provide a direct comparison to theory while completing the thesis within this Fall term.

I want to thank Andreas Kaldun and Daniela Rupp for their support and feedback for this thesis.

I thank my friends who assisted me not only with my written English. I would like to thank them for their fast and helpful feedback. They also gave me a great time being abroad in the United States, far away from home.

Last but not least, I also want to thank my family who encouraged me from the beginning with my plans to study in the U.S. and supported me and my ideas at all times. They empower me to work hard to achieve my goals.

Table of Contents

Chapter 1

Introduction

Nowadays, extremely intense and ultra-short X-ray pulses are used to push the frontiers in many research fields, such as femtochemistry [37], nonlinear spectroscopy [39], time-resolved ultra-fast dynamics [43], novel high-resolution imaging methods [26, 13]. These advances are enabled by X-ray free electron lasers (XFELs) that have become available at the beginning of this millennium. XFELs provide extremely intense, extremely short and coherent light pulses at Angstrom wavelengths. Some methods and effects that were developed and observed at XFELs are often extensions from previously known regimes.

For a long time, optical effects were assumed to be linear. Due to the invention of the laser [33], the field of nonlinear optics experienced a rapid development. The first observed non-linear effect using a laser was second harmonic generation [23]. The intensities in the optical regime available after the invention of the laser required an extension of the so far known theories. Only a decade after the first demonstration of nonlinear effects in the optical regime, the first non-linear effect in the X-ray regime, namely parametric down conversion (PDC), was demonstrated by Eisenberger and McCall in 1970 [21] (proposed by Levine and Freund in 1969 [32]). The limited x-ray intensity of classical light sources lead to a photon rate of only one per hour. Other effects could only be investigated theoretically. Later, synchrotron radiation allowed

the measurement of PDC with much higher precision, but the generated intensity of a synchrotron is still too low to cause other non-linear effects in the X-ray regime.

Today, such effects can be demonstrated in the hard X-ray regime using XFELs [24, 25, 46]. Moreover, it is of interest to explore new accessible parameter spaces and to study their behaviour in the nonlinear regime. Those experiments test existing theory and investigate whether limits of currently applied physical models can be found. For instance, an experiment, studying non-linear Compton scattering in the hard X-ray regime showed an unexpected red shift, indicating such limits of current models [24].

While X-ray second harmonic generation in a diamond has been observed before [46], in this thesis that process has been explored further. The angular dependence of the process was investigated. This allows insights into the microscopic details of the nonlinear mechanism.

To achieve an optimized precision in the number of measured second harmonic photons, different algorithms for automated interpretation of the 2D pixel detector data were analyzed. A new algorithm has been developed. It takes conceivable and ambiguous signal distributions due to a single photon hit on the pixel detector into account. In particular, for higher pulse energies, a considerable improvement of the data interpretation has been demonstrated.

The experimental results show good agreement with the theory [51]. An angular dependency of the efficiency for pulse energies of $70 \pm 20\,\mu J$ shows good overlap with simulated data (simulation by Priyanka Chakraborti). The quadratic dependence of generated second harmonic photon rate on the incident pulse energy was confirmed. Furthermore, crystal rocking curves are presented.

Chapter 2

Theory

2.1 Nonlinear Optics

2.1.1 Introduction

The propagation of light can be described using the wave equation derived from Maxwell's equations. In vacuum, the wave equation can be written in terms that depend only on the electric field $\boldsymbol{E}(\boldsymbol{r}, t)$ as a function of space $\boldsymbol{r}$ and time t. The presence of matter leads to additional source terms, making it also dependent on the matter's properties, e.g. polarization [15]. For simplicity in the first part of this chapter (ch. 2.1), the fields are described in only one dimension using plane waves.

$$\frac{\partial^2 E(r,t)}{\partial r^2} - \frac{1}{c^2}\frac{\partial^2 E(r,t)}{\partial t^2} = \frac{1}{\epsilon_0 c^2}\frac{\partial^2 P(r,t)}{\partial t^2} \tag{2.1}$$

Here c is the vacuum speed of light and ϵ_0 is the vacuum permittivity. Upon performing a Taylor expansion of P, it becomes clear that for common electric fields, only the first term shows significant contribution and higher order terms can be neglected. Under more extreme electric fields, like those generated by a laser, higher order terms may become relevant. Those depend non-linearly on the electric field, as can be seen from the Taylor expansion.

$$P(t) = \sum_{n=1}^{\infty} P_n(t) = \sum_{n=1}^{\infty} \chi^{(n)} E(t)^n \tag{2.2}$$

In that expansion, the electric susceptibility $\chi^{(n)}$ expresses the material's properties. There can be materials promoting higher order terms, yielding non-linear effects.

2.1.2 Non-linear properties in materials

Polarization is a material property, which for light-matter interactions is a rapid varying parameter, as it depends on the frequency of the light, the electric field and the magnetic field acting within the material. For wavelengths in the nanometer regime, the influence of the magnetic fields can be neglected in the linear regime. This assumption yields the expression of its material specific properties with regard to equation 2.2 in the electric susceptibility. In the following section the physical cause for this will be described using a classical approach with scalar fields for simplicity, following ref. [14].

The electric susceptibility can be derived using the classical Lorentz model for the atom, as e.g. shown in [12]. The same approach is used here. In the Lorentz model, when the material is not exposed to external fields, the electrons of a material are in an equilibrium state with the atomic cores; they are located in the minimum of the atomic potential. In the linear regime, the electron's behavior in the presence of a rapidly changing electric field can be modeled using a damped driven harmonic oscillator. The driving force occurs due to the electric field. In the non-linear regime, the potential U needs to be extended with an-harmonic (higher order) terms. This leads to a restoring

force $F_{restoring}$ in the oscillator that contains non-linear components:

$$F_{restoring} = \frac{dU}{dx} = -m\omega_0^2 x - m\sum_{i=2}^{n} a_i x^i \tag{2.3}$$

The atomic potential U represents an important property of a material. One important classification of materials is to differentiate between those with a centrosymmetric ($U(x) = U(-x)$) and those with a non-centrosymmetric potential. This is because due to symmetry arguments, centrosymmetric materials cannot exhibit terms of even order in the restoring force, which leads to non-zero $\chi^{(n)}$ terms of only odd order n in the polarization P.

The equation for an an-harmonic oscillator (e.g. for a non-centrosymmetric medium: $\frac{d^2x}{dt^2} + 2\gamma\frac{dx}{dt} + m\omega_0^2 x + a_2x^2 = -\frac{e}{m}E(t)$ [14]) can be solved using perturbation theory (see [14]). In the Lorentz model, the polarization for each order i is described by

$$P_i = -Nex^{(i)} \tag{2.4}$$

where N is the number of electrons. Using this description and the relation of P and the susceptibility shown before, each existing order $x^{(i)}$ corresponds to a non-zero value of P_i.

2.1.3 Second Harmonic Generation (SHG)

Second harmonic generation (SHG) is one of the best understood non-linear optical effects. It is a second order effect and it may arise, as it will be shown at first in this section, from a quadratic dependence of the polarization on the electric field. Hence applying the theory presented up to this point, this effect can only be observed in non-centrosymmetric media. Such a medium is considered in the following derivations.

Considering only terms up to second order, first order effects are still present but known not to lead to second harmonic generation. Thus only the nonlinear component will be considered here. In the following, the incident waves are approximated with plane waves, where $\tilde{E} = \hat{E}e^{i\boldsymbol{kr}}$ represents the part of the electric field that contains the amplitude $\hat{E}$ and spatial dependence $e^{i\boldsymbol{kr}}$ of the field, where $\boldsymbol{k}$ is the wave vector. The second-order polarization is then

$$P_2(t) = \chi^{(2)}E(t)^2 = \chi^{(2)}\left[\tilde{E}e^{-i\omega t} + c.c.\right]^2 \tag{2.5}$$

which leads to

$$P_2(t) = \chi^{(2)}\left[\tilde{E}^2 e^{-i(2\omega)t} + \tilde{E}^{*2}e^{i(2\omega)t} + 2\left|\tilde{E}\right|^2\right]. \tag{2.6}$$

The resulting polarization shows an oscillating term at twice the frequency of the incident beam and a constant term. For second harmonic generation only the oscillating part of of the equation is of relevance:

$$P_{2\omega}(t) = \chi^{(2)}\left[\tilde{E}^2 e^{-i(2\omega)t} + c.c.\right] \tag{2.7}$$

From the wave equation, shown in eq. 2.1 can be seen that the polarization term oscillating with twice the frequency leads to the generation of a second harmonic field.

But this is not the only possible approach to generate second harmonic signal. The case presented up to this point relies on the assumption that the effects due to the magnetic field can be neglected and that the radiation originates from an oscillating dipole term. It can be shown that second harmonic generation in centrosymmetric media is possible. The effect was demonstrated in 1962 in calcite [50] and a detailed theoretical description was given later that year by Bloembergen [11]. Though, second

harmonic generation in centrosymmetric media is several orders of magnitude weaker than that in non-centrosymmetric media.

2.1.4 Nonlinear Optical Effects in the X-ray regime

Since in the X-ray regime the frequency of the electric and magnetic fields are approximately four orders of magnitude higher than for fields in the visible range, the main contribution to parametric nonlinear effects are not based on anharmonicities of the atomic potential. This argument can be shown by making order of magnitude estimations for the required intensities to see the effect in a single atom, as it will be done in this section. The first part will show an approach that is explained in [14].

In this order of magnitude estimation, the required fields for the second order polarization to be on the same order of magnitude as the first order (linear) polarization.

In the visible regime (non-resonant), where the atomic resonant frequency ω_0 is much larger than ω, it will be fulfilled ca. with an electric field on the order of the characteristic atomic electric field strength $E_{at} = \frac{e}{a_0^2} \approx 6 \times 10^{11} \frac{V}{m}$. [14] This field leads to an order of magnitude estimation for the required intensity of:

$$I_{at} = |\langle \boldsymbol{S}_{at} \rangle_t| = \frac{\epsilon_0 c}{2} E_{at}^2 \approx 5 \times 10^{20} \frac{W}{m^2} = 5 \times 10^{16} \frac{W}{cm^2} \tag{2.8}$$

To make such an order of magnitude estimation for the X-ray regime, the scaling of the electric susceptibility with ω is considered. The needed relations can be derived using the approach from section 2.1.2 as it is presented in [14]. In the following, relations are given for second harmonic generation. The resulting order of magnitude

may be also valid for other second order nonlinear X-ray effects.

$$\chi^{(1)} \approx \frac{N\frac{e^2}{m}}{D(\omega)} \qquad D(\omega) = \omega_0^2 - \omega^2 - 2i\omega\gamma \tag{2.9}$$

$$\chi^{(2)} \approx \frac{N\left(\frac{e^2}{m^2}\right)a}{D(2\omega)D^2(\omega)} \tag{2.10}$$

In contrast to the optical regime, in the hard X-ray regime the atomic resonant frequencies are much smaller than those of the incident radiation: $\omega_0 << \omega$. Hence the equations shown before can be approximated to

$$\chi^{(1)} = -\frac{N\frac{e^2}{m}}{\omega^2} \qquad \chi^{(2)} = -\frac{N\left(\frac{e^2}{m^2}\right)a}{4\omega^6} \tag{2.11}$$

Now, by applying the same approach used for the optical regime and assuming that the order of magnitude of linear and first non-linear term have to be similar, an estimation for the required field can be made. From this the frequency scaling of the required electric field can be estimated as

$$\chi^{(1)}(\omega)E_{xray} \approx \chi^{(2)}(\omega)E_{xray}^2 \quad \Rightarrow \quad E_{xray} \approx \frac{\chi^{(1)}(\omega)}{\chi^{(2)}(\omega)} \sim \omega^4 \tag{2.12}$$

for a photon energy of 10 keV. The photon energy is at the order of 1 eV for the optical regime. Now, the estimated electric field and field's scaling with the photon energy are known. The required order of magnitude for the incident electric field in the X-ray regime can be estimated

$$E_{xray} \approx E_{at} \cdot (10000)^4 \sim 10^{27}\frac{V}{m}. \tag{2.13}$$

Also here the required intensity can be estimated

$$I_{xray} = \left|\langle \boldsymbol{S}_{xray} \rangle_t\right| = \frac{\epsilon_0 c}{2} E_{xray}^2 \sim 10^{54} \frac{W}{m^2} = 10^{50} \frac{W}{cm^2}. \tag{2.14}$$

Even the most advanced and brilliant hard X-ray sources in the world today, XFELs, are far from reaching such intensities [28]. As a result, the required regimes of intensity to observe second harmonic generation in the X-ray range only due to an-harmonic atomic potential effects are out of reach.

So instead of establishing as a driving force F_{drive} only one caused by the electric field, we can also include the magnetic field. This may give rise to observable effects with current technology.

$$F_{drive} \approx -\frac{e}{m}\boldsymbol{E} \quad \Longrightarrow \quad F_{drive} = -\frac{e}{m}\left(\boldsymbol{E} + \frac{d\boldsymbol{r}}{dt} \times \boldsymbol{B}\right) \tag{2.15}$$

As it was shown, an-harmonic terms in the Lorentz model can be neglected for hard X-rays at currently available intensities.

$$\frac{d^2\boldsymbol{r}}{dt^2} + 2\gamma\frac{d\boldsymbol{r}}{dt} + \omega_0^2\boldsymbol{r} = -\frac{e}{m}\left(\boldsymbol{E} + \frac{d\boldsymbol{r}}{dt} \times \boldsymbol{B}\right) \tag{2.16}$$

Due to the high X-ray photon energy, which is well above the binding energy of most materials (those with a low atomic number), and high X-ray frequency, which is well above the critical plasma density (for solids), the electrons can be approximated to be quasi-free. Thus the solid can be approximated as a collision-less plasma. For ultrafast femtosecond pulses, the ions can be approximated as stationary, a "frozen" ion.

Hence the dampening term, as well as the influence of the atomic potential on the electrons, can be neglected:

$$\frac{d^2\boldsymbol{r}}{dt^2} = -\frac{e}{m}\left(\boldsymbol{E} + \frac{d\boldsymbol{r}}{dt} \times \boldsymbol{B}\right) \tag{2.17}$$

2.1.5 SHG in the X-ray regime

In the following sections the current induced by the EM-wave is derived. The derivation is first shown for a single charge and then for a charge distribution. The current density is the time-derivative of the polarization, and is a source term in the wave equation. Later the concepts of phase matching and the coupled field equations are introduced. All results, as done before, are derived using classical approaches.

The first parts of this section will follow the concepts of [45, ch. 1.4].

A single free electron as a source for SHG

To determine solutions for $\boldsymbol{r}$ with eq. 2.17, the electric and magnetic fields must first be described. The incident wave is approximated to be a plane wave. The fields of an incident plane wave are given by

$$\boldsymbol{E}(\boldsymbol{r}) = \boldsymbol{E}_+(\boldsymbol{r}) + \boldsymbol{E}_-(\boldsymbol{r}) = \tilde{\boldsymbol{E}}_+ e^{-i\omega t} + \tilde{\boldsymbol{E}}_- e^{i\omega t} = \hat{\boldsymbol{E}}_+ e^{i(\boldsymbol{k}\boldsymbol{r}-\omega t)} + \hat{\boldsymbol{E}}_- e^{-i(\boldsymbol{k}\boldsymbol{r}-\omega t)} \tag{2.18}$$

$$\boldsymbol{B}(\boldsymbol{r}) = \sqrt{\mu\epsilon}\,\frac{\boldsymbol{k} \times \boldsymbol{E}(\boldsymbol{r})}{k} = \frac{1}{c_m}\frac{\boldsymbol{k} \times \boldsymbol{E}(\boldsymbol{r})}{k} \quad [30, ch.7] \tag{2.19}$$

with the speed of light in matter c_m, the permeability μ, the permittivity ϵ and the wave vector $\boldsymbol{k}$. Both the magnetic and electric fields are a first order perturbation to the equilibrium state of the charge. Due to the Lorentz force in eq. 2.17 it becomes clear that the forces act as a first order perturbation for the electric field. Furthermore, the equation shows that the second term is much smaller than the first term since $v/c_m << 1$. Hence the force due to the magnetic field can be considered

to be a second order perturbation. [45, ch. 1.4].

Approaching equation 2.17 this way, it can be rewritten:

$$\frac{d^2\boldsymbol{r}}{dt^2} = \boldsymbol{A}_1 + \lambda \frac{d\boldsymbol{r}}{dt} \times \boldsymbol{A}_2 \tag{2.20}$$

with

$$\boldsymbol{A}_1(\boldsymbol{r}) = -\frac{e}{m}\boldsymbol{E} \quad \text{and} \quad \boldsymbol{A}_2(\boldsymbol{r}) = -\frac{e}{m}\boldsymbol{B} \tag{2.21}$$

A series expansion of $\boldsymbol{r}$ in terms of λ can be made:

$$\boldsymbol{r} = \boldsymbol{r}^{(0)} + \lambda \boldsymbol{r}^{(1)} + \lambda^2 \boldsymbol{r}^{(2)} + ... \tag{2.22}$$

It is to be noted that $\boldsymbol{r}^{(0)}$ describes the electrons position in equilibrium without any external fields present. So it describes the static state:

$$\frac{d\boldsymbol{r}^{(0)}}{dt} = 0 \qquad \& \qquad \frac{d^2\boldsymbol{r}^{(0)}}{dt^2} = 0 \tag{2.23}$$

Introducing this expansion to equation 2.20 and separating it into multiple equations by comparing coefficients for each order of perturbation n, an equation for $\boldsymbol{r}^{(n+1)}$ can be found:

$$\frac{d^2\boldsymbol{r}^{(1)}}{dt^2} = \boldsymbol{A}_1(\boldsymbol{r}^{(0)}) \tag{2.24}$$

$$\frac{d^2\boldsymbol{r}^{(2)}}{dt^2} = \frac{d\boldsymbol{r}^{(1)}}{dt} \times \boldsymbol{A}_2(\boldsymbol{r}^{(0)}) \tag{2.25}$$

The fields are approximated to oscillate around their initial position on the static coordinate, since the displacement of the charge due to the incident field will be small. (As motivated by the order of magnitude estimation in ch. 2.1.4)

By solving eq. 2.24 for $\boldsymbol{r}^{(1)}$, the following solutions are found:

$$\boldsymbol{r}^{(1)} = \int\int \boldsymbol{A}_1 dtdt = \frac{e}{m\omega^2}\left[\boldsymbol{E}_+ + \boldsymbol{E}_-\right] \tag{2.26}$$

$$\frac{d\boldsymbol{r}^{(1)}}{dt} = -i\frac{e}{m\omega}\left[\boldsymbol{E}_+ - \boldsymbol{E}_-\right] \tag{2.27}$$

Now the result can be substituted into eq. 2.25:

$$\frac{d^2\boldsymbol{r}^{(2)}}{dt^2} = \left[-i\frac{e}{m\omega}\left(\boldsymbol{E}_+ - \boldsymbol{E}_-\right)\right] \times \left[-\frac{e}{mc_m}\frac{\boldsymbol{k}\times\left(\boldsymbol{E}_+ + \boldsymbol{E}_-\right)}{k}\right] \tag{2.28}$$

Expanding the vector product in eq. 2.28 and using the dispersion relation $\omega = c_m \cdot k$, the equation separates into a constant and an oscillating term. The oscillating term shows a frequency of 2ω.

$$\frac{d^2\boldsymbol{r}^{(2)}}{dt^2} = \frac{e^2}{m^2\omega^2}\left[i\left(\left(\tilde{\boldsymbol{E}}_+ \times \boldsymbol{k} \times \tilde{\boldsymbol{E}}_+\right)e^{i(2\boldsymbol{kr}-2\omega t)} + \left(\tilde{\boldsymbol{E}}_+ \times \boldsymbol{k} \times \tilde{\boldsymbol{E}}_-\right)\right) + c.c.\right] \tag{2.29}$$

By integrating twice the solution for the second order term is obtained:

$$\frac{d\boldsymbol{r}^{(2)}}{dt} = \frac{e^2}{2m^2\omega^3}\left[\left(\tilde{\boldsymbol{E}}_+ \times \boldsymbol{k} \times \tilde{\boldsymbol{E}}_+\right)e^{i(2\boldsymbol{kr}-2\omega t)} + c.c.\right] + \frac{e^2}{m^2\omega^2}\left[i\tilde{\boldsymbol{E}}_+ \times \boldsymbol{k} \times \tilde{\boldsymbol{E}}_- + c.c.\right]t \tag{2.30}$$

$$\boldsymbol{r}^{(2)} = -\frac{e^2}{4m^2\omega^4}\left[i\left(\tilde{\boldsymbol{E}}_+ \times \boldsymbol{k} \times \tilde{\boldsymbol{E}}_+\right)e^{i(2\boldsymbol{kr}-2\omega t)} + c.c.\right] + \frac{e^2}{2m^2\omega^2}\left[i\tilde{\boldsymbol{E}}_+ \times \boldsymbol{k} \times \tilde{\boldsymbol{E}}_- + c.c.\right]t^2 \tag{2.31}$$

The charge oscillating with 2ω is the source for radiation with a frequency of 2ω [30]. Contrary to a linearly induced dipole, the oscillation here takes place along the direction of propagation of the EM-wave ($\boldsymbol{k}$).

A charge density as a source for SHG

Knowing now the effect of the fields onto a single electron, the effect on many electrons can best be described in terms of local charge and current densities. Similar to the expansion of the position coordinate $\boldsymbol{r}$ in the previous section, the charge density may be written as:

$$\rho = \rho^{(0)} + \lambda\rho^{(1)} + \lambda^2\rho^{(2)} + ... \tag{2.32}$$

$$\boldsymbol{J} = \boldsymbol{J}^{(0)} + \lambda\boldsymbol{J}^{(1)} + \lambda^2\boldsymbol{J}^{(2)} + ... \tag{2.33}$$

The higher order current can be written as the product of the density and the velocity.

$$\boldsymbol{J} = \left(\rho^{(0)} + \lambda\rho^{(1)} + \lambda^2\rho^{(2)} + ...\right)\left(\frac{d\boldsymbol{r}^{(0)}}{dt} + \lambda\frac{d\boldsymbol{r}^{(1)}}{dt} + \lambda^2\frac{d\boldsymbol{r}^{(2)}}{dt} + ...\right) \tag{2.34}$$

The order zero describes again the static case, for which the current density is obviously equal to 0:

$$\boldsymbol{J}^{(0)} = \rho^{(0)}\frac{d\boldsymbol{r}^{(0)}}{dt} \overset{(2.23)}{=} 0 \tag{2.35}$$

By comparing coefficients the orders one and two of $\boldsymbol{J}$ are given by:

$$\boldsymbol{J}^{(1)} = \rho^{(1)}\frac{d\boldsymbol{r}^{(0)}}{dt} + \rho^{(0)}\frac{d\boldsymbol{r}^{(1)}}{dt} \overset{(2.23)}{=} \rho^{(0)}\frac{d\boldsymbol{r}^{(1)}}{dt} \tag{2.36}$$

$$\boldsymbol{J}^{(2)} = \rho^{(2)}\frac{d\boldsymbol{r}^{(0)}}{dt} + \rho^{(1)}\frac{d\boldsymbol{r}^{(1)}}{dt} + \rho^{(0)}\frac{d\boldsymbol{r}^{(2)}}{dt} \overset{(2.23)}{=} \rho^{(1)}\frac{d\boldsymbol{r}^{(1)}}{dt} + \rho^{(0)}\frac{d\boldsymbol{r}^{(2)}}{dt} \tag{2.37}$$

For a single electron spatial density variations may be neglected, but need to be taken into account here. Since both variables affect each other, changes have to be made to eq. 2.17 - the fundamental equations for the derivation are now the magnetohydrodynamic equations (see also [30, ch. 7.7]):

$$\frac{d^2\boldsymbol{r}}{dt^2} = \frac{\partial d\boldsymbol{r}}{\partial t dt} + \left(\frac{d\boldsymbol{r}}{dt}\cdot\nabla\right)\frac{d\boldsymbol{r}}{dt} = -\frac{\nabla p}{m\rho} - \frac{e}{m}\left(\boldsymbol{E} + \frac{d\boldsymbol{r}}{dt}\times\boldsymbol{B}\right) \tag{2.38}$$

$$\frac{\partial \rho}{\partial t} + \nabla\left(\rho\frac{d\boldsymbol{r}}{dt}\right) = 0 \tag{2.39}$$

Here p is the pressure. For simplicity, we assume an isotropic plasma distribution that allows us to use the assumption $\nabla p \approx 0$. Now the velocity of the electrons may have an explicit spatial dependence.

Following a similar perturbative approach as in the previous section, yields to equations for the charge density (from eq. 2.39):

$$\frac{\partial \rho^{(0)}}{\partial t} = -\nabla\left(\rho^{(0)}\frac{d\boldsymbol{r}^{(0)}}{dt}\right) \overset{(2.23)}{=} 0 \quad \Rightarrow \quad \rho^{(0)} = \text{const. in time} \tag{2.40}$$

$$\frac{\partial \rho^{(1)}}{\partial t} = -\nabla\left(\rho^{(1)}\frac{d\boldsymbol{r}^{(0)}}{dt}\right) - \nabla\left(\rho^{(0)}\frac{d\boldsymbol{r}^{(1)}}{dt}\right) \overset{(2.23)}{=} -\nabla\left(\rho^{(0)}\frac{d\boldsymbol{r}^{(1)}}{dt}\right) \tag{2.41}$$

$$\rho^{(1)} = -\int \nabla\left(\rho^{(0)}\frac{d\boldsymbol{r}^{(1)}}{dt}\right)dt = -\nabla\left(\rho^{(0)}\int\frac{d\boldsymbol{r}^{(1)}}{dt}dt\right) = -\nabla\left(\rho^{(0)}\boldsymbol{r}^{(1)}\right) \tag{2.42}$$

and the equations for the velocity (from eq. 2.38).

$$\frac{\partial d\boldsymbol{r}^{(1)}}{\partial t dt} + \left(\frac{d\boldsymbol{r}^{(1)}}{dt}\cdot\nabla\right)\frac{d\boldsymbol{r}^{(0)}}{dt} + \left(\frac{d\boldsymbol{r}^{(0)}}{dt}\cdot\nabla\right)\frac{d\boldsymbol{r}^{(1)}}{dt} = -\frac{e}{m}\left(\boldsymbol{E} + \frac{d\boldsymbol{r}^{(0)}}{dt}\times\boldsymbol{B}\right) \tag{2.43}$$

$$\frac{\partial d\boldsymbol{r}^{(2)}}{\partial t dt} + \left(\frac{d\boldsymbol{r}^{(2)}}{dt}\cdot\nabla\right)\frac{d\boldsymbol{r}^{(0)}}{dt} + \left(\frac{d\boldsymbol{r}^{(0)}}{dt}\cdot\nabla\right)\frac{d\boldsymbol{r}^{(2)}}{dt} + \left(\frac{d\boldsymbol{r}^{(1)}}{dt}\cdot\nabla\right)\frac{d\boldsymbol{r}^{(1)}}{dt} = -\frac{e}{m}\frac{d\boldsymbol{r}^{(1)}}{dt}\times\boldsymbol{B} \tag{2.44}$$

Since $\boldsymbol{r}^{(0)}$ is static, the velocity in first order can be obtained by direct integration. The equation for velocity in second order simplifies significantly:

$$\frac{\partial}{\partial t}\frac{d\boldsymbol{r}^{(1)}}{dt} = -\frac{e}{m}\boldsymbol{E} \quad \Rightarrow \quad \frac{d\boldsymbol{r}^{(1)}}{dt} = -\frac{e}{m}\int\boldsymbol{E}dt = -\frac{e}{m\omega}\left(i\boldsymbol{E}_+ + c.c.\right) \tag{2.45}$$

$$\Rightarrow \quad \boldsymbol{r}^{(1)} = -\frac{e}{m\omega}\int (i\boldsymbol{E}_+ + c.c.)\, dt = \frac{e}{m\omega^2}\boldsymbol{E} \tag{2.46}$$

$$\frac{\partial}{\partial t}\frac{d\boldsymbol{r}^{(2)}}{dt} = -\left(\frac{d\boldsymbol{r}^{(1)}}{dt}\cdot\nabla\right)\frac{d\boldsymbol{r}^{(1)}}{dt} - \frac{e}{m}\frac{d\boldsymbol{r}^{(1)}}{dt}\times\boldsymbol{B} \tag{2.47}$$

Further the result for the first order velocity can be substituted:

$$\frac{\partial}{\partial t}\frac{d\boldsymbol{r}^{(2)}}{dt} = -\frac{e^2}{m^2\omega^2}\left[(i\boldsymbol{E}_+ + c.c.)\cdot\nabla\right](i\boldsymbol{E}_+ c.c.) - \frac{e^2}{m^2\omega}(i\boldsymbol{E}_+ + c.c.)\times\boldsymbol{B} \tag{2.48}$$

By separating the fields into their time and spatial dependencies from equation 2.48, using the equations 2.19 and 2.18 for a plane incident EM-wave, the time integral over eq. 2.48 can be solved and a solution for the second order velocity can be found:

$$\begin{aligned}\tfrac{d\boldsymbol{r}^{(2)}}{dt} = \tfrac{e^2}{m^2\omega^2}\Big\{\Big[\tfrac{i}{2\omega}(\boldsymbol{E}_+\nabla)\boldsymbol{E}_+ - (\boldsymbol{E}_+\nabla)\boldsymbol{E}_-\cdot t + c.c.\Big] \\ +i\Big[\big(\tfrac{i}{2\omega}\boldsymbol{E}_+\times(\boldsymbol{k}\times\boldsymbol{E}_+) - c.c.\big) + (\boldsymbol{E}_+\times(\boldsymbol{k}\times\boldsymbol{E}_-)\cdot t - c.c.)\Big]\Big\}\end{aligned} \tag{2.49}$$

Using the shown results for the terms of ρ and $d\boldsymbol{r}/dt$, the first order induced current can be written as

$$\boldsymbol{J}^{(1)} = -\frac{e\rho^{(0)}}{m\omega}(i\boldsymbol{E}_+ + c.c.) \tag{2.50}$$

which is oscillating at a frequency ω. The second order term includes both non-oscillating terms and terms oscillating at 2ω. Hence the second-order current density can be written as $\boldsymbol{J}^{(2)} = \boldsymbol{J}_0^{(2)} + \boldsymbol{J}_{2\omega}^{(2)}$. For second harmonic generation, only the $\boldsymbol{J}_{2\omega}^{(2)}$-term is of interest:

$$\boldsymbol{J}_{2\omega}^{(2)} = \frac{e^2}{m^2\omega^3}\left\{\nabla\left(\rho^{(0)}\boldsymbol{E}\right)(i\boldsymbol{E}_+ + c.c.) + \frac{\rho^{(0)}}{2}\left[i\left((\boldsymbol{E}_+\nabla)\boldsymbol{E}_+ - c.c.\right) - (\boldsymbol{E}_+\times(\boldsymbol{k}\times\boldsymbol{E}_+) + c.c.)\right]\right\} \tag{2.51}$$

For a plane wave the term $(\boldsymbol{E}_+\nabla)\,\boldsymbol{E}_+$ equals zero, since $\boldsymbol{k} \perp \boldsymbol{E}$:

$$\boldsymbol{J}_{2\omega}^{(2)} = \frac{e^2}{m^2\omega^3}\left\{\nabla\left(\rho^{(0)}\boldsymbol{E}\right)(i\boldsymbol{E}_+ + c.c.) - \frac{\rho^{(0)}}{2}\left[\boldsymbol{E}_+ \times (\boldsymbol{k}\times\boldsymbol{E}_+) + c.c.\right]\right\} \tag{2.52}$$

The three-dimensional wave equation, that considers the current density as a source term instead of the polarization (like in eq. 2.1), is given by (according to [40]):

$$\nabla\times\nabla\times\boldsymbol{E} - \frac{1}{c^2}\frac{\partial^2\boldsymbol{E}}{\partial t^2} = \frac{4\pi}{c^2}\frac{\partial\boldsymbol{J}(\boldsymbol{E})}{\partial t} \tag{2.53}$$

From this equation, it becomes clear how $\boldsymbol{J}$ acts as a source term for an oscillating $\boldsymbol{E}$-field. Consequently, an oscillation of $\boldsymbol{J}$ with 2ω results in an $\boldsymbol{E}$-field-component oscillating also with 2ω. A second harmonic field is generated.

In further derivations the electric field is just represented by the $\boldsymbol{E}_+$-term ($\boldsymbol{E} = \boldsymbol{E}_+$). Eq. 2.52 transforms to:

$$\boldsymbol{J}_{2\omega}^{(2)} = \frac{e^2}{m^2\omega^3}\left\{i\left[\left(\nabla\rho^{(0)}\right)\boldsymbol{E}\right]\boldsymbol{E} - \frac{\rho^{(0)}}{2}\boldsymbol{E}\times(\boldsymbol{k}\times\boldsymbol{E})\right\} \tag{2.54}$$

$$\boldsymbol{J}_{2\omega}^{(2)} = \frac{e^2}{m^2\omega^3}\left|\hat{\boldsymbol{E}}\right|^2 e^{i(2\boldsymbol{k}\boldsymbol{r}-2\omega t)}\left\{i\left[\left(\nabla\rho^{(0)}\right)\hat{\boldsymbol{e}}\right]\hat{\boldsymbol{e}} + \frac{\rho^{(0)}}{2}\boldsymbol{k}\right\} \tag{2.55}$$

Here $\hat{\boldsymbol{e}}$ is the normalized polarization vector giving the direction of the amplitude $\hat{\boldsymbol{E}}$. The current density has two components. The first term in eq. 2.55 is oscillating along the polarization direction $\hat{\boldsymbol{e}}$ and the second term is oscillating in propagation direction $\boldsymbol{k}$ of the incident electric field $\boldsymbol{E}$. Depending on the geometry of the experiment, either of the two terms in the current density can be dominating.

Phasematching

This section follows [40].

In order to calculate the response of the whole target, it is helpful to take a closer look at the charge density $\rho^{(0)}$. Since second harmonic generation occurs in a crystal, periodicity can be exploited to write the charge density in terms of a Fourier series

$$\rho^{(0)} = \sum_m \rho_m e^{i\boldsymbol{g}_m \cdot \boldsymbol{r}} \tag{2.56}$$

where $\boldsymbol{g}_m$ is a reciprocal lattice vector and ρ_m is the corresponding Fourier coefficient. The expression can be substituted into eq. 2.55:

$$\boldsymbol{J}^{(2)}_{2\omega} = \frac{e^2}{m^2\omega^3} \left|\hat{\boldsymbol{E}}\right|^2 \sum_m \rho_m \left[\frac{1}{2}\boldsymbol{k} - (\boldsymbol{g}_m \hat{\boldsymbol{e}})\,\hat{\boldsymbol{e}}\right] e^{i[(2\boldsymbol{k}+\boldsymbol{g}_m)\boldsymbol{r}-2\omega t]} \tag{2.57}$$

The concept of phase matching is to make each localized source of radiation (current density) radiate in phase, such that the emitted radiation interferes constructively. This can be achieved by keeping the phase between the source (i.e. the second order current) and the generated radiation constant, which leads to a phase-matching condition of vectors $\boldsymbol{g} = \boldsymbol{g}_m$:

$$(2\boldsymbol{k} + \boldsymbol{g}) \approx \boldsymbol{k}_{2,g}. \tag{2.58}$$

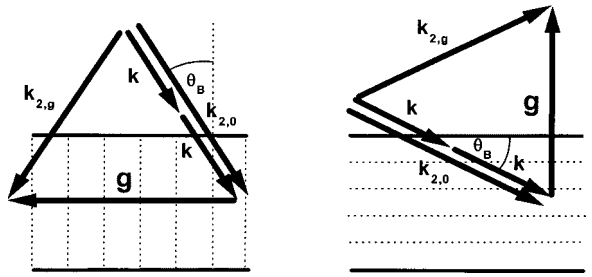

Figure 2.1: Illustration of phase-matching with incident and generated fields in Laue (left) and Bragg (right) geometry (figure from [40], modified)

Where $\boldsymbol{k}$ is the wave vector of the incident beam, $\boldsymbol{k}_{2,g}$ describes the wave vector of the generated field. This momentum conservation condition is slightly different than

the Bragg condition for 2ω since the refractive indices for both frequencies ω & 2ω are nearly equal. It is shown in fig. 2.1 for Bragg and Laue geometry.

Coupling of Fields & Walk-off effects

Since the phase matching condition implies that second harmonic generation takes place at angles close to the Bragg condition, the generated second harmonic field may be re-(Bragg)-scattered. A second generated 2ω-field emerges along $k_{2,0}$. It propagates nearly parallel to the incident beam since the generated field propagating along $\boldsymbol{k}_{2,g}$ is scattered on the reciprocal vector $-\boldsymbol{g}$, as illustrated in fig 2.1 .

At first, when the fields are generated, they overlap in space and time with the incident field. At this point, those are to be considered as coupled fields. Due to the finite focus size and pulse duration and the non-parallel propagation directions, the overlap changes spatially and in time. This effect is known as a spatial and temporal walk-off. These walk-off effects have a significant influence on the efficiency of second harmonic generation, as they reshape the spatial and temporal profile of the generated pulses.

The theory described above assumes plane wave. Since in the experiment, we used X-ray pulses of finite duration, transverse size and bandwidth, we have to extend the theory to describe the field envelopes. The equations for describing the envelopes are shown in [51, eq. 1 & 2]. Further details on the process of solving those equations can also be found in [51].

Implications of the solutions

The implications of the coupling and walk-off together with the derived current density are presented in [51]. Here, a short overview of the influences of some parameters

is given. Of particular interest is the efficiency of the process, which can be found in the experimental data, as it will be presented later in this thesis. In this case, the efficiency is defined as the relation of generated second harmonic to incident fundamental photons.

With a simulation, it can be shown that the efficiency of the process increases with the propagation length until it reaches saturation. The efficiency of the process further depends on the photon energy, where the boundary conditions from [51] lead to a peak value around 7.3 keV. The shorter the pulse duration for constant pulse energies, the higher the efficiency. The same applies to the beam size in the sample. A reduction of walk-off effects leads to higher efficiencies. The smaller the angle between the incident fundamental and the generated second harmonic beam, the more the walk-off effects are reduced.

2.2 X-ray Free Electron Laser

X-ray free-electron lasers (XFELs) are novel light sources that enable many new experiments that require a extremely intense, coherent and short pulsed X-ray light. More specifically, these high intensities are particularly important for second harmonic generation and other non-linearities. XFELs exceed the brightness of undulator radiation by several orders of magnitude. [5]

Intense X-ray light is often generated using relativistic electrons. Those are usually accelerated in bunches using electron accelerator facilities. As the bunch propagates through a transverse magnetic field, the Lorentz force directs the electrons in a curved trajectory. Due to the curved path, radiation is emitted. A source consisting of only of one magnet is called a bending magnet. Further improvement to that is provided by an undulator. An undulator consists of many alternating magnets, forcing the

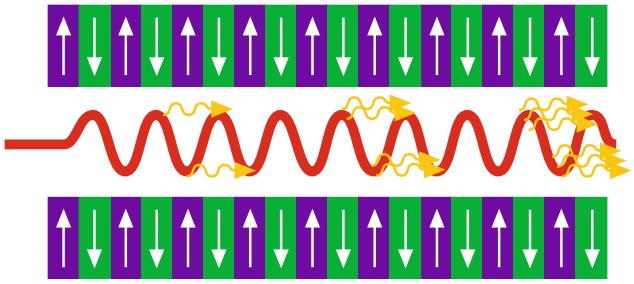

Figure 2.2: Illustration of the working principle of an undulator within a FEL; for illustrative purposes the sinusoidal trajectory of electrons is not shown orthogonal to the magnetic field (as in reality) but in the same plane (figure from [44])

electron bunch into a sinusoidal path. In an undulator, electrons radiate independent of each other; but the emitted light is in phase with the radiation from preceding oscillations. This results in intense and narrow-band but incoherent radiation. Further improvement is provided by electrons radiating coherent with each other, as realized with an XFEL. An XFEL uses a linear accelerator (LINAC) instead of a circular accelerator (synchrotron) to bring the electrons to relativistic speeds. This is necessary as, in order to achieve coherence between the electrons, the bunch must be sufficiently short in time. For instance, a 100 ps pulse that can be generated with a synchrotron is too long. After acceleration, an XFEL uses undulators, as illustrated in fig. 2.2, to generate high quality, coherent X-ray radiation.

In an undulator, spontaneous generated EM-fields interact with the electrons. The impact of this interaction depends on the electron's position relative to the phase of the field. Out of phase electrons are slightly accelerated towards an in-phase position. In usual undulator-sources, this effect is weak since it depends on the strength of the EM-field acting on the electron. A shorter electron bunch length contributes to stronger fields. Hence, strong fields / short electron bunches lead to a structuring of the electron bunch referred as microbunches. Microbunches occur with separation distances of complete wavelengths, allowing them to radiate coherently.

Linearly accelerated electron bunches are not only short but very dense due to a small divergence of about 1μrad. These properties enhance the effect of microbunching. The process that spontaneously emitted light leads to microbunching, which leads to the emission of coherent radiation, is called self-amplified spontaneous emission (SASE). In this process not only radiation at the fundamental photon energy is generated, but also photons of second and higher harmonic energy.

Due to the spontaneous nature of the process that initiates a pulse, pulse properties are subject to vary from pulse to pulse. Those properties are e.g. source point, photon energy, or pulse duration. [5, 44]

2.3 Structure of Diamond

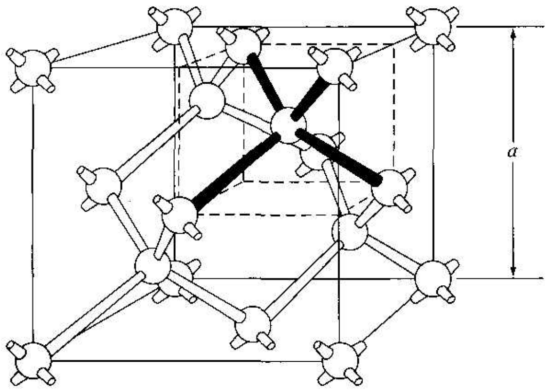

Figure 2.3: Crystal structure of diamond. Figure reproduced from ref. [41]

Diamond (C*) is a crystal with zincblende structure [16]. This structure can also be described by two equal face-centered cubic (FCC) lattices that are overlapped but shifted by one-quarter of the body diagonal to each other. This overlay transfers the cubic nature of both lattices to the diamond structure, as well as their properties as a Bravais lattice. The diamond can be described regarding the unit cell of one of the mentioned FCC lattices, as can be seen from fig. 2.3.

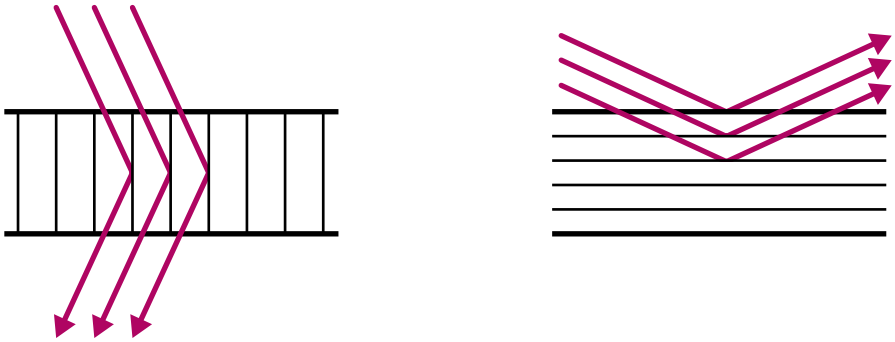

Figure 2.4: Illustration of Laue (left) and Bragg (right) geometry

For this experiment, the structure of the crystal is especially important, since it determines possible reflections and phase-matching conditions for second harmonic generation (see ch. 2.1.5). In first order approximation, the charge densities, which are sources of radiation due to interaction with incident X-ray radiation, can be viewed as localized around the nuclei. This perspective leads to the Laue equations and the Bragg condition, which as it can be shown are equal. X-ray scattering setups making use of these conditions are divided into two geometries. Those that use reflection (an incident beam penetrating the sample from the same side the output beam emerges from) are referred to as Bragg geometries and those that use transmission (an incident beam penetrating the sample from one side, while the output beam emerges from the other) are referred to as Laue geometries. Both cases are illustrated in fig. 2.4.

The Bragg condition for an n-th order reflection is according to ref. [31] given by

$$2d \sin \vartheta = n\lambda \tag{2.59}$$

where d refers to the spacing of the considered planes, ϑ is the angle for incident / reflected light relative to the plane and λ stands for the incident light wavelength.

The structure of a crystal can be expressed in real space as well as in reciprocal space. Real space shows the spatial structure of the crystal directly while the lattice

points in the reciprocal space, given by Miller indices [36], represent all possible reflections. Therefore in addition to real planes, virtual planes (nh, nk, nl) that represent nth order reflections may be introduced [35].

The distance d between two adjacent planes described by the Miller indices (hkl) for cubic lattice structures can be calculated with the lattice constant a see fig. 2.3):

$$d = \frac{a}{\sqrt{h^2 + k^2 + l^2}} \tag{2.60}$$

In diamond the lattice constant a is given with 3.57 Å.

Here we need to consider a more detailed model that includes the structure factor F in order to accurately describe the X-ray diffraction from diamond. Reflections will be allowed only if this factor is non-zero. For an allowed reflection (hkl) in diamond one of the two following conditions has to be fulfilled.

$$(h + k + l) \bmod 2 = 1 \tag{2.61}$$

$$(h + k + l) \bmod 4 = 0 \tag{2.62}$$

These selection rules allow to examine second harmonic signal by highly suppressing the reflection of the FEL fundametal using a (for the fundamental) forbidden reflection. Such a case is, for example, the (220)-reflection for 2ω-signal. The Bragg angle for this reflection equals the angle for the (110)-reflection of the fundamental (ω). Obviously, the (110)-reflection is not fulfilling either of the conditions given in eq. 2.61 and 2.62. Hence, the (220)-reflection provides suitable conditions to measure second harmonic generation. [35, 5]

Chapter 3

Experiment

3.1 Setup

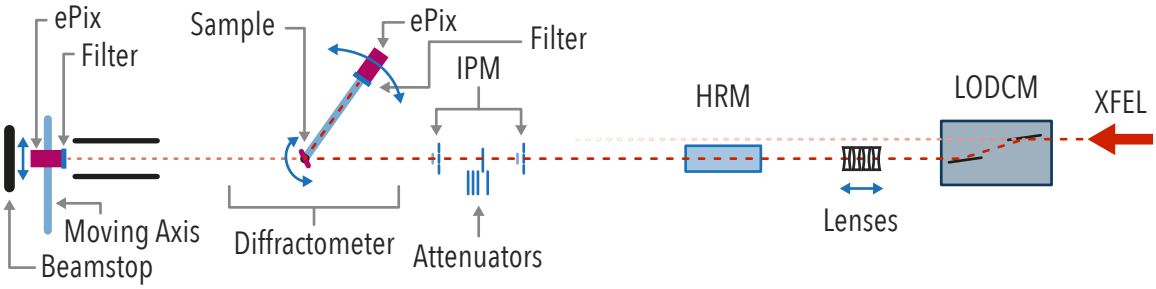

Figure 3.1: Beamline Setup Schematics: the beam is guided into the beamline with a large-offset double-crystal monochromator (LODCM). After the focusing optics, the beam passes harmonic rejection mirrors (HRM). Intensity position monitors (IPM) before the attenuators, called IPM2, and after the attenuators, called IPM3, measure the pulse energy. Different attenuating filters can be introduced into the beam. The sample and one 2D ePix X-ray detector with a filter in front are mounted onto the diffractometer. A second ePix detector is placed at the end of the beamline on a linear motorized stage just in front of the beam-stop.

3.1.1 Overview

X-ray second harmonic generation (XSHG) requires powerful and high intense X-ray pulses. Such a source can be provided by X-ray free electron lasers (XFELs). In this experiment, the XSHG is generated in a diamond sample. The signal is recorded on a 2D pixelated X-ray detector that delivers information about the photon's energy

and its position by using the single photon counting technique together with the low electronic noise of the detector of 360 eV [9]. Single photon counting statistics are ensured by placing a filter in front of the detector that suppresses the fundamental signal significantly, while it attenuates the second harmonic signal only slightly.

Because of the narrow phase-matching condition (see section 2.1.5), the XSHG signal can be maximized while avoiding damage of the sample by reducing the FEL bandwidth using a monochromator, as illustrated in fig. 3.1. Further signal-to-background-ratio is improved by using grazing incidence mirrors that reduce higher FEL harmonic contamination of the incident light, which can pass the monochromator, significantly. Moreover, the effect depends on the pulse energy which can be adjusted by inserting silicon filters of various thickness into the unfocused beam. Focussing the beam is achieved with Beryllium lenses. Two intensity position monitors (IPMs) in the beam give a scale for the energy of each pulse. The IPM that the beam passes first is called IPM2 and the other IPM is called IPM3. The sample is mounted on a diffractometer. One of the pixel detectors is mounted on an arm of this diffractometer. The detector can be replaced by a simple diode to perform calibrations. Another pixel detector is placed at the very end of the beamline, facing the incident beam. Both detectors are shielded with filters for protection and to keep a low number of photons per shot ensuring right conditions for single photon counting.[19]

The experiment was carried out at the XPP-beamline of the Linac Coherent Light Source (LCLS) at SLAC (Menlo Park, CA, USA) in September and October 2016.

The Linac Coherent Light Source (LCLS)

Based on the SASE principle LCLS can deliver pulse energies in the millijoule range and pulse duration in the tens of femtosecond regime. It can generated a photon

energy of more than 10 keV. Pulses are generated at a frequency of 120 Hz. Different operation modes allow, among others, for self-seeded pulses [6] or two-color pulses [34].

To conduct a various range of experiments, LCLS has seven beam-lines in two different experimental halls - the near experimental hall (NEH) and the far experimental hall (FEH).

This experiment was conducted in the NEH at the XPP beam-line. This beam-line allows for X-rays in the range of 4 keV to 24 keV. A diffractometer in an ambient environment setup can be provided. [13]

In the following subsections, some crucial elements of the setup are described in more detail.

3.1.2 Beamline Components

Large-offset double-crystal monochromator (LODCM)

The first element of the XPP beamline is the so-called large-offset double-crystal monochromator (LODCM). It consists of two sets of two crystals, each to allow a precise energy selection by Bragg reflection. This way, the bandwidth of the incoming FEL beam is decreased from the initial 0.4% to 0.005% (0.5 eV) using the diamond (C*) (111) reflection. So not only the bandwidth of a single pulse is decreased, but also the jittering in photon energy due to SASE with the drawback of increased intensity fluctuations. The narrow bandwidth leads to an average transmission of 1 - 2 % of the pulse energy assuming a tuned beam close to the desired wavelength. Moreover, the LODCM enables the parallel usage of the beam by a second beamline. The first crystal of each set is very thin, so it transmits the beam energies, that were not Bragg-reflected, to this other beamline. [52]

Harmonic Rejection

Since the LODCM works based on Bragg reflection, it allows for all harmonics in the beam with regard to the selected energy to pass through it. The experiment is designed to generate a second harmonic signal, which requires a minimized second harmonic background. Due to its reflectively cut-off at 25 keV, the third FEL harmonic of a 9.8 keV fundamental beam is already highly suppressed at the hard X-ray offset mirror system (HOMS) that guides the beam into the XPP beam-line [38]. Harmonic rejection mirrors (HRM) on the beamline consist of silicon mirrors that have a high reflectivity for the fundamental but not for the second harmonic. This property leads to a suppression of the second harmonic after both mirrors by a factor of 10^{-4} to 10^{-5}.

Beryllium lenses

The beamline provides stacks of beryllium lenses, fabricated by B. Lengele group in RWTH Aachen, to focus the beam. Those are located 3852 mm upstream from the sample. To adjust the focal position the lenses can be moved $\pm$150 mm up- / downstream. Different focal properties are provided by various sets of lenses that are available. For this experiment, these produce a focus with the size of 2.5 μm (σ) and a Rayleigh length of ca. 30 mm. Python libraries on-line allow for focus size calculation. [4]

Si-Attenuators

The pulse energy of the FEL fundamental can be reduced by using Silicon attenuators. Different thicknesses of filters can be inserted remotely. They can be used to

investigate the intensity-dependence of the process. Using these attenuators, it is also possible to identify background-signal in the beam.

Diffractometer

The orientation of the sample, which is mounted onto a holder, is controlled by a diffractometer. The diffractometer also provides a mount for a detector. Meaning it can act as a theta-two-theta-apparatus, but both angles can be controlled separately. This way the crystal planes on which the beam will be incident may be selected. But also rocking curves can be recorded. The angles can be configured using known Bragg peaks of the sample.

3.1.3 Detectors

Intensity Position Monitors (IPMs)

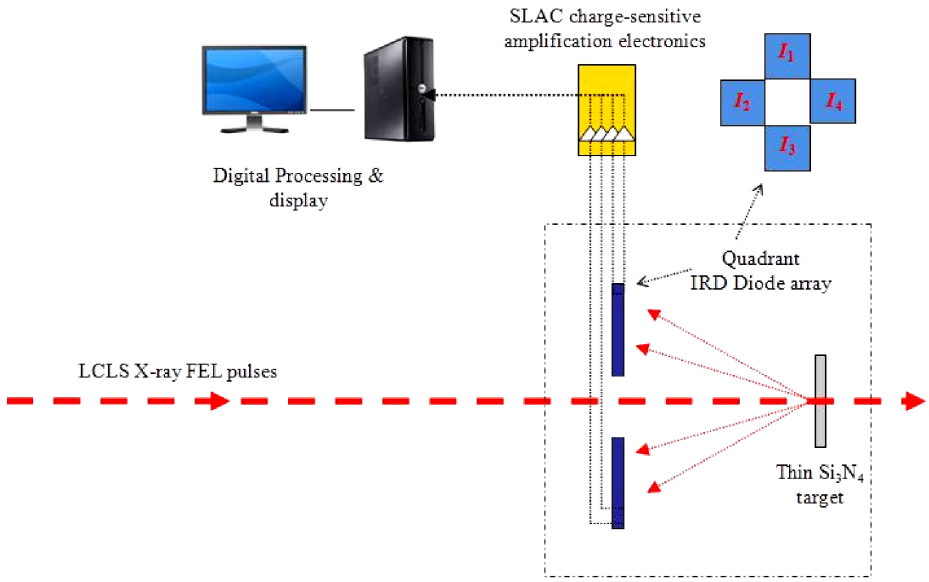

Figure 3.2: Intensity position monitor (IPM) schematics: an IPM consists of a target and four diodes collecting the backscattering signal. The diodes and their readout electronics resolve single shots. [22]

The intensity position monitors (IPMs) are an essential tool for the analysis of the data. They give a signal that relates to the shot-by-shot pulse energy of the beam. The IPMs consist of a thin target intersecting the beam and four diodes detecting back-scattered X-rays. The target has a high transmission depending on the beam energy. It is selected out of four targets that are currently installed. It has a low surface roughness as well as highly uniform density to preserve the coherence property of the FEL. The four diodes allow for calculation of the total intensity of each pulse as well as the position of the beam, on that cross-section - the so-called pointing. It provides a relative precision of 0.11% for intensity measurements and an absolute precision of 5 μm and below (2.5 μm limit for sufficiently high intensities) for horizontal and vertical beam positions. The limiting factor for the precision of the detectors is given by the Poisson-statistics of the collected X-rays per single shot. The suppression of the vertical jitter of the FEL beam by the HOMS makes the right and left diodes of the IPMs a more precise tool to relate the IPM signal to the intensity than the vertical ones. [22]

PIPS

Instead of using a pixel-array detector, like the ePix, also a simpler 1D diode detector is available. This diode is a passivated implanted planar silicon (PIPS) detector.[1] It provides a more straightforward approach for recording rocking curves and other data, e.g., for finding Bragg-peaks and calibrating diffractometer angles with those.

ePix Detectors

The detectors used to measure the second harmonic signal are the ePix100 detectors provided by LCLS. Those second generation integrating hybrid pixel detectors provide an active area of ca. 35×38 mm and a resolution of 704×768 pixel (ca. 0.5 megapixel).

Figure 3.3: Photo of an ePix100 detector [17]

With their small pixels of 50×50 μm they allow for single photon counting for a high photon flux compared to larger pixels or single diode measurements. Even for a very low photon flux, due to the pixel's low noise behavior and high quantum efficiency, the detector stays efficient. Experiments show that, e.g., over 60 peaks due to multiple 7keV photons hitting one pixel of the detector each integration time (shot) can be distinguished. [17] The detector response towards incident signal is linear. [9]

The second harmonic generation experiment uses two ePix100 detectors. As can be seen from fig. 3.1, one is placed on an arm that is mounted onto the diffractometer, and another one is placed in the so-called alcove, which is the end of a pipe in which the beam propagates after the sample before it hits a beam stop. The ePix detector in the alcove is used for focus finding and calibration as well as for looking for a processes that emit into the forward direction.

Filter for ePix Detectors During the experiment different filters in front of the ePix detectors were used to suppress undesired (e.g., fundamental) signals by multiple orders of magnitude more than the desired signal (e.g., second harmonic). For most of the measurements, a 1.5 mm Al-filter has been used. It transmits 25.9% of the second harmonic signal ($9831\text{eV} * 2 = 19662\text{eV}$), while only 0.00264% of the fundamental signal passes through the filter [29].

3.1.4 The Sample: A diamond crystal

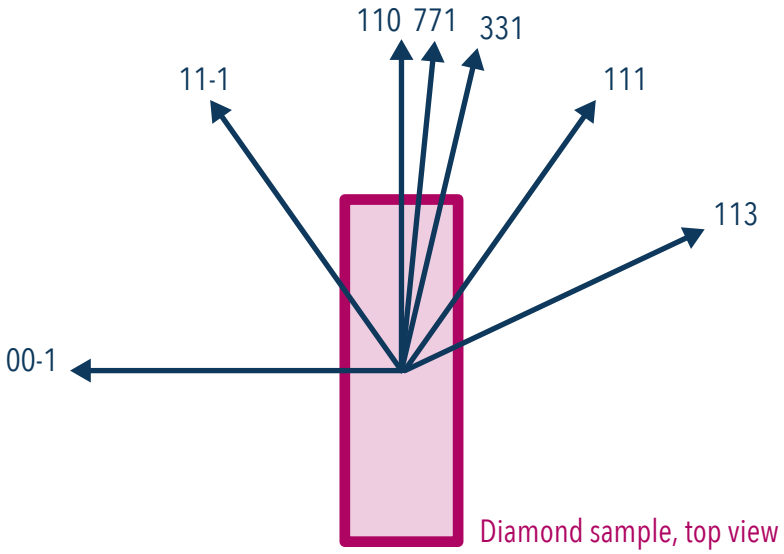

Figure 3.4: Accessible planes in the diamond sample, when rotating around $1\bar{1}0$ plane. The vectors indicate the reciprocal vectors, which are perpendicular to the lattice planes.

A diamond crystal with the dimensions of $4 \times 4 \times 0.8$ mm is used as a sample for second harmonic generation. The faces of the diamond are cut to match the crystal planes (110),(001) and $(1\bar{1}0)$ so that the crystal forms a cuboid. The face with a size of 4×4 mm has the (001)-face. For the whole experiment, the sample is mounted on the diffractometer so that it rotates around the $(1\bar{1}0)$-surface normal.

As shown in fig. 3.4 this makes the planes (mmn), where m and n are integers, that exist for diamond and allow for Bragg reflection, accessible. More planes would be accessible when changing the axis of rotation for the crystal in the diffractometer. Using the Bragg condition (eq. 2.59) and the orientation of the planes towards the (110) face, which are taken as reference in the experiment, expected angles for looking at the Bragg reflection can be found. The reflections used in the experiment are shown in table 3.1 .

Plane	**Incident Beam**		**Outgoing Beam**
	grazing angle to plane	*grazing angle to sample (220 plane)*	*scattering angle (output to incident beam)*
$(00\bar{4})$	20.70	−69.27	41.47
$(11\bar{1})$	8.81	−26.44	17.64
(220)	14.48	14.48	29.00
(660)	48.59	48.59	97.37
(771)	61.58	67.48	123.46
(331)	22.66	35.94	45.39
(111)	8.81	44.07	17.64
(113)	17.05	81.82	34.14

Table 3.1: List of reflections used in the experiment with angles for geometry; all angles are given in degree.

3.2 Procedure

3.2.1 ePix Calibration

At the start and during the experiment calibration images for the pixel detector are taken. Two types of images are necessary: a dark shot, meaning images without incident X-ray light (beam has to be off) and a flat exposure image, where the detector is illuminated with a flat intensity beam profile. The second kind of images is usually generated using fluorescence light, e.g., of copper under FEL radiation. Knowing those two points and assuming linearity of the detector, the correction of pixel-specific offsets and gain differences is possible. Furthermore, the common-mode noise will be corrected in post-processing with algorithms explained in ref. [3]. [10]

3.2.2 Focal Alignment

Due to the limited availability of time for experiments at XFELs, standard procedures, like finding the focus, require fast and precise techniques. Ideally, those require no more than one-dimensional scans and simple setups. By using speckle patterns to enable focal alignment those conditions can be met.

Speckle patterns occur when coherent light is either reflected on rough surfaces or when it is transmitted due to scattering through some material. Diffuse reflection or transmission introduces phase shifts which depend on the path taken by the light. Furthermore, the diffuse nature of those processes leads to interference effects in the beam itself. When inserting a plane for imaging, those interference effects form a speckle pattern. [27]

In the far field, the size of the speckle pattern corresponds in first-order approximation to the inverse of the illumination volume. Hence a larger speckle size is generated from a smaller illumination volume and hence the closer to the focus the sample is placed. A detailed analysis also allows for an advanced focus characterization. [47]

For focal alignment, a scan along the beam propagation axis with nano-sized particles for diffuse transmission is made. The speckle pattern is then analyzed automatically, and an average speckle size is found. Plotting the average speckle size over the z position of the sample indicates at its maximum the optimal focal position. Within the Rayleigh range close to the focus, the illumination volume changes are only small which indicates that a position close to the focus has been found. Now a more sensitive method, such as scanning intensity-dependent processes for the best efficiency or doing a knife-edge scan, can be used. A knife edge scan is also suitable for focus characterization and will be described in the next section. For this experiment, all three methods were applied.

3.2.3 Focus Characterization

There are different established methods for focus characterization at XFELs. For this experiment, a knife-edge scan [7] is used. It is a fast and simple technique that allows for beam cross-section characterization with a sub-micrometer resolution [47]. Assuming the focus has been found, e.g., as described before (see ch. 3.2.2) the focus can be characterized. It can also be used to find the focus, but exhibits several disadvantages, like time consumption as compared to the method presented before.

For such a scan some beam attenuating material with a sharp edge, like that of a knife, is required. This piece of material is then placed out of the beam and is moved slowly into the beam (or vice versa) on a fixed axis while the signal is recorded. The signal is integrated (temporal and spatial) for each position of the knife edge. The integration values are plotted over the positions of the knife edge. A curve described by $\int_{-\infty}^{\infty}\int_{x}^{\infty} B(x',y)dx'dy$ with regard to a beam profile $B(x',y)$, can be fitted to that data points. A beam profile can be reconstructed from the parameters that were fitted for the intensity-beamprofile by assuming, e.g. a Gaussian beam profile. It is important to note that with this method only a projection of the beam profile onto the x' axis (axis perpendicular to knife edge) can be reconstructed. For distorted or asymmetric profiles, the same procedure has to be repeated at different orientations of edge and appropriate moving direction relative to the beam [8]. For an accurate measurement, the beam jitter relative to the knife edge has to be minimal and stable beam profile is required. Otherwise, it often yields an overestimation of the beam size. [47]

3.2.4 Energy per pulse calibration

To determine the energy per FEL pulse after the beam reached the experimental station, XPP provides a power meter as it is used for conventional lasers in the optical regime. The measurement of the energy here is imprecise and gives only a reasonable estimate rather than an exact value, which is also valid for alternative devices. The power meter is used to assign an energy value per pulse to the IPM scale. The measured value will overestimate the actual energy per pulse by roughly a factor 2 to 3 [53]. The calibration of the IPM scale will be done with a time-averaged IPM value corresponding to a time-averaged pulse energy.

3.2.5 Diffractometer: Angle-Calibration and Sample Alignment

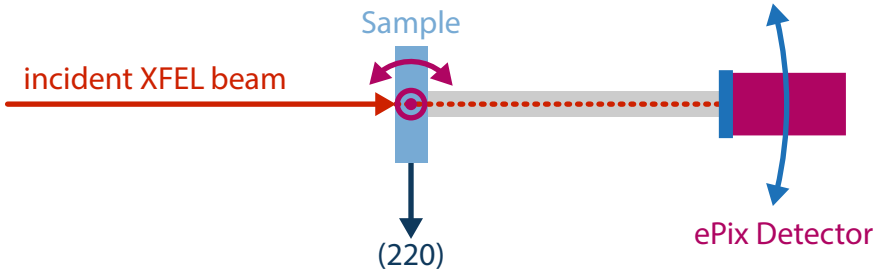

Figure 3.5: Ideal alignment for sample and detector at zero degrees

The sample is mounted onto a holder, which is mounted onto a rotation stage. At first, a rough alignment is done by eye - e.g., the desired face/plane has to be parallel to the incoming beam. At this position, the motor is set to zero degrees (see fig. 3.5). Exact angles are defined, by looking for known Bragg peaks of some accessible crystal planes, which are reflected at precise angles. This way, also during the experiment, small corrections to the calibration can be applied quickly.

The angle of the detector arm can be set by measuring the transmitted direct beam using high attenuation. At this setting, the zero angle beam can be placed on

a chosen area of the detector. So this area can be selected by avoiding very noisy pixels.

After calibration, as shown in fig. 3.5, the zero position for the sample orientation is achieved with the (220)-face parallel to the incident beam. The detector faces in its zero position the incident beam.

Chapter 4

Analysis

4.1 Preprocessing of the Data

Since the detectors are recorded for each FEL shot separately and the machine is operating at 120 Hz, the amount of data resulting from this experiment is in the order of several terabytes. To deal with this raw data, the complete analysis is done remotely on server clusters. Already in the recording process the data is organized in certain sets, called runs. Usually, each run represents an individual set of experimental settings.

The first step in the analysis is the so-called pre-processing, in which the raw file format xtc is read and after some automated analysis and conversion, the results are stored in an HDF5 file. This file type allows for fast and easy reading by using different standard programming languages or software like MATLAB. Furthermore, the file size is reduced significantly.

During the pre-processing, the data passes through multiple algorithms. In particular, the ePix detectors undergo a special treatment. At first, the 2D ePix X-ray recorded image undergoes standard corrections. These use data from the detector calibration such as a series of dark shots for pedestal correction and a gain map as well as apply appropriate algorithms for common mode correction.[2, 3]

The signal's intensity on each pixel is given in Analog-Digital-Units (ADUs). The

ADU values scale linear with the number of electron-hole-pairs registered on a pixel and thus can be correlated with the energy of the hits.

Secondly, predefined spatial masks are applied to the detector. Moreover, to automatically interpret the signal on the ePix detector, a preprocessing algorithm can be used. A provided toolset includes a so-called droplet-algorithm, which is explained in ch. 4.1.3, and photon algorithms, which are written for other pixel-detector types than ePix. Other options are to skip that step and work with the raw data directly, as shown in ch 4.1.2 , or to write a custom interpretation algorithm. The latter option has been done for this experiment and is explained in ch. 4.1.4 .

4.1.1 Spatial Masking

The goal of masking the detector is to exclude malfunctioning pixels from the data. Using detector calibration data, pixels, that show a too high or too low pedestal, can be identified. Also, pixels giving a signal on a dark shot, which overcomes the average noise level on the detector by a certain factor, have to be excluded. This is why pixels over a threshold of 10 sigma of the width of the electronic dark noise in a dark shot are masked. Such a mask is presented in fig. 4.1. It shows the mask from the online analysis for run 168. The applied limits for pedestals that are not masked are 2000 in the lower limit and 6000 in the upper limit.

With this information, the masked image is then forwarded to the next level of pre-processing.

4.1.2 Plain Data

As described already at the beginning of section 4.1, the usage of one of the predefined algorithms for further pre-processing is optional. So the most straightforward way is to continue without any algorithm and with storing the ADU values for each pixel

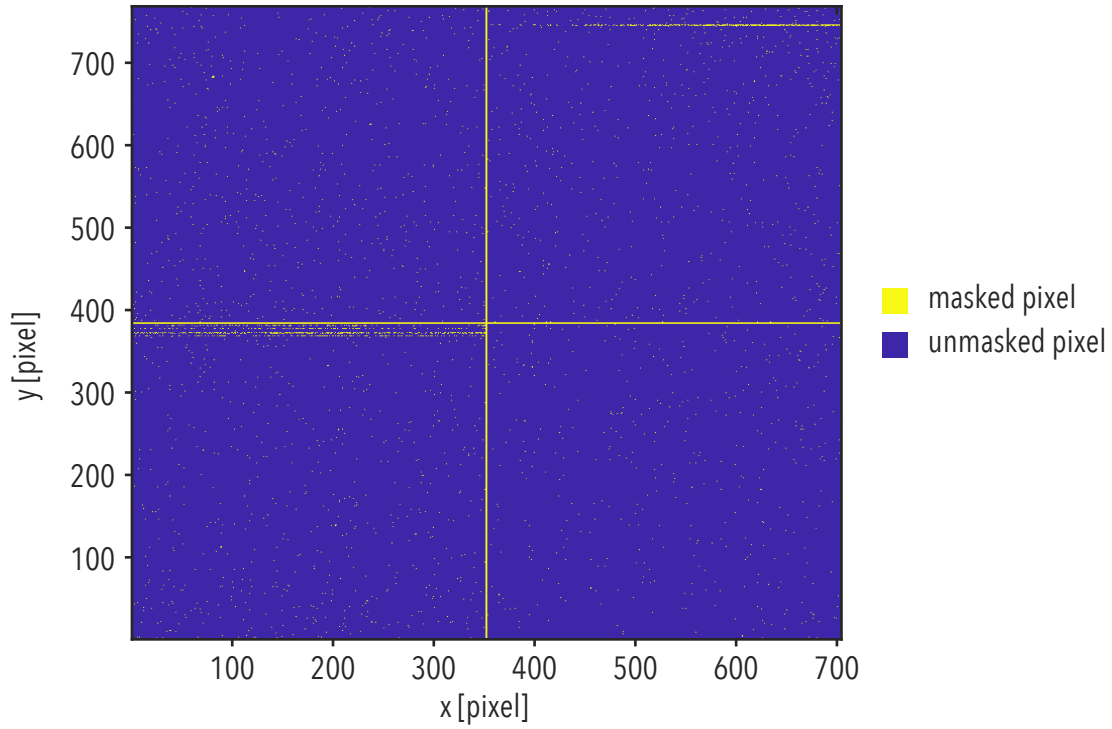

Figure 4.1: Mask for detector in run 168 (rocking curve for second harmonic generation at (220)-reflection); masking criteria: $pedestal < 2000$ ADU, $pedestal > 6000$ ADU, $rms > 10$. The horizontal and vertical lines are the limits of the four ASICs used for the readout electronics

directly into a file. This is an important step to explore advantages in further preprocessing algorithms. There may exist cases were the usage of the raw data results in smaller errors, to minimize the error in the analysis.

For understanding the raw data and how to analyze it, processes in the detector that occur due to an incident photon and lead to its measurement have to be taken into account.

A photon that hits the ePix detector yields photoexcitation resulting in primary and secondary excited electron-hole-pairs. Those are then relaxed down to the conduction band and guided towards the electrodes through the sensor (due to its thickness). As shown in fig. 4.2, the lower electrode is divided into pixels. Those relate the incident photons to their position on the detector. Mainly, due to the distance, the

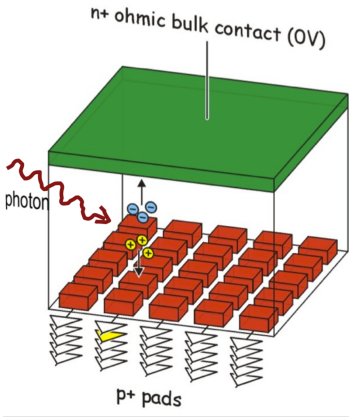

Figure 4.2: Process in the detector due to a hit by photon, also illustrates how pixel are implemented in architecture. (fig. taken from ref. [18])

holes drift to the pixel, thereby their distribution spreads perpendicular to the beam. That distribution of the pixels, resulting from one photon hit, can be approximated by a Gaussian function. It has for an ePix100 detector a standard deviation of 8.5 μm. So it is possible for some of the electron-hole-pairs to generate a signal on more than one pixel. Hence the information regarding that photon may be spread over multiple neighbored pixels. This effect will be further referred as pixel-sharing. Additionally, it may happen that two photons hit mainly the very same pixel, generating a signal that looks like one photon of twice the energy. Such effect is called pile-up. [53, 18]

Methods for analysis

Without considering any pixel-sharing or pile-up effects, in a histogram of the ADU values of each pixel over all shots, slightly broadened peaks at ADU values corresponding to multiples of the incoming photon energy, as illustrated on the left in fig. 4.3, would be expected. For different photon energies, non-overlapping intervals can be found. By Integrating over those intervals, the number of photons in each peak can be deduced.

Due to the Gaussian distribution of the excited electron-hole-pairs in the detector

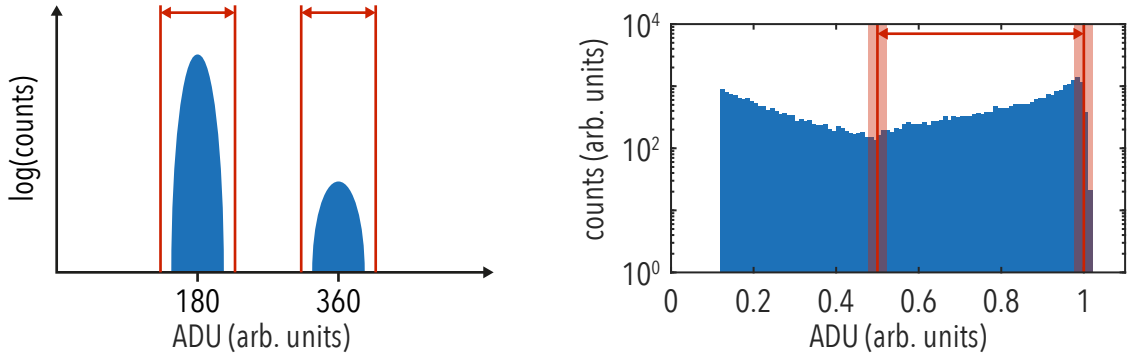

Figure 4.3: Effect of pixel-sharing onto ADU histogram; left: expected ADU histogram without pixel-sharing shows clear peaks for fundamental and second harmonic signal. right: simulated ADU histogram for 25000 second-harmonic photons considering pixel-sharing with parameters of the ePix detector.

relative to the hit, the signal can be spread over up to four pixels. As a result, the pixel that has the highest contribution can contain a fraction of the signal, down to 25%. However, many photons cause a signal on multiple pixels, so a simple integral over the range of signal does not lead to the number of photons. The expected signal is presented on the right in fig. 4.3. Simulations further show that an approximate photon count can be obtained by integrating over the upper 50% of the region that shows signal. This implies for fig. 4.3 (right) an interval from 0.5 to 1.0 ADU plus error-ranges addressing the limited energy resolution of the detector (here: 0.03 ADU).

The upper limit of each interval has to be found, to define these ranges in the raw data. Therefore a run with a clear fundamental signal and a run with a clear second harmonic signal is used. With knowledge of the upper limits for ω and 2ω signal, other upper limits can be inferred.

A data set of the run 172 shows significant fundamental signal. It contains data of a rocking curve for the Bragg reflection (111) of the fundamental. Its ADU histogram (up to 1000 ADU) can be seen in fig. 4.4, where the detector's signal clearly overcomes its noise. The upper limits for the ADU intervals are set at the ADU value after a

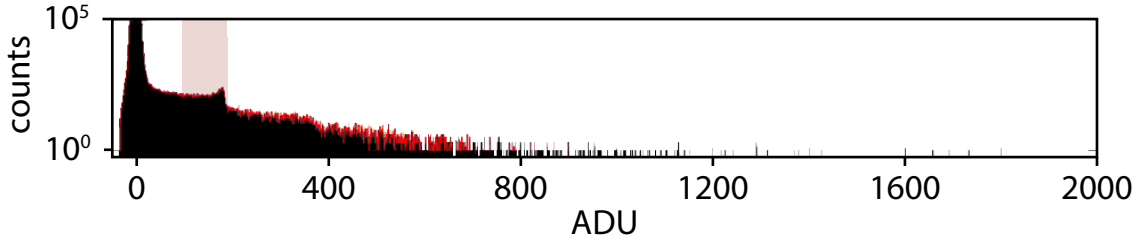

Figure 4.4: Run 172 ADU histogram for full detector from plain data; red: identified fundamental (ω) ADU region of interest (ROI)

significant decrease of the signal. Since all runs are recorded under similar conditions, for all runs the level (rms) of the detector's noise of this particular run can be assumed. It is found to be ca. 2.7 ADUs. Hence the errors for each interval limit are set to ± 8.1 ADU.

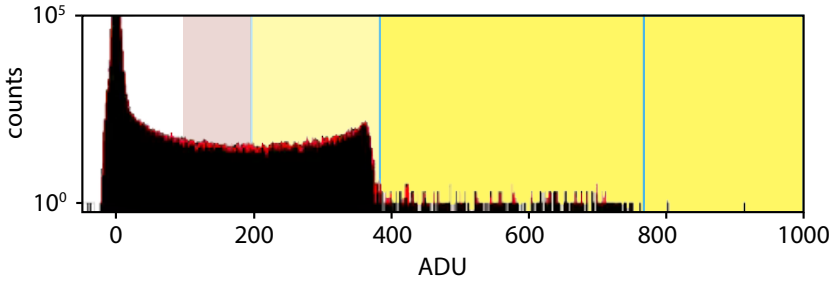

Figure 4.5: Run 169 ADU histogram for small region on the detector that contains interesting signal (spatial region of interest) from plain data; higher order region of interest (ROI) was inferred from other ROIs

The ROI for SHG signal is obtained with data from run 169, shown in fig. 4.5, which shows pure SH signal. Higher order ROIs are inferred. To study the performance of this analysis method with the defined intervals, a nearly ideal signal was used. Since such a signal was recorded in run 169, it is of further use. Its ADU histogram is presented in fig. 4.5 and shows data from second harmonic generation at a fixed angle, with nearly no fundamental background and very few pile-up counts (counts with an ADU above second harmonic range). The low fundamental background can be seen from comparing the data with the simulation shown in in fig. 4.3

(right). It shows a same qualitative shape.

The second harmonic signal can be counted by integrating over the appropriate ADU range found before. It shows 8500 ± 600 hits, so an error of 7%. However, 9000 ± 3000 pixels are counted in the fundamental range. Using the assumption that no fundamental signal hit the detector, this signal is explained by shared-pixels that contain only a small fraction of the generated charge. By computing hits within the first pile-up range (4ω), 230 ± 30 hits are counted.

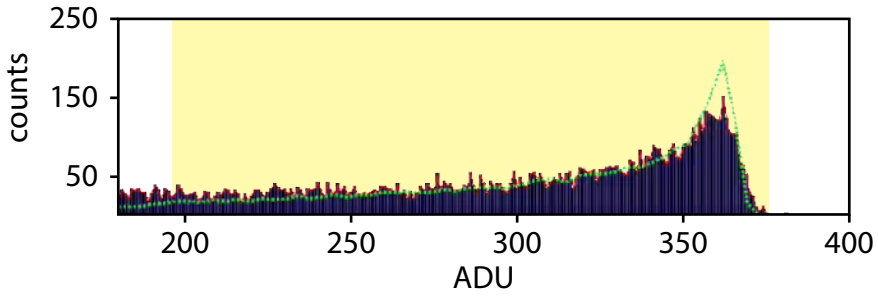

Figure 4.6: Simulation of an ADU histogram for a 5×5 pixel array for 25000 single photon hits, considering also the detector noise, overlayed and scaled manually to fit the ADU histogram in run 168 approximately. Results in predicting 8800 ± 400 photons

Using the results from the simulation, that have been used for qualitative comparison only until now and with the knowledge of the original number of photons simulated, the photon count in the signal can be reconstructed. To this end the fraction of photons is converted into ADU values. The simulation result can be fitted to the experimental signal (see fig. 4.6). Results of this fitting show simulated counts within the error-range of the counting of the raw data: 8800 ± 400 photons. The similarity of this results with the integrated experimental signal supports the method of counting hits contained only in the upper half of the covered ADU range. Moreover, the simulation shows that this method gives a number of photons slightly below the actual one. Further, it is to be noted that the simulation considers a uniform dis-

tribution of photon hits over the whole pixel. Inferring from the hit distribution on the detector this assumption is unlikely. Still, it seems to be a good approximation. Small differences between the data and the fit, as in fig. 4.6, may be explained by this approximation.

Limits

For data with low fundamental background and pile-up signal, only for the first pile-up range - not for pile-up in higher orders - the presented method gives promising results. However, higher pile-up orders will become a problem. As mentioned above, the intervals above half the peak ADU range gives reliable results. Thus, for higher pile-up orders the range of half the harmonic peak ADU value to the harmonic peak ADU value have to be taken into account. However, after the two-photon peak, only an upper fraction of the ADU range can be used for the integral, because the other signal overlaps with lower order ranges.

In general, also the signal below the 50% mark overlaps with lower signal ranges. So only for a signal at significantly higher ADU values, the additional miscounts can be neglected, and the signal in the range can be estimated. Due to this effect already for run 169, it is not possible to determine the number of fundamental hits, which is essential for a full estimate of the pile-up statistics for this energy. The method can be tested for a dominating fundamental signal depending on the number of higher harmonics to be counted.

Effect of limitations on real data

Scenarios described in the last section are now to be demonstrated by applying the presented method and together with simulation results onto two more runs. To show a scenario with significant pile-up the run 172, will be analyzed. Furthermore run 191

that shows low pile-up but fundamental as well as the second harmonic signal will be used.

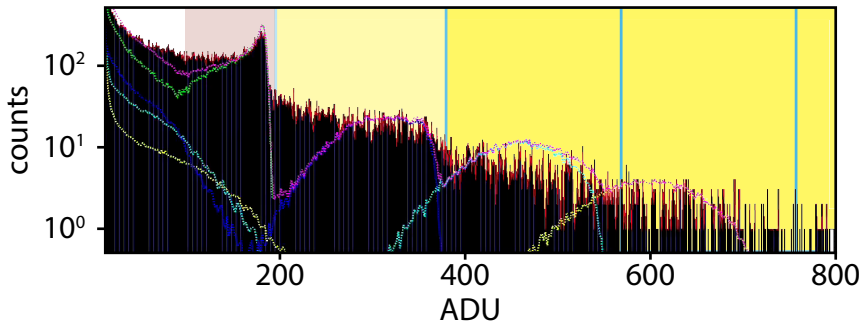

Figure 4.7: Run 172 ADU histogram for position ROI on detector from plain data; red: fundamental ROI; yellow; pile-up ROIs; histogram overlapped by fitted simulation data; magenta: cumulative curve, green: fundamental signal only, blue: first pile-up only, cyan: second pile-up only, yellow: third pile-up only;

Run 172: The resulting ADU histogram for run 172 is presented in fig. 4.7 along with fitted simulation data. The many pile-up peaks show a softening of their edges in the simulation, explaining the nearly continuous ADU histogram of the data. This means that part of the pile-up signal starts to overlap with the fundamental ROI. When integrating the fundamental bin, a significant fraction is due to the pile-up signal. While the data shows, 13000 ± 2000 counts, the fitted simulation (green) gives only 9000 ± 1000 photons. The cumulative curve (magenta) on the other hand gives 10000 ± 1000 counts by integration. The discrepancy between simulation and data can only be explained by more detailed simulations, which are beyond the scope of this thesis. Thus it has to be considered as an additional error of ca. 30% that has to be taken into account, meaning finally for the data $13000\,(+2000, -6000)$ counts. Similarly, the first pile-up shows a signal of $3600\,(+900, -2000)$ by considering an addition error of again ca. 30% (derived by same principles as presented before). Fig. 4.7 shows that higher pile-up signal lacks for good statistics which makes it not

possible to make a precise fit. 800 $(+400, -500)$ counts are identified for the second pile-up peak (including again an additional error of 30% based on what was found for the peaks before). For the same reasons, no reliable data can be obtained from higher pile-up ranges.

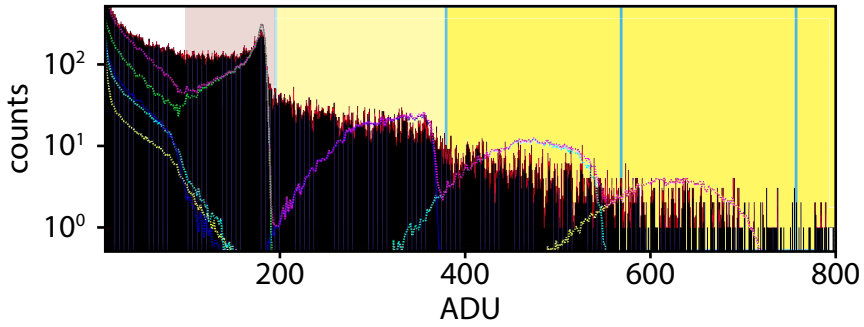

Figure 4.8: Run 172 ADU histogram for position ROI on detector from plain data, fundamental ROI red, pile-up ROIs yellow; histogram overlapped by fitted simulation data; magenta: cumulative curve, green: fundamental signal only, blue: first pile-up only, cyan: second pile-up only, yellow: third pile-up only; The fit is based on the assumption that the pixel experience a uniform illumination.

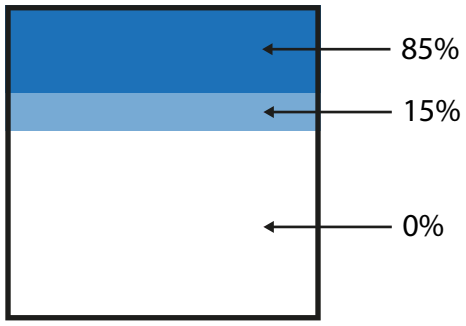

Figure 4.9: Pixel illumination profile for a single pixel optimized for run 172; the percentages give the probabilities for a photon hitting a certain region of the pixel. The upper region (dark blue) covers the upper 28% of the pixel, the middle region (light blue) covers 12% of the pixel and the not illuminated region (white) covers the lower 60% of the pixel.

At this point, an additional comment on the simulation and fit is to be made. For run 172 a new feature was necessary. Due to the unsatisfying performance of the standard algorithm, as shown in fig. 4.8, that considers uniform illuminated pixel,

a different illumination profile has been chosen. For a simple implementation a 2 step illumination profile, as shown in fig. 4.9, with a chance of 85% of a photon to be spatially detected in the upper 28% region of a pixel, a chance of 15% to hit the middle 12% of the pixel and a chance of 0% to hit the lower 60% of the pixel. These specific settings were obtained by optimizing the simulation for the ADU histogram of run 172 as, e.g., shown in fig. 4.7. By comparing the results of the standard algorithm with the results of the new illumination profile shown in fig. 4.7, a clear improvement can be seen. Following this tendency, it appears that the differences between data and simulation can indeed be described due to the illumination profile, which is in reality individual for each pixel.

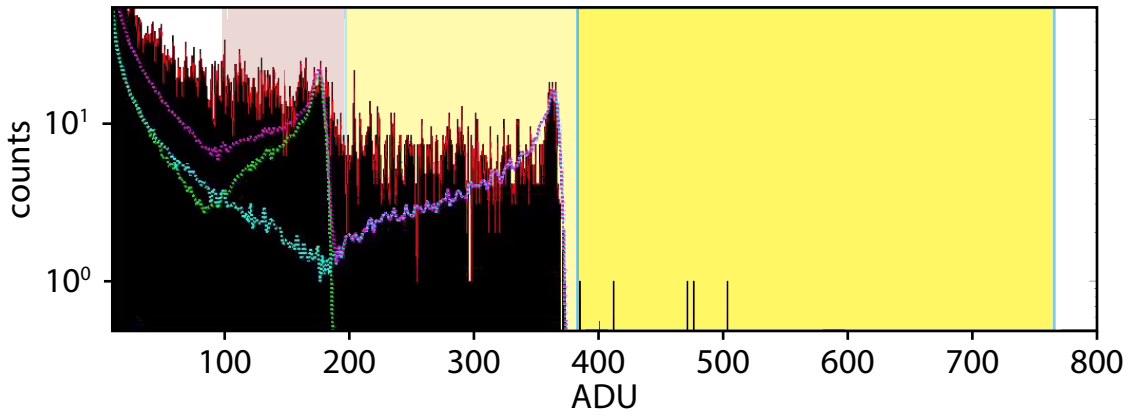

Figure 4.10: Run 191 ADU histogram for position ROI on detector from plain data, fundamental ROI red, pile-up ROI yellow; histogram overlapped by fitted simulation data; magenta: cumulative curve, green: fundamental signal only, cyan: second harmonic only;

Run 191: Hence data only from an illuminated ROI (position) on the detector is to be considered. Data in this scenario is different to run 172 as shown in the histogram in fig. 4.10. Here fundamental signal and native second harmonic signal are the major contributions. This can be, not only identified by the relation of the intensities of the ADU ROIs, but especially it can be deduced by looking at the shape of the

peaks. Unlike in run 172, both peaks exhibit clear and sharp edges. As can be seen from fig. 4.10, the fundamental signal peak is broader than the second harmonic peak. Since both are two independent (regarding hitting/within the detector) processes, the difference can be explained considering different distributions of the hits on the single pixels. Hence to fit the data, the used simulations are also based on two different distributions. It can be shown that a slimmer peak indicates that a larger area of the pixel receives the majority of the hits.

The quantitative analysis of the fundamental region works similar to the one done for run 172. This way the number of fundamental counts is given as 1600 ± 1000. The significant error arises from the overlap with the second harmonic signal, as well as from the deviation of simulated fit and experimental data. It is not distinguishable whether or to which parts arise from uncertainties in the simulation regarding the fundamental counts or the overlap with the second harmonic signal. However, for the second harmonic signal, this is not the case. There it is clear that the difference between experimental data and simulation fit arises from inaccurate assumptions made in the simulation. The simulated curve underestimates the counts by 30% compared to the real counts that are given with 1100 ± 200. Applying the new method towards the fundamental would reduce the error due to the difference between simulation and data to zero and only the overlap and range limits contribute to the error. However, as stated before, the hit distribution on the pixel for the fundamental is different and it overlaps with other signal, so therefore the method is not applicable.

Conclusion

Conclusively it can be stated that working with the plain data can give promising results. Even for inconvenient cases such as significant pile-up or overlapping of two native signals, the measured counts for data ranges with sufficient signal stay more

significant than the errors which allow at least for classifications regarding the order of magnitude. For good cases and a high quality of the signal, the errors due to the method can be reduced to below 5%, which makes this method suitable for those cases.

Though, the limited capabilities of the simulations lead to a high uncertainty in the results. The next section will show, whether processing algorithms can overcome that uncertainty.

4.1.3 Standard Droplet-Algorithm

The droplet algorithm is the standard detector interpretation step in preprocessing for ePix detectors with a low number of hits per each shot expected.

Goal of the droplet algorithm

A droplet algorithm aims to process the detector (pixel-resolved) signal to reconstruct actual information about the photon that hit the detector. It is used to preprocess the data to enable a convenient way of analyzing measurements.

The preprocessing for this experiment uses a droplet algorithm written by Silke Nelson. [42] The analysis will rely on two versions of it. The most recent version is accessible via GitHub. [2]

Applied Methods

The basic Principle of the droplet algorithm is that it is looking for "islands", so-called droplets, of signal over the noise level of the detector, e.g., as shown in fig. 4.11 (a). Therefore it applies at first a certain threshold that a peak has to overcome. Furthermore, it looks for surrounding pixels that overcome a second lower threshold. Each threshold is defined as a factor concerning the specific pixel's electronic noise

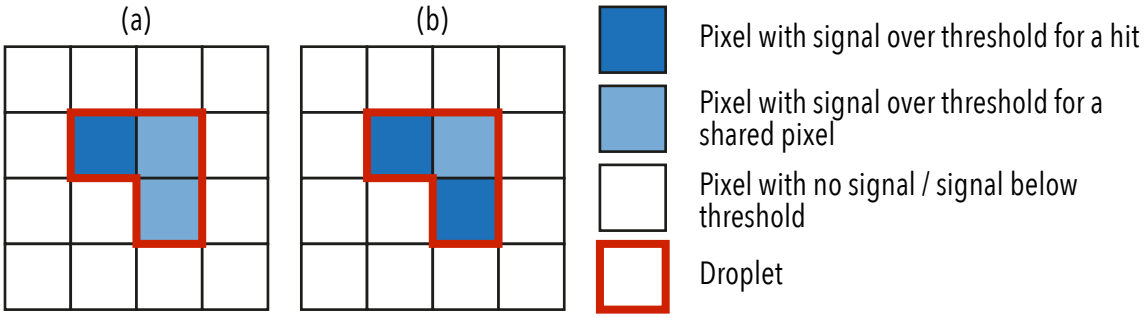

Figure 4.11: Working principle of the droplet algorithm; Left: the situation with one hit and surrounding shared pixels, the droplet algorithm works appropriately. Right: situation with two close hits and one shared pixel that is neighboring both hits, the droplet algorithm does not work properly

on the detector from the most recent dark run. As can be seen from this method: the droplet algorithm gives only meaningful information when each shot contains a low number of hits, and hits that are far from each other. Otherwise, droplets begin to merge like in fig. 4.11 (b).

The algorithm looks for more signal of the droplet in a "sourrounding" pixel. A "surrounding" pixel is a direct neighbor (right, left, top or bottom) but not a diagonal neighbored pixel. To include those diagonal neighboring pixels it needs a next neighbor that is already included in the droplet (as can be seen in fig. 4.11).

In order to reconstruct a photon hit, for an identified droplet the sum of each pixel's signal (ADU) will be assigned to that droplet. Furthermore, the position of the droplet will be given by an ADU-weighted average of each pixel's position forming the droplet. Also, the number of pixels each droplet consists of is stored.

Errors

The algorithm interprets the detector signal individually for each shot. This automation is necessary since the experiment's data consists of several million shots. For the program, it is crucial to minimize misinterpretation, but the limits regarding the

validity of the applied methods and other errors in the resulting dataset may not be suppressed entirely. The most critical errors that may occur will be discussed in this paragraph.

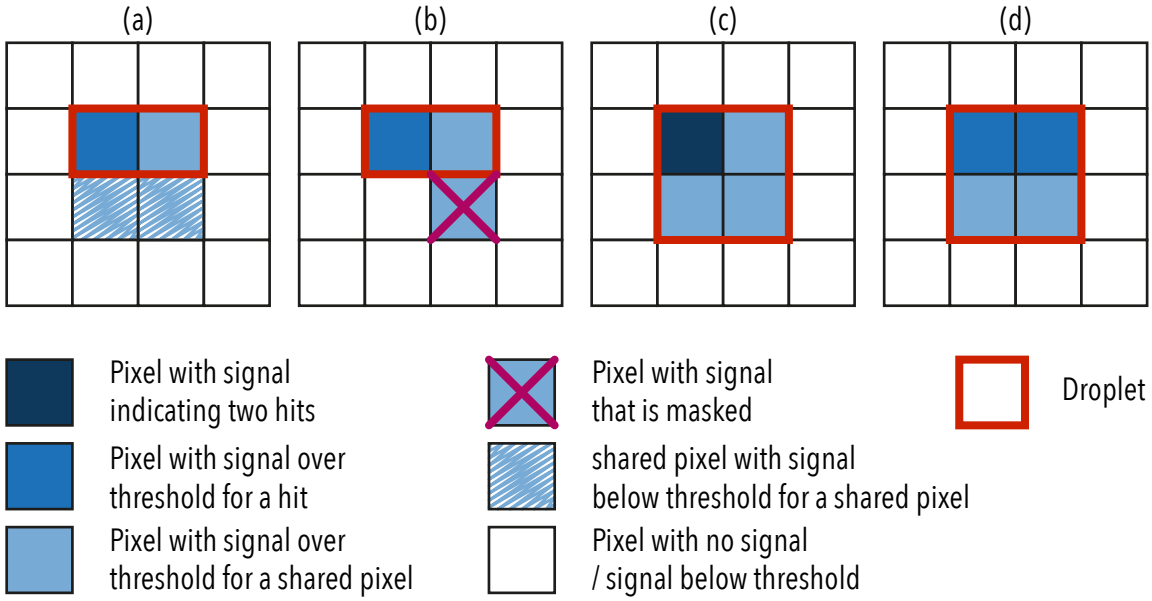

Figure 4.12: Errors that can occur using the droplet algorithm; (a) shows shared pixels that have ADU counts below the threshold and hence are not included within a droplet. (b) illustrates a pixel that should be part of a droplet, but is masked and thus does not contribute to the droplet. (c) is a situation that may happen with or without the droplet algorithm, a pixel is hit by two photons within the same shot and can not be distinguished from signal with doubled frequency. (d) presents an effect that looks at ADU values the same as the situation in (c), but instead of two photons hitting the same pixel they are just close enough to contribute to the same droplet.

The threshold applied to the algorithm for finding peak-surrounding pixels with signal implies that signal below this threshold will be lost, as illustrated in fig. 4.12 (a), although it may be hidden in the detector's noise anyways. Since the effect of pixel-sharing follows its statistical nature, the losses will vary for each droplet, but overall this will lead to a peak broadening in terms of ADU values. The error can be minimized by having a lower threshold that is just above the noise level. A threshold of $3 \cdot rms$ with regard to each pixel's (dark) signal is used. So only the detector's noise

contributes to the rms, and not the signal of each shot. Using an individual pixel threshold, the best possible signal over noise level is collected. Only ca. 0.3% of the noise may be above this level. Furthermore, each pixel that overcomes the threshold contains an ADU value which is the sum of signal and noise. This means that an error in the ADU values scales with droplet size. This leads to further broadening of the signal in the energy spectrum.

In the standard configuration of the droplet algorithm, masked pixels may be neighbors to pixels in the current droplet. With a detector image in which the masks already have been applied, as shown in fig. 4.12 (b), such possible signal will not be included as a shared pixel. Modifying options to run the droplet algorithm, this kind error can be reduced by also considering masked pixels next to pixels that are found to be part of a droplet. This may be done in offline analysis but is typically not done online, due to the larger required processing time of the algorithm. Nevertheless, the problem persists for peaks lying on masked pixels.

Furthermore, the rare event (when the algorithm is applied to an appropriate dataset) that two droplets come very close to each other, although their peaks may not overlap, they may appear to the droplet algorithm as a single droplet. The standard algorithm applied here is not able to separate those droplets nor able to mark droplets that may contain two photons. Hence in addition to the rare event of ordinary pile-up (fig. 4.12 (c)), when two photons hit the very same pixel in one shot (first kind of pile-up), the droplet algorithm contributes with a second kind of pile-up (fig. 4.12 (d)) to the preprocessed data. It may be referred to that kind as the pile-up of the second kind.

Effect of errors onto signal

The way the droplet algorithm acts on data can be illustrated using data that may promote certain errors, as described before, shown in fig. 4.12. Since pile-up will cause the major error, this is the effect that will be analyzed in this section.

At first, we will take a look at a run in which more photons are expected to hit the detector than the algorithm can deal with. Pile-up effects, as illustrated in fig. 4.12 (c) & (d), are expected to be stronger in this as compared to other data sets. Such a run is run no. 172, which recorded a rocking curve of the Bragg reflection of the (111)-plane that allows a reflection of the fundamental wavelength. This reflection occurs directed with a small divergence. This is why only a small region on the detector is illuminated. To suppress noise in the signal, in the following, only data from this region is considered. Since the cross-section for second harmonic generation is expected to be many orders of magnitude lower than for Bragg-reflection of fundamental signal [46] and the FEL second harmonic is highly suppressed, the data-set is expected to be dominated by the fundamental and probably will contain nearly no second harmonic signal.

A good way to illustrate the effect of the droplet algorithm is to use ADU histograms that show the signal for different droplet sizes (in pixels) as plotted in fig. 4.13.

As can be seen from fig. 4.13 there exists a significant number of droplets of the size of only one pixel. This implies that there exists at least one zone on the pixel where the probability for enough electrons to accumulate in neighbored pixels to overcome the threshold for a shared pixel is low. Describing the average electron distribution with a Gaussian function (centered where the pixel has been hit), the electrons exhibit some mean free diffusion length, leading to the conclusion that this

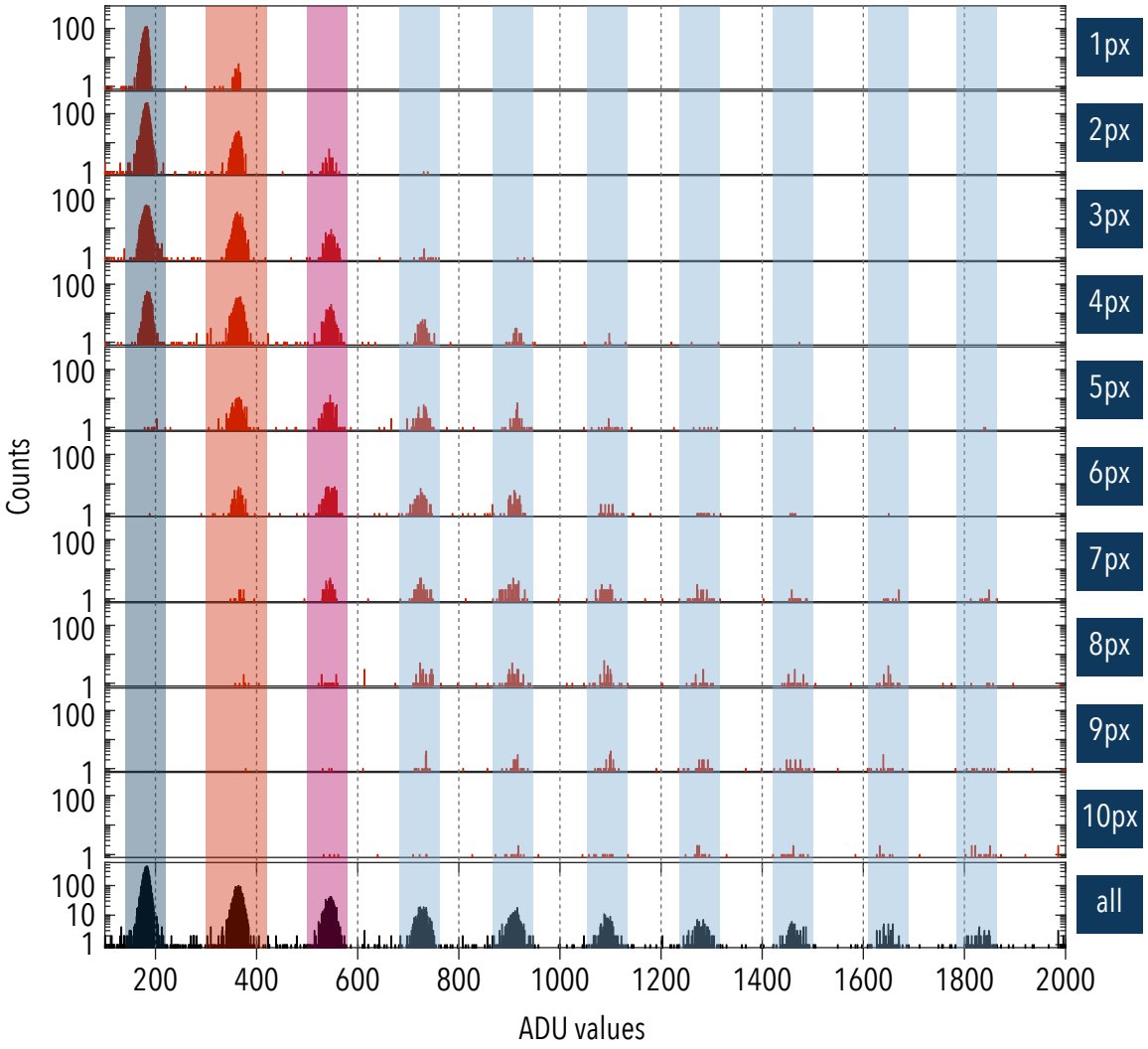

Figure 4.13: ADU histograms for run 172 by size of droplets in pixel (label on the right-hand side) and histogram in the bottom over all droplet sizes; Y-axis scales logarithmically; Marked ROIs for fundamental (dark blue), first fundamental pile-up (red), second fundamental pile-up (pink) and higher order fundamental pile-up (light blue); The signal is expected to dominated by fundamental photons.

is one central zone and that the position of shared pixels depend on the position the incident photon hits the single pixel. The data also shows that a droplet with an area of larger than four pixels is improbable for those that show no pile-up nor any second harmonic signal. For the same run, the pile-up dominated peak at energies of the second harmonic shows on the other hand that larger droplets than four pixels

contribute with a relevant number of counts towards the total number of hits. Two consecutive hits can be considered in the form of a linear combination of each single one. Hence the shift towards larger droplets may be caused by pile-up of the second kind.[53, 18]

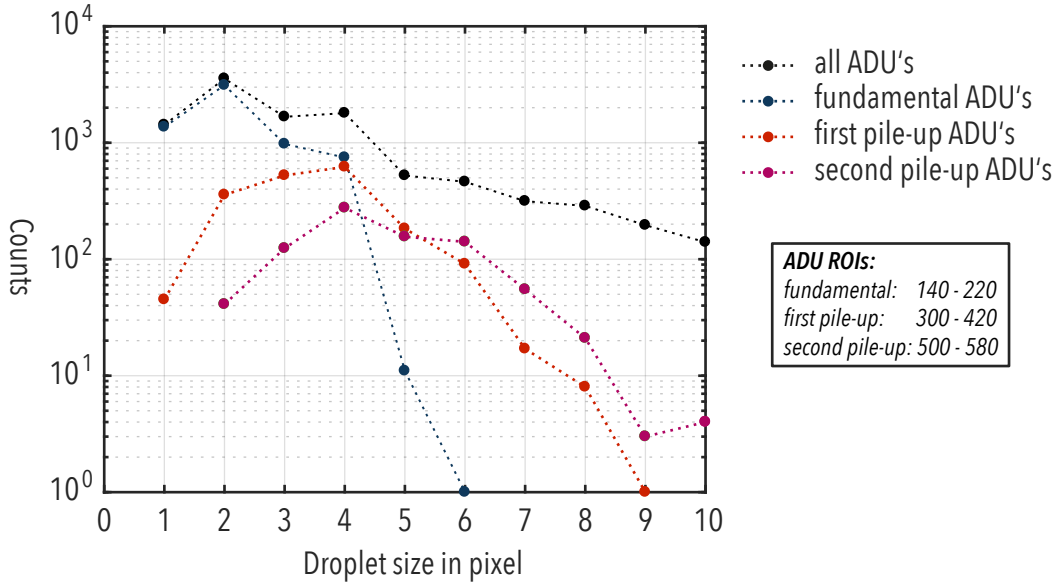

Figure 4.14: Dropletsize vs. counts by different ADU ranges (ROIs) and for all ADU's for run 172; Y-axis scales logarithmically; The color scheme follows that of fig. 4.13: fundamental (dark blue), first fundamental pile-up (red), second fundamental pile-up (pink) and all ADU's (black); The signal is expected to be dominated by fundamental photons (other photon energies are neglected).

So, in general, the tendency that higher orders of pile-up correlate with bigger droplets is observed from fig. 4.13. A better visualization of this effect is presented in fig. 4.14. Each colored data point represents the integral value of one ADU ROI (as specified in the figure) for a certain droplet size. The black data points represent the integral over the whole ADU range for each droplet size. It confirms the tendency from fig. 4.13. Not only as obviously expected differ the blue, red and pink curve in fig. 4.14 in intensity, they are also displaced relative to each other.

Simulations show that pile-up of the first kind may shift the pile-up peak slightly

but not enough to overlap with the here measured droplet sizes. When allowing hits spreading multiple pixels according to the hit distribution on the pixel of run 172, the simulation of ADU distribution per shot and the afterward applied droplet algorithm results in a droplet size distribution that agrees with minor differences close to peak well with the experiment. Those minor differences may be explained by a non-uniform distribution of the photon hits on the pixels themselves. (for details on the simulation, code and some comments see the appendix A) The simulation supports the argument that the droplet algorithm indeed produces the second kind of pile-up (fig. 4.12 (d)) and it furthermore can have a significant influence on the interpretation of the data. Significantly more pile-up than actually is occurring may be seen in the pre-processed data.

Thus data from run 172 shows that pile-up of the second kind can be identified by a shift of the probability on the occurrence of droplet sizes when comparing hits at the fundamental and its first pile-up energy on the detector. Furthermore, the pile-up of the second kind is much more probable than pile-up of the first kind, so its effects dominate the pile-up in the preprocessed data.

For a dataset that contains a real second harmonic signal, e.g., run 191 was chosen. The identification of the real second harmonic signal can be made by using the ADU histograms in fig. 4.15. Since most of the second harmonic signal is confined to a small region (over 90% of the signal) in which only a small fraction of the fundamental energy signal is contained (less than 1%), and in which the expected fundamental, four-photon pile-up signal shows nearly no signal. Further, the second harmonic two-photon pile-up energy shows slightly more signal than the fundamental second pile-up energy. A significant pollution of the second harmonic signal by fundamental two-photon pile-up can be ruled out by applying Poisson statistics. Those can be used to describe the pile-up process [20].

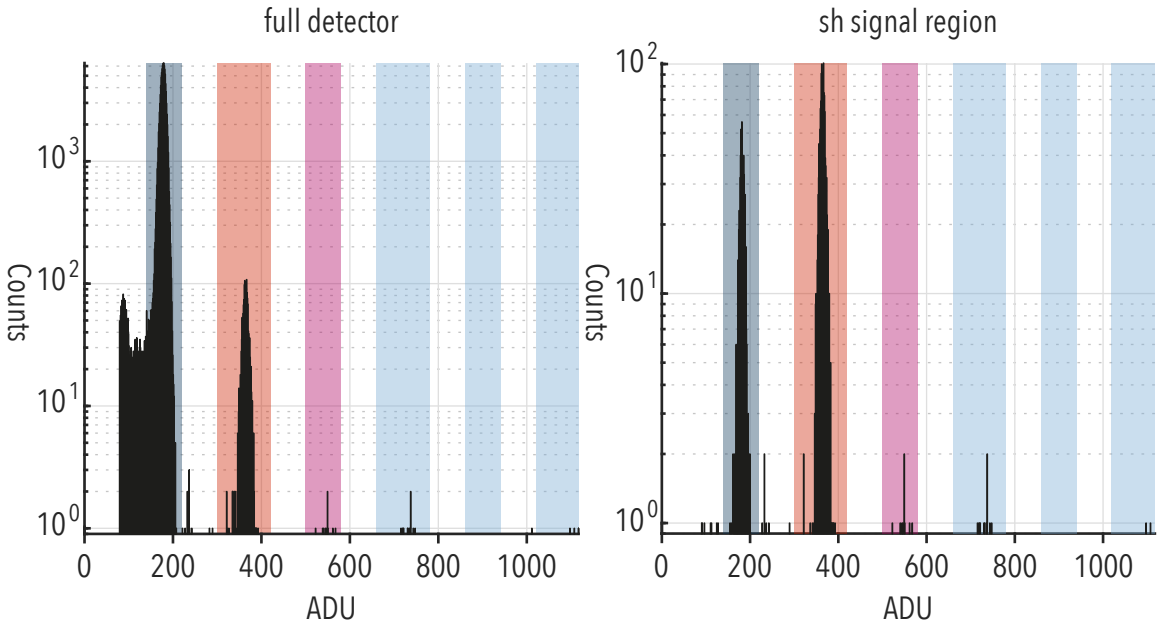

Figure 4.15: ADU histograms (ADU vs. counts) for full detector and region with confined second harmonic signal for run 191; Y-axis scales logarithmically; Follow color scheme of fig. 4.13: fundamental (dark blue), second harmonic / fundamental pile-up (red), second fundamental pile-up (pink) and higher order pile-up (light blue); The fundamental region in the left plot contains 102187 counts where the same region in the right plot contains only 630 counts, while the second harmonic region in the left plot contains 1550 counts and in the right plot 1397 counts.

Now the droplet size distribution for this run, shown in fig. 4.16, can be analyzed. Opposite to the distribution of run 172 (see fig. 4.14), the curve for the fundamental signal and the data points for two-photon fundamental pile-up / single-photon second harmonic (SH) signal are not displaced to each other. Applying the conclusion from run 172 that pile-up signal can be identified by a relative shift of both curves to each other, the same deduction as in the preceeding paragraph is obtained. The apparent SH signal shows no significant contribution of two-photon fundamental pile-up signal.

The analysis method proposed by the conclusions of the study of run 172 has been successfully tested with this data set and applies to identify signals that are dominated by pile-up rather than actual signal in the observed energy- / ADU-range.

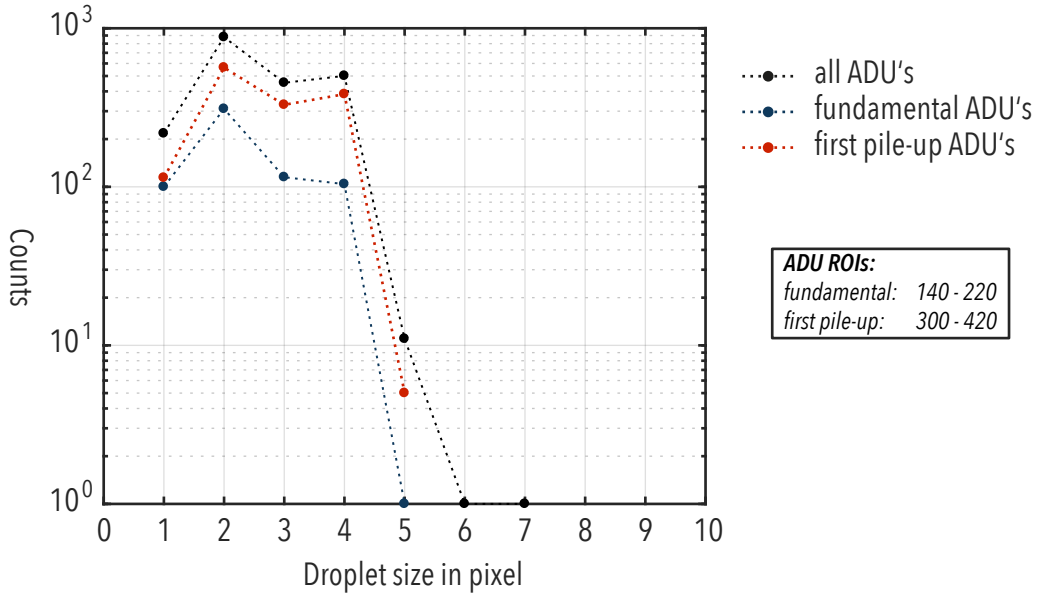

Figure 4.16: Droplet size vs. counts by different ADU ranges (ROIs) and for all ADU's for run 191; Y-axis scales logarithmically; Follow color scheme of fig. 4.14: fundamental (dark blue), second harmonic / fundamental pile-up (red) and all ADU's (black); No shift of red curve compared to blue curve identifies it as second harmonic and not pile-up signal

Furthermore, this test demonstrates that artifacts assigned with pile-up are not generated from the appropriate signal in the same energy range. It is clear that the results of the droplet algorithm may distort counting statistics and hence depending on the average count rate may increase the error significantly.

Conclusion

Overall the algorithm performs well in reconstructing the original photon signal from the distribution on the detector. This becomes more clear when comparing the results of this algorithm with the ideal signal proposed in fig. 4.3. The algorithm causes a small spread in an ADU histogram. However, it misinterprets some signal distributions which leads to additional pile-up. This pile-up can be added as an error directly, but it leads to an error caused by the analysis and not the experiment. Improvements

to this may will be achieved by using a custom written droplet algorithm.

4.1.4 Custom Droplet-Algorithm

The custom droplet algorithm aims to preprocess the detector's signal, using improved approaches, to reconstruct actual photon hits. Therefore the pile-up of the second kind is to be reduced, while the noise due to separating droplets is to be kept low.

Concept

The customized droplet algorithm follows the same basic concept as the previously analyzed droplet algorithm. As a consequence of the too large droplets, that are actually multiple neighboring or overlapping droplets, this algorithm aims for isolating single droplets. It is constructed to find impossible (non-logic) droplet shapes, meaning shapes that a single photon cannot generate.

The algorithm consist of four functions. One that all the data is accumulated with and actual droplet finding algorithms are delegated, though this function also finds

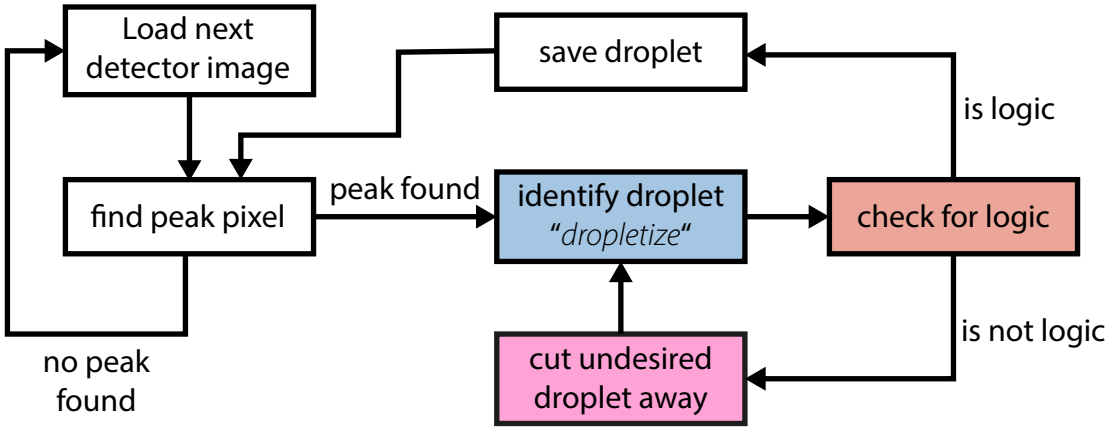

Figure 4.17: Block diagram for custom droplet algorithm; each color (white, blue, red & pink) represents a different function. The "dropletize" function is called recursively until enough droplets are cut away temporary. When a droplet is finally classified as "logic" all temporary removed droplets are added back into the detector image, while the found droplet is masked out.

the peak pixels. The other three then identify droplets, check whether it is a possible (logic) shape and in case it is not, parts that are probably not part of the droplet are dismissed. After that the function to identify droplets is called again. This process repeats recursively, as also shown in fig. 4.17.

Process of finding a droplet: The principle of the procedure is illustrated with a block diagram in fig. 4.17. After loading the detector image, at first a "peak pixel" is found, in which the algorithm searches for the pixel with maximum ADU value in the region of interest. The detected potential peak pixel then has to overcome a peak threshold - analogous to the standard droplet algorithm. This maximum pixel will be referred to as center pixel. The center pixel is then handed to the function "dropletize".

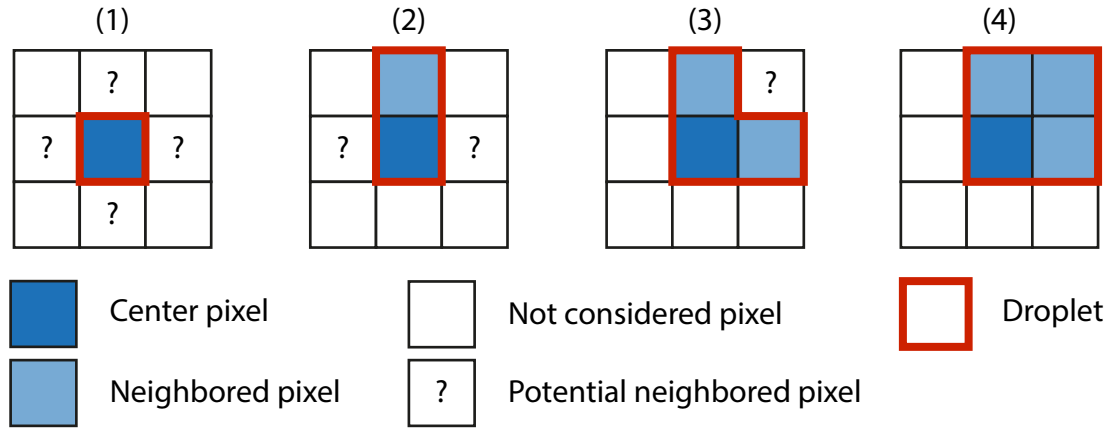

Figure 4.18: Illustration of how a droplet is found; (1) look in all neighbored pixels from the center pixel, (2) look to the right and to the left, with regard to the in (1) found neighbored pixel, (3) consider the pixel between the in (1) and (2) found pixels as a potential fourth pixel, (4) a droplet with maximal size is found

A droplet is found by searching in the surrounding pixels for those that overcome a lower threshold (same threshold concept as the standard droplet algorithm). To state it in more detail, as illustrated in fig. 4.18, at first, for the pixel that shows the most signal of all direct neighboring pixels is searched (fig. 4.18 (1)). Then, the

algorithm searches for a second maximum neighboring pixel that lies either at the right or at the left relative to the first found neighbored pixel (fig. 4.18 (2)). Further it looks for a possible fourth pixel in the droplet at the corner between neighbored pixels, which were just found (fig. 4.18 (3)). To be included, the fourth pixel's ADU value has to be smaller than 110% of each surrounding pixel, otherwise it is not included (it could be, e.g., a second peak pixel). A Droplet has been found, that has an "allowed" shape. But at this point it is not clear whether those neighbored pixels are peaks themselves or are influenced by other peaks next to them. This is why, in a next step, this possibility is checked. A droplet is flagged (marked to be part of a merged droplet), when there is another pixel overcoming the threshold for at least a neighbored pixel on the outer edge of the found droplet. Droplets that are not flagged will be returned, and the head function looks for the next peak.

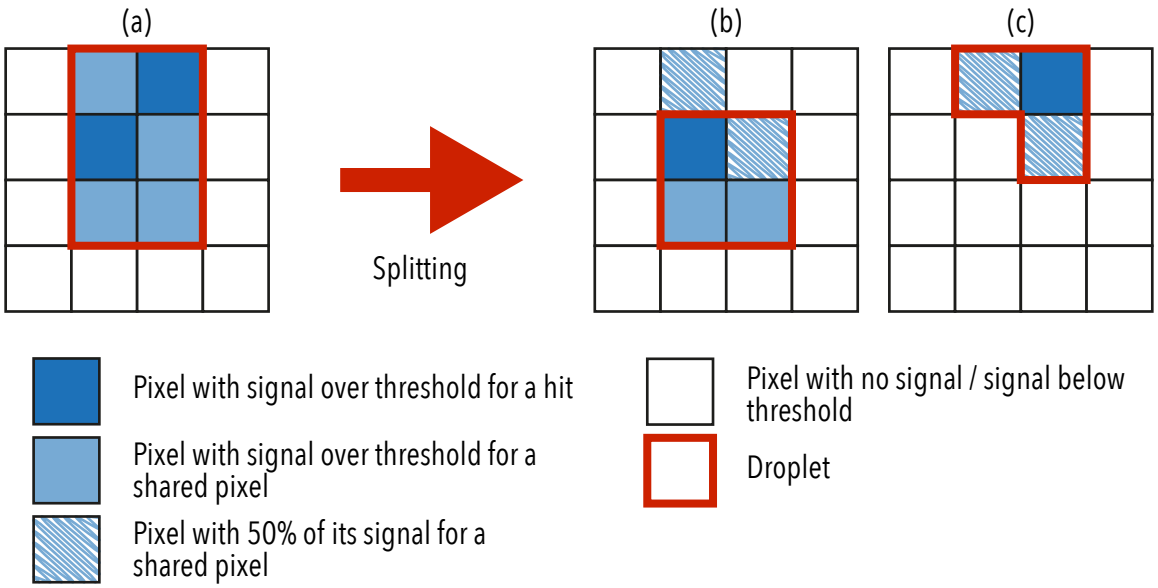

Figure 4.19: Illustration of droplet splitting: the algorithm splits the droplet in (a) by knowing two peaks, pixels (except peaks!) shared by both are split in half. Assuming the isolated droplet in (b) contains the original found peak, the other droplet shown in (c) is removed and (b) is processed as new identified droplet. Since the upper pixel in (b) does not overcome the peak threshold the red droplet is not flagged and it is saved. The previously excluded part of the droplet is added back into the data.

Flagged droplets will be processed with a "split"-function. It looks for another peak in a larger 5×5 neighborhood of the center pixel. If such a peak is found (see also the example in fig. 4.19), commonly shared pixels are cut in half in their ADU value. The extra droplet is masked out and the remaining image is fed back to the "dropletize"-function. the process repeats itself recursively until an ordinary droplet is recognized (not flagged). Afterwards the detected droplet is masked out of the image and the ADU values that have been cut away before are added back to the image.

Errors

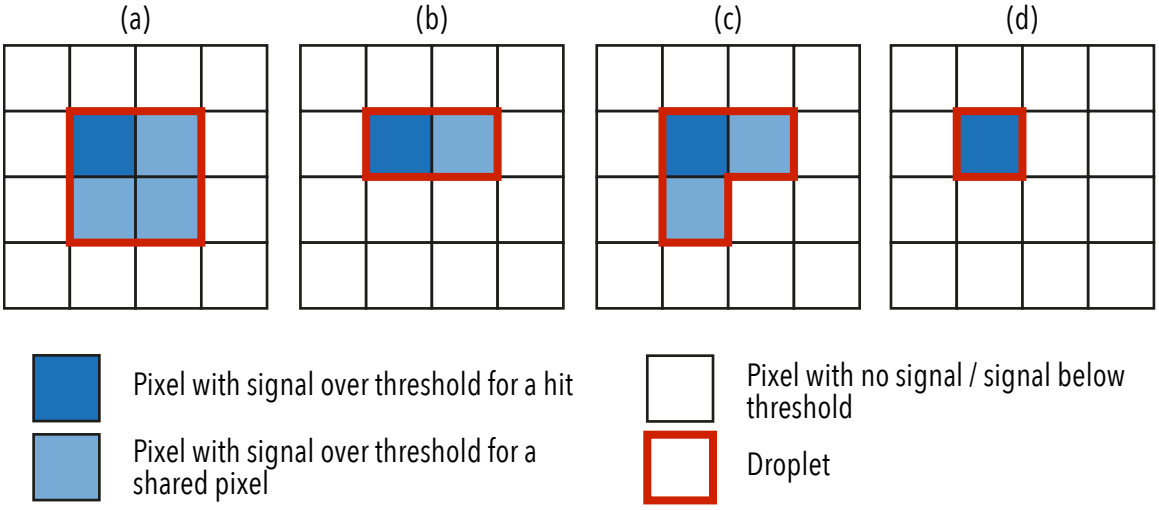

Figure 4.20: Illustration of possible ("logical") droplet shapes

From the detector's behaviour presented in ch. 4.1.2, it is obvious that the shapes shown in fig. 4.20 can be produced by one photon. In fig. 4.21 those shapes are presented that are "non-logical" in the sense that more than one photon have to be responsible. Those "non-logical" shapes need to be classified into those due to pile-up of the first kind (fig. 4.21 (c) & (d)) and pile-up of the second kind (fig. 4.21 (a) & (b)). While the latter will occur much more often, assuming a signal spread over

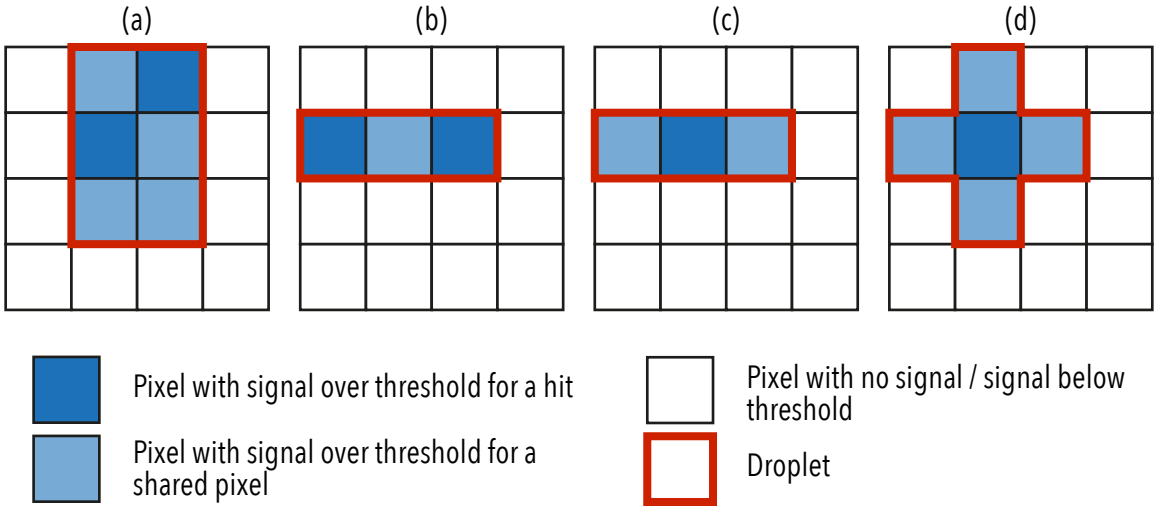

Figure 4.21: Illustration of some impossible single photon ("non-logical") droplet shapes

multiple pixels, the inaccurate recognition of pile-up of the first kind should nearly show no error. However, the main source of errors will arise from wrong decisions in removing other droplets from the droplet that is in processing.

The possible scenarios in fig 4.21, point to a problematic scenario: just considering the shape, a pile-up of the first kind can look the same as a pile-up of the second kind. Depending on the statistics, stating that pile-up of first kind is much less probable than pile-up of the second kind is reasonable. For this algorithm, the consequences of misinterpretation due to that have to be accepted.

Also for properly identified non-logical droplets, the algorithm for splitting two overlapped droplets uses the following assumption. It assumes that for potential shared pixels of both droplets half of their ADU values can possibly be part of each droplet. This means that it either happens that droplets show too high or too low ADU values. The lower signal that still lies in the ADU range for the appropriate photon energy is classified as such a photon. The lower signal out of ADU range has to be counted as a full error photon. The higher signal out of ADU range cannot be

distinguished from pile-up and has to be treated like such.

Application

Similar to the previous sections about the other preprocessing methods, in this section the algorithm is applied to actual data. In order to allow for a good comparison the same runs are to be chosen as before.

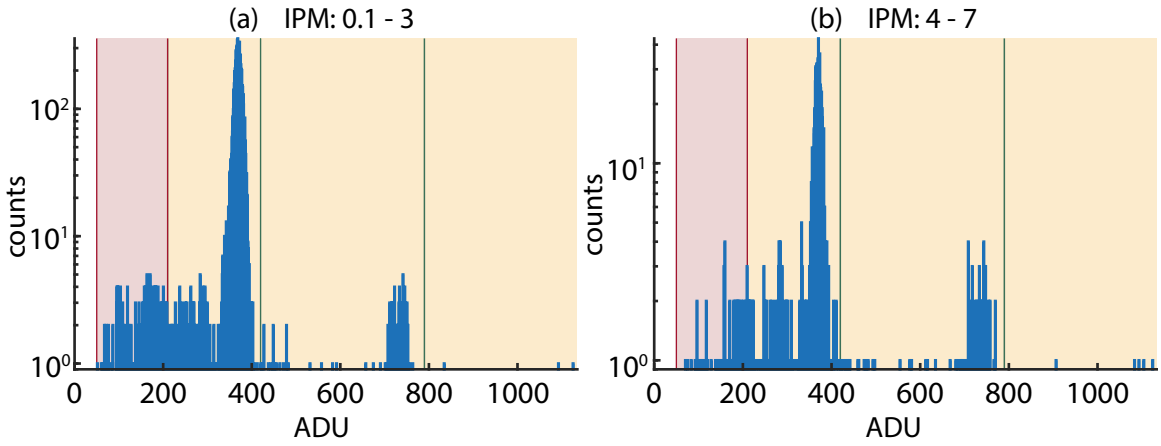

Figure 4.22: ADU histograms for run 169 with custom droplet algorithm: (a) low pulse energy range: 0.1 - 3 IPM; (b) high pulse energy range: 4 - 7

Run 169: For this run, that contains nearly no fundamental and mostly second harmonic signal, with the custom droplet algorithm in an ADU histogram a clear peak of second harmonic signal is observed, as shown in fig. 4.22. The errors occur as mentioned above. In both presented energy regimes, for ADU values lower than the SHG peak, noise occurs due to the algorithm. However, in both cases pile up photons are successfully split. Such a signal looks also like the noise, but lies in the ADU ROI of the SHG signal. As presented in the theory the efficiency of the second harmonic process is expected to depend quadratically on the pulse energy. Since higher photon rates lead to more pile-up a better analysis is done by splitting the histogram in two. One for the lower pulse energy range ($IPM2 < 4$) and one for the higher pulse

energy range ($IPM2 > 4$). For the lower range, shown in fig. 4.22 (a), much less pile up occurs than in the high pulse energy range, when compared to the number of shots associated with each regime. The algorithm shows low additional noise. For higher pulse energies it becomes clear that due to this algorithm noise signal becomes more significant. However, as long as the noise generates a lower error than other interpretation, the performance of this algorithm stands the test.

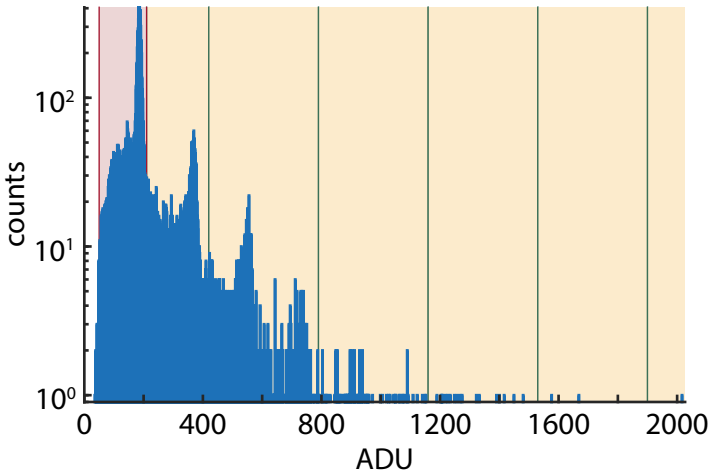

Figure 4.23: ADU histogram for run 172 with custom droplet algorithm

Run 172: Like in the previous sections run 172 is used to illustrate the case of extreme pile-up signal. As can be seen from fig. 4.23, the amount of pile up reduces itself from a lower order peak towards a higher order peak approximately by one order of magnitude. That is very close to the expectations of pile up of the first kind [20]. However, this run also shows scatter signal, but this is still about one order of magnitude below the signal contained in the peak for each interval.

Run 191: This run gives a situation in which fundamental as well as second harmonic signal can be observed. This provides an additional challenge to the presented algorithm, since the noise signal that counts as an error overlaps partially with the

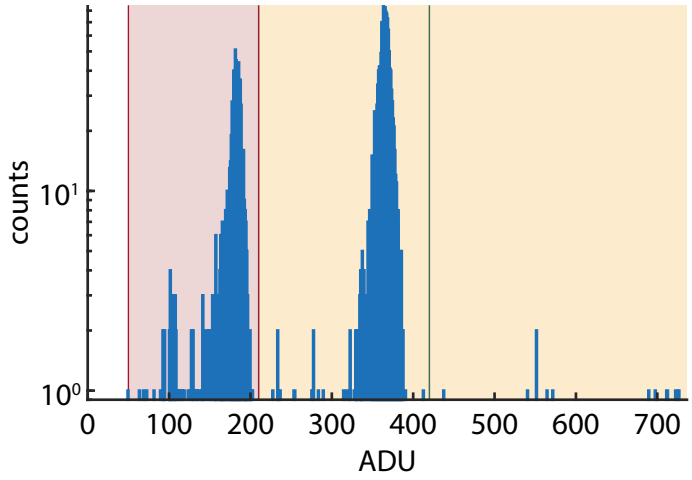

Figure 4.24: ADU histogram for run 191 with custom droplet algorithm

fundamental ADU ROI. Fig. 4.24 shows the ADU histogram after the custom droplet algorithm has been applied of that run. This run shows in general not much pile-up, which makes this algorithm not really effective. Most droplets obey the allowed shapes anyways. Especially since the artificial noise signal in the fundamental region cannot be quantified, the error due to that can just be given in an upper limit by the number of hits, that were flagged, but then the algorithm did not achieved its goals.

Conclusion & Outlook

The algorithm provides a great way to interpret data from an ePix100 detector. Especially for situations that show pile-up signal (flagged droplets), many of those are recognized and split into single photons. Due to misinterpretations by the splitting algorithm noise that contributes to the error is generated.

A further improved approach may be to fit the distribution with photons, represented by Gaussian functions that emulate the photon behaviour in the detector. For such algorithm an intense computing time is expected. Further another challenge for such algorithm would be photons of two different colors, while a shape algorithm is

not influenced by the number of colors of the photons.

4.1.5 Comparison between different approaches

To compare the performance of the different approaches especially the data from run 169 and run 191, that are both second harmonic generation runs, has to be taken into account. Run 172 was good for illustrative purposes, but does not represent data of interest.

As already mentioned in the discussion of each method, it is obvious what basic effects each method has. It is now to be discussed which method is to be used in what cases in order to generate the best results.

However, at first a general overview over the results will be given. As presented before the biggest error due to the preprocessing occurs from some artificial pile-up, called pile-up of the second kind. This pile-up is not shown by the raw data, but both versions of a droplet algorithm show it. While the droplet algorithm leads to very direct interpretations, the interpretation of the raw data is more difficult. It is in the nature of the raw data to show broad distributions with no defined single peaks in an ADU histogram in the region of interest on the detector. But also both droplet algorithms show some noise signal - meaning signal between distinct peaks, maybe due to misinterpretation and/or stray light on the detector. The custom droplet algorithm shows more noise signal, indicating more misinterpretations, and not stray light.

In order to provide a convincing comparison certain common bounds have to be set. At first it has to be clear what will be discussed. Obviously, performance concerning the determination of the amount of second harmonic and potentially fundamental signal shall be compared. Additionally, the errors also have to be taken into account. Moreover with regard to the droplet, it may be of interest from what signal errors

arise, meaning from signal in potential pile-up peaks or from noise signal. The results from that comparison can be used to get a better impression of possible improvements to the customized droplet algorithm.

Run 169: This run is a good starting point, because as can be seen from the sections where the methods are analyzed, this is a run that shows nearly no fundamental signal, so that its contribution can be neglected. In the comparison, two characteristic regimes will be discussed. A low/medium and a high pulse energy interval, in terms of IPM values, is chosen. Those are $0.1-3$ and $4-7$. The errors in this region should be dominated by pile-up and not by counting statistics. In general this section discusses only errors due to the selected analysis method.

For the low/medium pulse energy range the second harmonic counting rates lie below 1%, while here the raw data shows nearly no pile-up, also both droplet algorithms show only the same very few pile-up counts. In direct comparison the standard droplet methods gives more reliable results only because the customized one shows some more noise signal in the fundamental region. At highest pulse energies the standard droplet algorithm shows pile-up from up to seven photons, while that raw data clearly indicates that there is only real pile-up up from up to three photons. The customized droplet algorithm shows its strengths. It can reduce pile-up to the 3rd order and further the droplet splitting algorithm can reduce the overall error by over 11% absolute, translating to over 16% relative error, compared to the standard algorithm.

Run 191: Run 191 is a complicated run, since the data set shows two colors of photons. It contains nearly no pile-up signal, which is why the custom droplet algorithm cannot show its strengths. It results with this algorithm in more noise signal.

The raw data, as can be seen from fig. 4.10, is also affected by the two color overlap. Especially the fundamental signal has some significant error, but also the second harmonic signal can be determined only with an uncertainty of 20%. However, the standard droplet algorithm shows clear peaks and nearly no pile-up signal. It is the algorithm of choice for this run. Because of the low number of pile up no analysis of two different pulse energy domains is necessary.

Conclusions: The droplet algorithm is to be used for signals that show no or very low pile-up. The sharp peak and minimal noise signal allow for a clean interpretation, without losing the low error in the signal. For runs that show medium pile-up signal, it is to a case sensitive decision, in such a regime it not clear whether the pile-up error with the standard droplet overcomes the error due to noise signal in the custom droplet method. For signal with large pile-up signal, but still with the intention to find single photons, the raw data may be taken as base, though also only one color is allowed in the signal, otherwise the custom droplet algorithm has to be chosen. In general the raw data is not to be considered as a reliable method. Though the basic principle can be simulated, as of now we have no simulation that is sophisticated enough to allow for a good fit. This results at this time in large uncertainties about the number of photons. Those result in large errors. The signal with more noise that can be observed using the customized droplet algorithm points towards too general assumptions and methods. The method to split droplets needs to consider more circumstances than only parts of the direct neighborhood of the peak pixel.

Altogether analyzing three possible methods for data analysis shows that the droplet algorithm is still to be considers the best all-round tool. Though when allowed to do case sensitive decision on the algorithm, the custom droplet algorithm will be useful in many cases.

4.2 Detector Calibration: IPM to pulse energy

The calibration of the IPMs for the pulse energy scale can be made using a power meter originally designed for optical lasers, which is provided at the XPP beamline. Therefore, during the beamtime, the value displayed by the instrument was calibrated to an averaged IPM3 signal. However, typically the IPM2 is a better choice to provide a general pulse energy scale, since it is placed before any attenuator, that would reduce the signal to noise ratio. So at first, the IPM2 sum is correlated to the IPM3 sum and then a scale can be set. The IPM values are expected to increase linearly with the pulse energy [22].

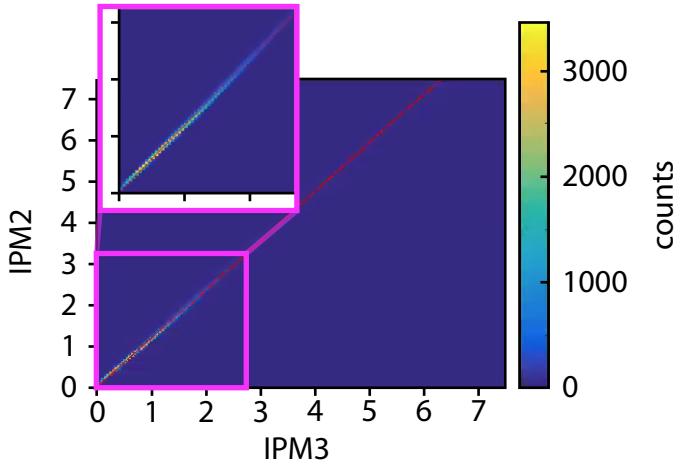

Figure 4.25: IPM3 to IPM2 calibration with run 169

On September 29 at 9:50 AM an IPM3 average around 1.0 relates to ca. $85\,\mu$J shown by the power meter. According to a beamline scientist, the real pulse energy is roughly lower by a factor of 2 to 3 than the one displayed [53]. Hence 1.0 on IPM3 relates to a pulse energy range of $27-43\mu J$, thus an average pulse energy of $35\pm8\mu J$. An average of 1.0 on IPM3 relates to an average of 1.19 ± 0.04 (error given by rms on fit) on the IPM2.

4.3 Experimental Results & Comparison with Simulation

The parameters of interest for this experiment are the photon rate and the efficiency of the second harmonic process for different phase-matching conditions. In this section, resulting efficiencies and their angular dependence is presented. Further, the dependence of the second harmonic photon rate on the pulse energy and data on the angular acceptance of each reflection are presented. Details on some errors are given in the separate section 4.3.4 "Error Analysis".

4.3.1 Efficiency

During the experiment for most of the investigated crystal geometries, particular datasets at the angle of incidence with maximum second harmonic photon-rate were recorded. Those runs consist of many shots, to ensure proper counting statistics (see also ch. 4.3.4). This section uses if existing, data from those runs. Furthermore, this section will show a derivation of an equation to calculate the efficiency and its error from experimental data. Furthermore, it will present values for the efficiency and compare it to a theoretical simulation done by Priyanka Chakraborti.

The efficiency rate for the process is defined to be the number of generated second harmonic (SH) photons divided by the number of incident fundamental photons. So it can be calculated from the incident light and the generated light. The average number of incident photons, i_{fund}, (normalized per shot) with the fundamental photon energy, $E_{ph,fund}$, can be calculated from the average pulse energy.

$$i_{fund} = \frac{E_{pulse,avg}}{E_{ph,fund}} \tag{4.1}$$

$E_{pulse,avg}$ can be obtained from the average IPM2 signal per shot, $IPM_{2,avg}$. For the

conversion of the calibrated IPM3 signal, we find the pulse energy per IPM3 with $E_{pulse,IPM3} \approx 35 \pm 8 \frac{\mu J}{pulse}$. From the data, a conversion factor from IPM3 to IPM2, IPM_{conv}, can be obtained (see ch. 4.2).

$$E_{pulse,avg} = E_{pulse,IPM3} \times IPM_{conv} \times IPM_{2,avg} \tag{4.2}$$

The number of generated second harmonic photons, n_{sh}, can be obtained from the counts per shot on the detector (in the desired energy range) $n_{det,sh}$ with the knowledge of the Transmission, T_{sh}, of the filter used in front of the detector and the detector's quantum efficiency, η_{det}.

$$n_{sh} = \frac{n_{det,sh}}{T_{sh} \times \eta_{det}} \tag{4.3}$$

During the experiment it has to be shown how high the second harmonic background of the incident light is. In case it would be too high to be neglected, the number of incident second harmonic photons (normalized per shot), i_{sh}, together with the reflectivity of the crystal depending on its orientation due to Bragg reflection, $R_{sh,bragg}$, have to be considered.

The overall efficiency of the process η_{SHG}, neglecting i_{sh}, is given by:

$$\eta_{SHG} = \frac{n_{sh}}{i_{fund}} \tag{4.4}$$

$$\eta_{SHG} = \frac{n_{det,sh}}{T_{sh} \times \eta_{det}} \times \frac{E_{ph,fund}}{E_{pulse,IPM3} \times IPM_{conv} \times IPM_{2,avg}} \tag{4.5}$$

When approximating the error distributions of the measurements and conversion

factors to follow a Gaussian distribution, the error in the efficiency is given by:

$$\begin{aligned}\Delta\eta_{SHG} = \Bigg[&\left(\frac{1}{T_{sh}\times\eta_{det}} \times \frac{E_{ph,fund}}{E_{pulse,IPM3}\times IPM_{conv}\times IPM_{2,avg}}\Delta n_{det,sh}\right)^2 \\ &+ \left(\frac{n_{det,sh}}{T_{sh}\times\eta_{det}} \times \frac{E_{ph,fund}}{E^2_{pulse,IPM3}\times IPM_{conv}\times IPM_{2,avg}}\Delta E_{pulse,IPM3}\right)^2 \\ &+ \left(\frac{n_{det,sh}}{T_{sh}\times\eta_{det}} \times \frac{E_{ph,fund}}{E_{pulse,IPM3}\times IPM^2_{conv}\times IPM_{2,avg}}\Delta IPM_{conv}\right)^2 \\ &+ \left(\frac{n_{det,sh}}{T_{sh}\times\eta_{det}} \times \frac{E_{ph,fund}}{E_{pulse,IPM3}\times IPM_{conv}\times IPM^2_{2,avg}}\Delta IPM_{2,avg}\right)^2\Bigg]^{1/2}\end{aligned} \tag{4.6}$$

To reduce the error in the efficiencies, we use a narrow distribution of the pulse energies. Since the XFEL has large fluctuations in photon energy and the LODCM (see ch. 3.1.2) transmits only a narrow, fixed bandwidth of that into the beamline, the transmitted intensity fluctuates significantly. The range of intensities was limited in the analysis by only analyzing data where the shots lie within a fixed energy (IPM2) range. This was determined to be 2 to 3 IPM2 because this is a range in which many SH photons were measured and a large statistics of shots could be detected. This translates to an average pulse energy of $70 \pm 20\,\mu J$.

The count rates on the detector and their errors can be ascertained using either of the two droplet algorithms. For runs that show some pile-up, with the custom droplet algorithm improvements in the positive error of over 9% are achieved. It can be shown that for the more extreme case the positive error can be reduced by more than 37%.

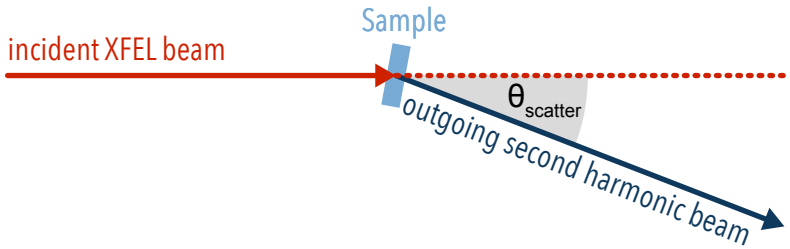

Figure 4.26: Illustration of the scattering angle $\theta_{scatter}$

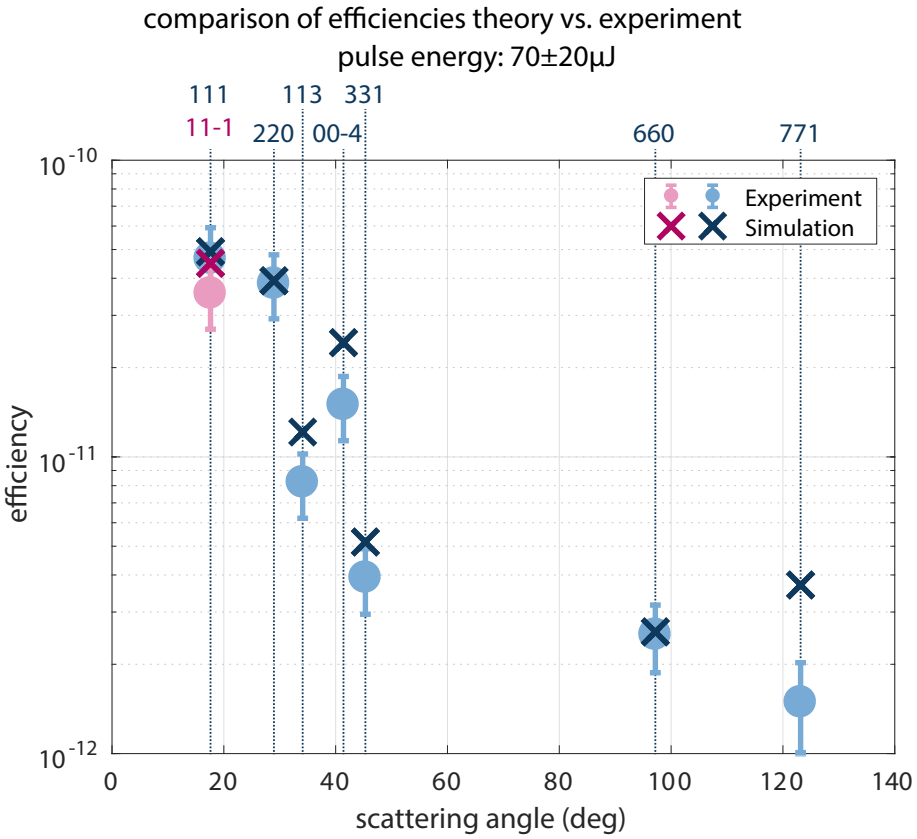

Figure 4.27: Efficiency vs. phase-matched scattering angle; there are different scattering angles due to different phase-matching conditions for different planes. Since the scattering angles for the (111)- and $(11-1)$-geometries are equal, in order to differentiate between the data points two different colors ($(11-1)$: red & (111): blue) are used. Deviations from a tendency of high efficiencies at low scattering angles, are explained by different propagation lengths in the sample, as well as different lengths until saturation occurs. The error was calculated using eq. 4.6.

The resulting efficiencies (obtained by using the better result of both algorithms) are compared to theoretical simulations (see fig. 4.27). It can be seen that there is a good overlap with the theory for all angles. Walk-off effects explain the decrease of the efficiency towards larger scattering angles. Those get more severe because the spatial and temporal overlap between the coupled fields is shorter. The fundamental beam acts as a pump for the generated second harmonic fields. The sample's dimensions may explain deviations from that overall tendency. It allows for each reflection

different propagation lengths, since as shown in table 3.1 in ch. 3.1.4, the angle between sample's surface and incident beam varies. A big contribution to the overall errors arises from the uncertainty on the measurements delivered by the power meter, made to reconstruct the pulse energy. However, the pulse energy fluctuation within the selected IPM2 range also participates with a significant amount. Since counting statics (see ch. 4.3.4) appear to be no major contributor to the error at this point, further, but slight improvements to the error can be made by narrowing the pulse energy down further, as it will be done in the following section.

4.3.2 Pulse energy Dependence

As it could be shown in the previous section, the desirable counting statistics of the data allow for a fine binning of the pulse energies. To show the pulse energy dependence in this section, a dependency will be plotted regarding IPM2 values. This is because the IPM2 values scale linearly with the pulse energy and the translating factor comes with a significant error as presented before. So the IPM2 values are equivalent to an energy scale in arbitrary units. The intensity will be given regarding the effective 2ω-count rate, which is expected to scale quadratically with the pulse energy. The effective count rate is the measured 2ω-count rate corrected for filter transmission and quantum efficiency of the detector. Since higher pulse energies expect higher count rates, hence more pile-up, this section will always compare the results of both droplet algorithms.

In the previous section, an efficiency was derived and calculated, which represents the relation of the incident fundamental to the generated second harmonic photons. It is not only specific for the focal parameters, the sample, and the general beam properties, it also depends on pulse properties, meaning those that vary pulse to

pulse. In this case, pulse properties refer, especially to the pulse energy. Properties like pulse duration or source point, which affects the focus, are assumed to be stable. This problem leads to the goal of this section, that is to define another kind of efficiency that depends on fewer parameters and to find a factor that relates to that new efficiency.

One approach for this is to use the non-linear relation of the incident to the generated electric field, as presented in ch. 2.1.5. For this, an efficiency η_{NL}, called in the following "nonlinear efficiency", can be defined as:

$$\boldsymbol{E}_{2\omega} = \eta_{NL} \cdot \boldsymbol{E}_{inc,\omega}^2 \tag{4.7}$$

, where $\boldsymbol{E}_{2\omega}$ is the electric field of the outgoing SH photon pulse and $\boldsymbol{E}_{inc,\omega}$ is the electric field of the incident fundamental photon pulse. This relates to a quadratic dependence regarding the photon rates. Further a possible second harmonic background signal that was Bragg reflected or background due to the pile-up of the fundamental signal is to be considered. Such a background scales linearly with the incident pulse energy. Furthermore, a possible noise signal is taken into account. This results in a polynomial of second order. The data will be fitted for

$$n_{2\omega} = a \cdot IPM_{2,avg}^2 + b \cdot IPM_{2,avg} + c. \tag{4.8}$$

This way the factor a that relates to the non-linear efficiency is independent of the pulse energy. A direct conversion between both parameters is not possible at this point, since the exact parameters, like the pulse duration of the generated second harmonic, are unknown.

The dependence of the effective count rate on the pulse energy for several crystal

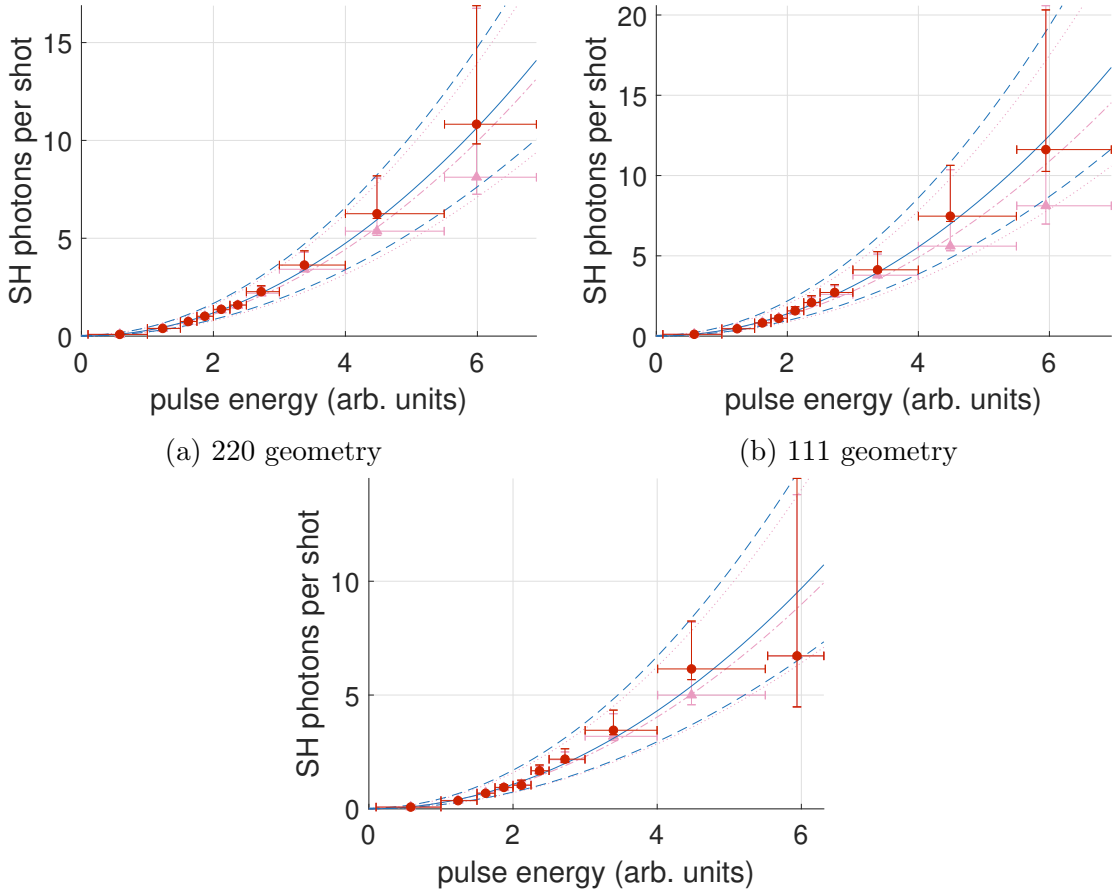

(a) 220 geometry

(b) 111 geometry

(c) 11-1 geometry

Figure 4.28: SH photons per shot vs. pulse energy (IPM2); For the shown planes clear advantages can be obtained by the use of the customized droplet algorithm; the red data points and the blue fits are based on data obtained with the custom droplet algorithm, while the light pink data and fits were obtained by applying the standard droplet algorithm to the raw data; the fits were done using the function $ax^2 + bx + c$, where the fit-parameter a, b, c are limited to positive values. This results in all cases in $b \approx 0, c \approx 0$.

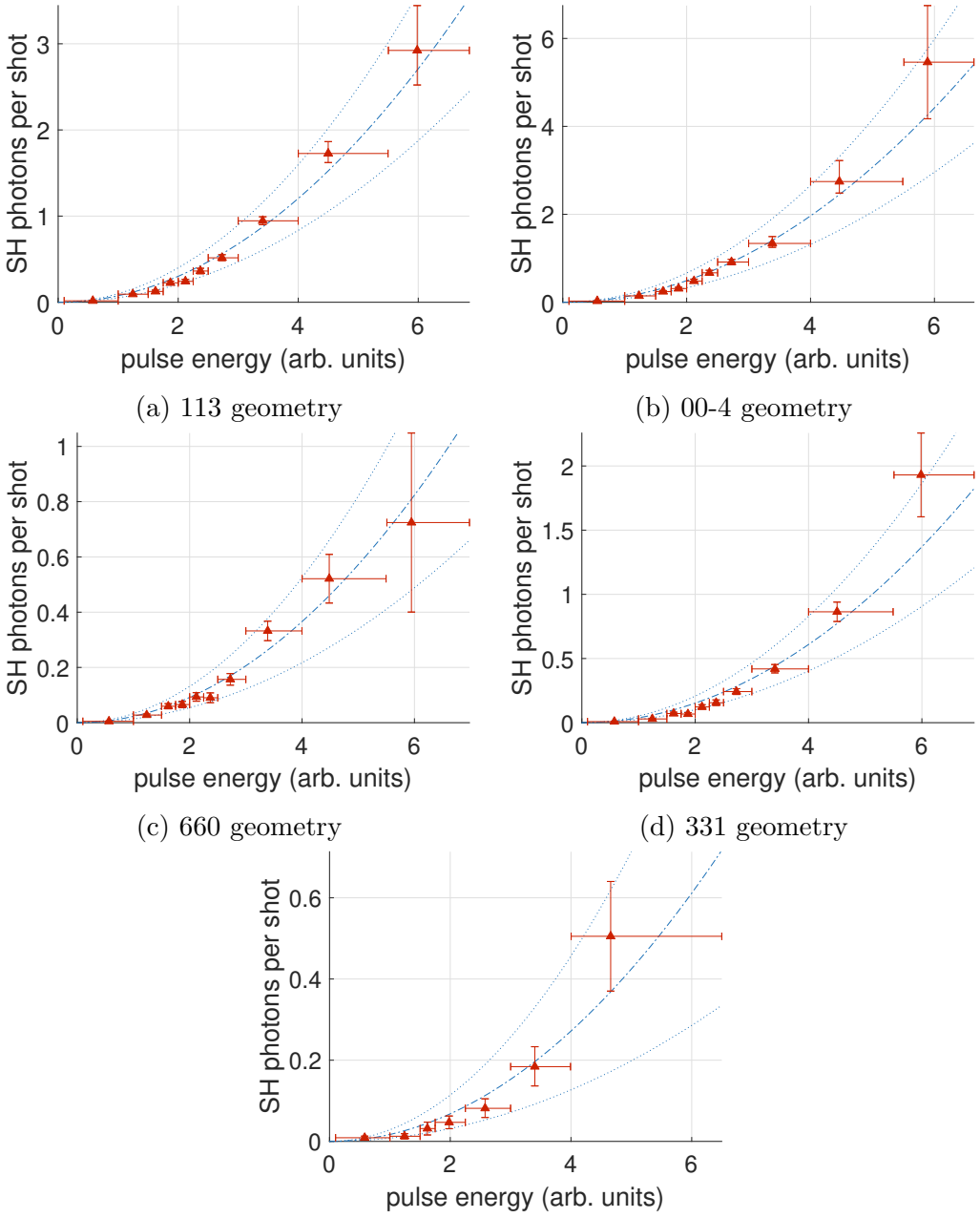

(a) 113 geometry

(b) 00-4 geometry

(c) 660 geometry

(d) 331 geometry

(e) 771 geometry

Figure 4.29: SH photons per shot vs. pulse energy (IPM2); For the shown planes no advantages or even disadvantages compared to the standard droplet algorithm are obtained by the use of the customized droplet algorithm; the red data points and the blue fits are based on data obtained with the standard droplet algorithm; the fits were done using the function $ax^2 + bx + c$, where the fit-parameter a, b, c are limited to positive values. This results in all cases in $b \approx 0, c \approx 0$.

planes in diamond is shown in fig. 4.28 and 4.29. From the plots in these figures, the expected quadratic dependence is observed for all planes within the error ranges of the data points. Hence the developed theory appears to be valid in this regime. This also validates the approach to find an efficiency with a quadratic dependence on the incident field. Furthermore, the plots show for each data set a comparison between the performance of both droplet algorithms. Those presented in fig. 4.28 show reflections where the custom droplet algorithm can provide some improvement and for those in fig. 4.29, the standard droplet gives better results. The fits further show that there is no or nearly no background or noise signal ($b, c \approx 0$).

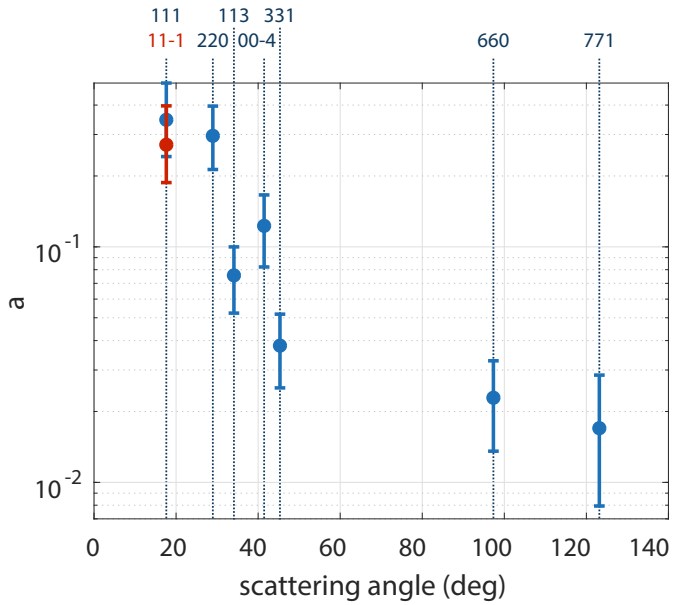

Figure 4.30: Fit parameter a vs. phase-matched scattering angles; there are different scattering angles due to different phase-matching conditions for different planes. Since the scattering angles for the (111)- and $(11-1)$-geometries are equal, in order to differentiate between the data points two different colors ($(11-1)$: red & (111): blue) are used. Data shows qualitatively the same behaviour as fig. 4.27

With the obtained efficiency related parameter a as in the previous section an angular dependence can be plotted. Such a plot is shown in fig. 4.30. The plot shows qualitatively the same behavior as the data in fig. 4.27. Note that a scattering angle

of 90 degrees means scattering into the polarization direction of the FEL fundamental. This is highly suppressed for linear scattering, but the nonlinear scattering shows a finite value, which is expected from the $\boldsymbol{J}_{2\omega}$ source term in chapter 2.1.5.

4.3.3 Crystal Rocking Curves

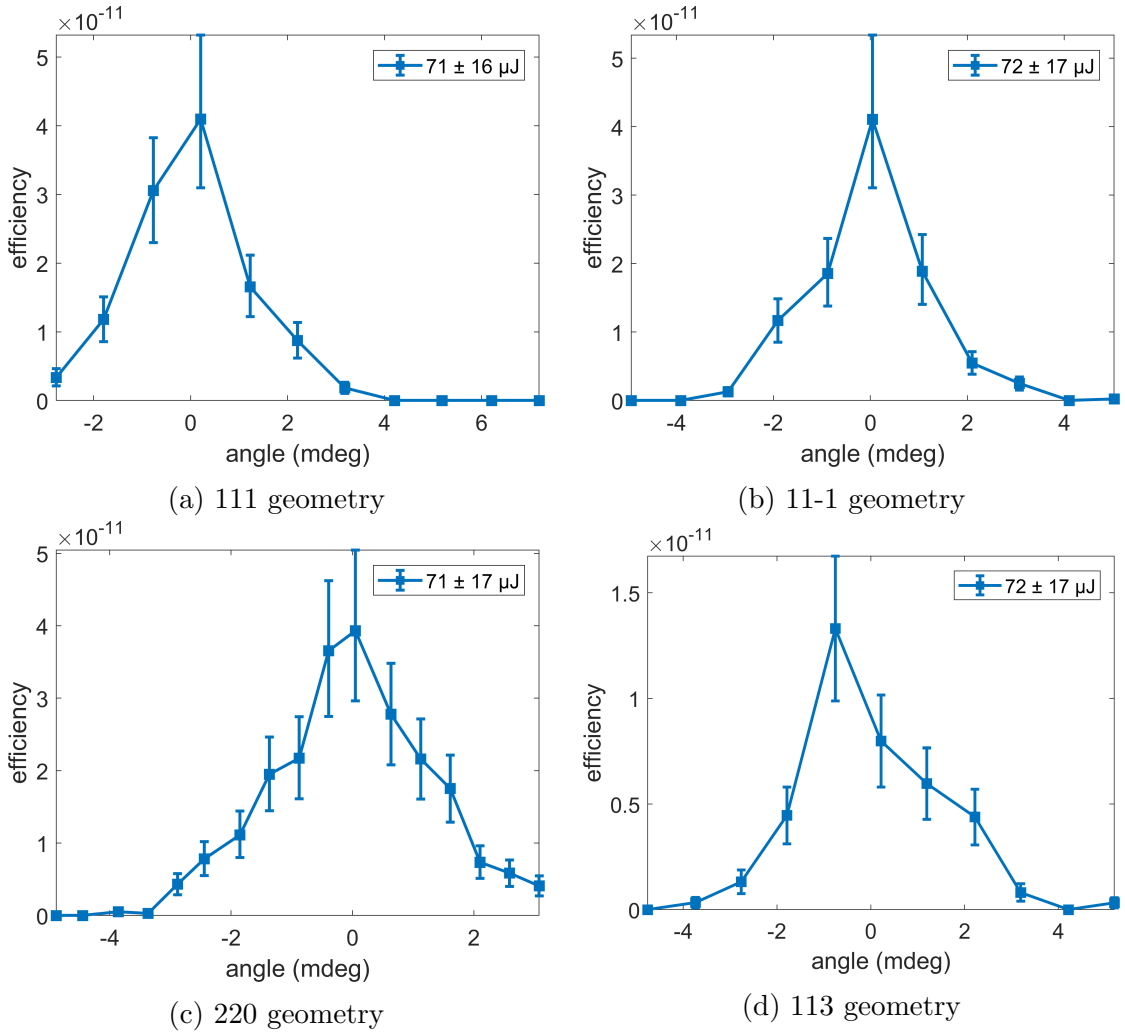

(a) 111 geometry

(b) 11-1 geometry

(c) 220 geometry

(d) 113 geometry

Figure 4.31: rocking curves

The small-angle emission near a phase-matching condition is measured using rocking curves. In a rocking curve measurement, the crystal is rotated, while the detector remains at the same scattering angle. In this thesis for all reflections presented before,

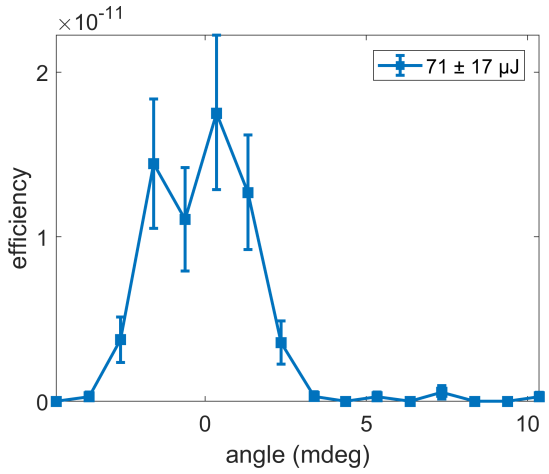

(a) 00-4 geometry

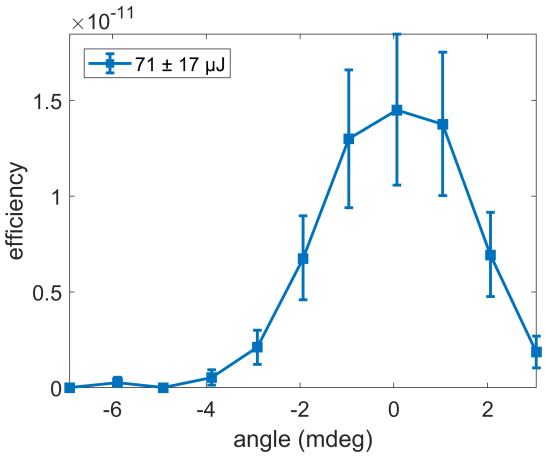

(b) 00-4 geometry

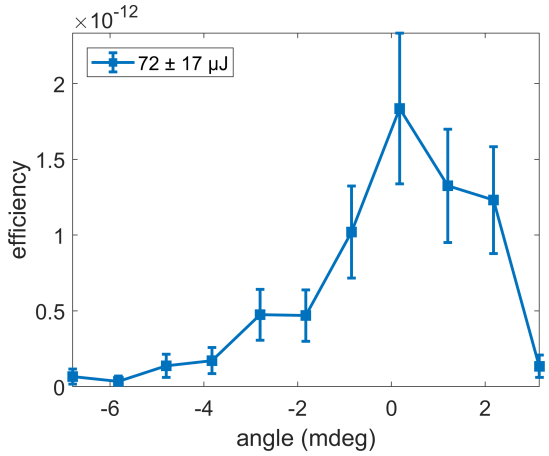

(c) 331 geometry

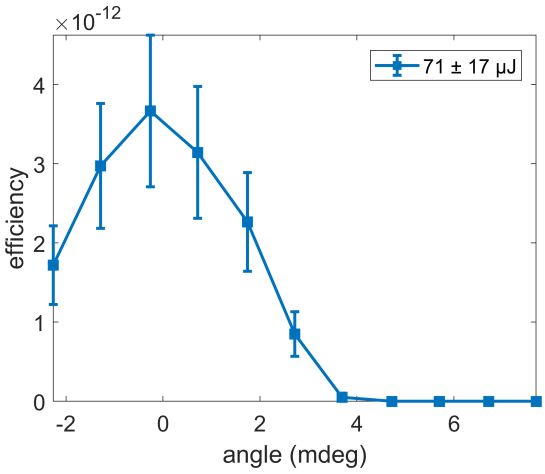

(d) 660 geometry

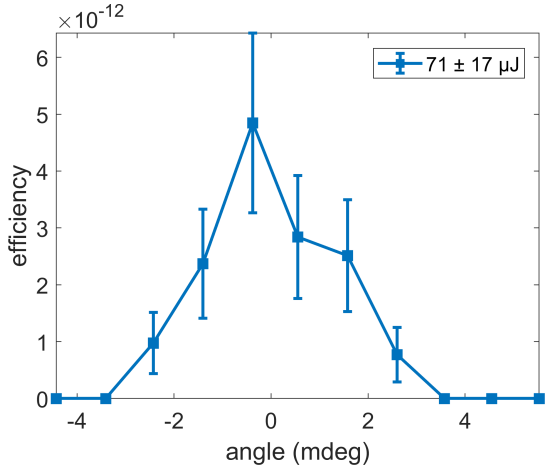

(e) 660 geometry

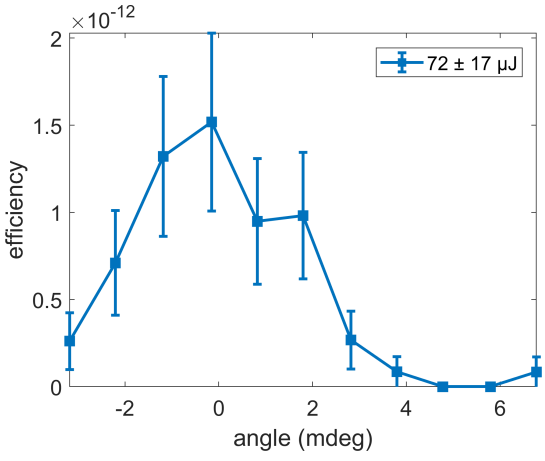

(f) 771 geometry

Figure 4.32: rocking curves

also rocking curves are reported. All presented rocking curves are generated using the standard droplet algorithm. The rocking curves are shown in the fig. 4.31 and 4.32 . The here presented rocking curves all relate to a pulse energy of $70 \pm 20\,\mu J$. Rocking curves also for other pulse energies are shown in appendix B.

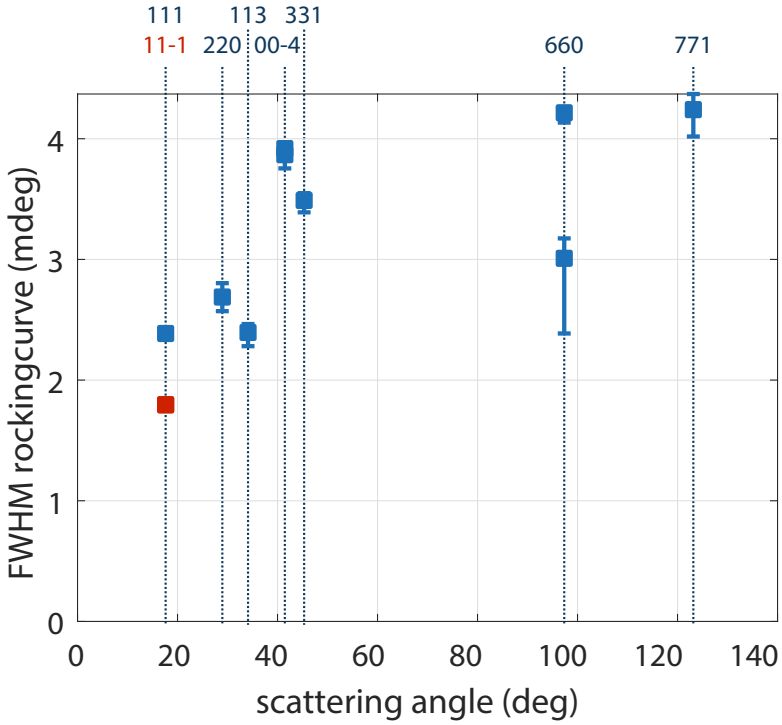

Figure 4.33: Dependence of the full width half maximum (fwhm) of the rocking curves on the phase-matched scattering angle; for the geometries $(00-4)$ and (660), 2 rocking curves were recorded. Since the scattering angles for the (111)- and $(11-1)$-geometries are equal, in order to differentiate between the data points two different colors ($(11-1)$: red & (111): blue) are used.

The dependence of the rocking curve on the phase-matched scattering angles can be visualized by using the full width half maximum (fwhm) value of the rocking curves as a measure. As a result of such approach fig. 4.33 shows that larger scattering angles correspond to wider rocking curve and hence a wider angular acceptance.

4.3.4 Error Analysis

The quality of a measurement depends mainly on two factors: the quality of the method used to measure a particular process and the quality of the process itself. Further, for the resulting data, as could be seen from previous sections, also the method of analysis and interpretation can influence the quality of the results significantly. The latter was extensively discussed in ch. 4.1 and will not be discussed here.

First, the quality of the process itself will be discussed. Depending on many parameters, second harmonic generation occurs in the diamond crystal at a certain rate. Together with the attenuation in front of the detector and its quantum efficiency, a certain photon rate is measured. These circumstances make the experiment eligible to be described using Poisson statistics [49]. The assumption is made that the counts N measured in the interval I are approximately the average number of counts $\bar{N}$ that would be measured when repeating this measurement many times ($N \approx \bar{N}$). From this, the standard deviation is given by $\sigma = \sqrt{N}$. Though σ increases for a higher number of counts, the relative error for N average counts, which goes as $\frac{\sigma}{N} = \frac{1}{\sqrt{N}}$, decreases. That shows in general: A larger number of counts per data point result in a lower relative error.

Looking at the quality of the measurement, effects due to the detector must be considered. Due to the high efficiency of the ePix100 detectors, misdetection of photons can be neglected. However, as already presented in this thesis, pile-up effects may lead to misinterpretation of the signal by the detector and must be considered. Detailed information on the estimation of pile-up (of the first kind) can be found in ref. [20]. Since it is not possible to differentiate between harmonic signal and pile-up, it cannot be simply corrected for and must be considered as error. Due to the clean

signal on the detector, the error due to pile-up is determined by counting the number of droplets in the ADU ranges associated with the appropriate order of pile up / harmonics. The value is calculated by assuming that each potential pile-up signal contains n photons according to the order $n-1$ of the pile-up associated with the ADU ROI.

Since the efficiency η_{SHG}, defined in ch. 4.3.1, depends on the pulse energy and hence on the IPM values, those are a significant error contributor. Where the IPM calibration relates already to a relative error of ca. 20% and the range of pulse energies have a relative error of ca. 10% (rms). Here, counting statistics are not a crucial contributor since only the very high pulse energy regimes lack a high number of shots. Also, pile-up effects are mostly expected in the higher pulse energy ranges.

However, the effective count rate, discussed in ch. 4.3.2, is not calculated using the pulse energy. So here, effects contributing to the error, such as count rate and pile-up, are of major interest. While the counting statistics contribute symmetric to the error, pile-up or noise signal from the custom droplet algorithm counts towards the positive error only. Thus the contributions can be estimated well from the figures 4.28 and 4.29 directly. It becomes clear, that especially for higher pulse energies, the errors increase. This is explained by the Poisson-like distribution of pulse energies reaching the beamline, as well as by the high photon rates reaching the detector what increases the probability of pile-up.

The results on the angular acceptance presented with rocking curves in fig. 4.31 and 4.32 follow the same approach as for efficiencies, so the error contributions due to the pulse energy calibrations are the same. However, opposite to the efficiency datasets on a fixed angle, each angle consists of fewer shots. This leads to worse counting statistics showing a contribution between 0 and 10%.

Chapter 5

Conclusion & Outlook

In this work, we investigate X-ray second harmonic generation (XSHG) for various geometries. For the diamond (220) geometry, phase matching of the second harmonic generation has previously been shown to agree with theoretical calculations [46]. For other geometries and scattering angles, the accuracy of the theory had remained an open question. We were able to answer that question using new experimental data. The novel data analysis algorithm described in this thesis has improved the accuracy of the data sets. The algorithm is a result from a better understanding of the detectors that were used in the experiment.

Since XFELs have become available only recently, it is an exciting time to explore the new regime of ultra-fast, nonlinear X-ray interactions.

To improve automated signal interpretation of the used pixel detectors, a detailed analysis of existing methods was performed. Several pathways for improvement were identified and a new algorithm, based on existing approaches and improvements, was built from scratch. The algorithm has led to a better understanding of the measured signal and has decreased the measurement uncertainty. In particular, it has improved the measured photon energy width and the interpretation of the observed detector histograms. The algorithm works by identifying and analyzing ambiguous detector signals. To this end, the algorithm identifies the problematic signal by the shapes

of the pixel signal due to photon hits on the detector. An irregular shape, which relates to multiple photon hits, is then split into multiple defined shapes, one for each photon. This work is ongoing, and further improvements are expected.

The best results are usually expected when an analytical method is tailored to each data set. This requires a considerable amount of fine tuning, but here this method has been shown to reduce the detector error as much as 37%. For proper analysis, results from this new and established methods have to be compared for each data-set. It has been shown that the common algorithm performs well for very low photon rates per pixel, though for photon rates that are close to the limit for single photon counting, the improved algorithm is at an advantage.

The experimental obtained efficiencies are in good agreement with simulated efficiencies (simulation by Priyanka Chakraborti). This verifies the validity of the applied models and the developed theory [51]. Efficiencies for the second harmonic generation process at 9.831 keV in diamond for different phase-matching angles are presented. The resulting angular dependence in efficiency is influenced by walk-off effects and by the dimensions of the sample. The qualitative shape agrees with proposed theoretical results [51]. For smaller scattering angles the efficiency increases. It was also found that pulse energy vs. photon rate had the expected quadratic dependence. Accounting for these effects, the data infers that the SHG signal was recorded with almost no FEL background second harmonic signal or noise. In addition to the peak efficiency for different reflections in the crystal, also rocking curves showing the angular acceptance of the effect for each reflection are reported.

The further improved algorithm for ePix detector data interpretation is to be considered as a step towards a reliable algorithm for single photon counting at higher photon rates. As of now, the most significant error of the algorithm presented here

comes from the inaccurate splitting of the multiphoton signal. Further steps towards a next generation algorithm can be made by fitting the photon's signal. This way photon hits cannot only be located with sub-pixel resolution but also overlapped photon signal reliable separated. Currently, researchers from McGill University and SLAC are working on an algorithm based on such an approach.[48, 42]

The rate of X-ray sum frequency generation (SFG) will rise rapidly with the advent of the next, superconducting XFEL generation that will operate at MHz repetition rates. This will allow to use nonlinear effects as diagnostics or as applications. The much higher repetition and thus data rates, requires reliable and automated signal interpretation. It is expected that in the future, novel methods for probing condensed-matter will be provided by nonlinear X-ray mixing processes like X-ray SFG. For instance, X-ray-optical SFG processes can be used to study polarization dynamics by directly probing valence charge on the atomic time and length scales. Further applications can be in diagnostics of the FEL pulse itself. For example, the effect can be used to measure pulse duration or pulse intensity. Moreover, the detailed understanding of the mechanism of XSHG as well as SFG provides a basis for higher order effects, which have the potential to lead to novel probes with resolution on the atomic scale.

Appendix A

Detector Simulation Code

The detector simulation code is able to simulate the distribution of electrons, hence also of ADU values, across the detector caused by one or two photons. Furthermore it can apply an algorithm that works analogue to the standard droplet algorithm in preprocessing onto the data and plot a histogram over the resulting droplet sizes for three cases. These cases are at first just one photon hitting the detector and may share pixels, at second two photons hitting the same pixel and may share pixels and at third two photons hitting the detector random within a defined range of pixels relative to each other. To define this range, changes in "dropletSizeSimulator_pileup2nd" (see ch. A.2.3) have to be made.

In the main script (see ch. A.2.1) are some basic parameters that can be adjusted: the number of photons simulated (*samples*), the number of electrons simulated per photon (n), the standard deviation of the charge distribution on the detector to simulate (*all_radii*, multiple possible; in the code *radius* refers to the standard deviation), the threshold for a shared pixel to be counted & the threshold for a peak to be found (similar to preprocessing droplet algorithm) and whether an extended detector area for each hit will be considered (*extended*, true: 5×5, false: 3×3).

The pixel array: One very important structure in this code are the pixel arrays, that are returned by the "pixel_hit_simulator" (see ch. A.2.2): Those are flat arrays

that represent the pixel of a 3x3 or 5x5 area. The assignment for array positions on positions on the map are shown in figure A.1.

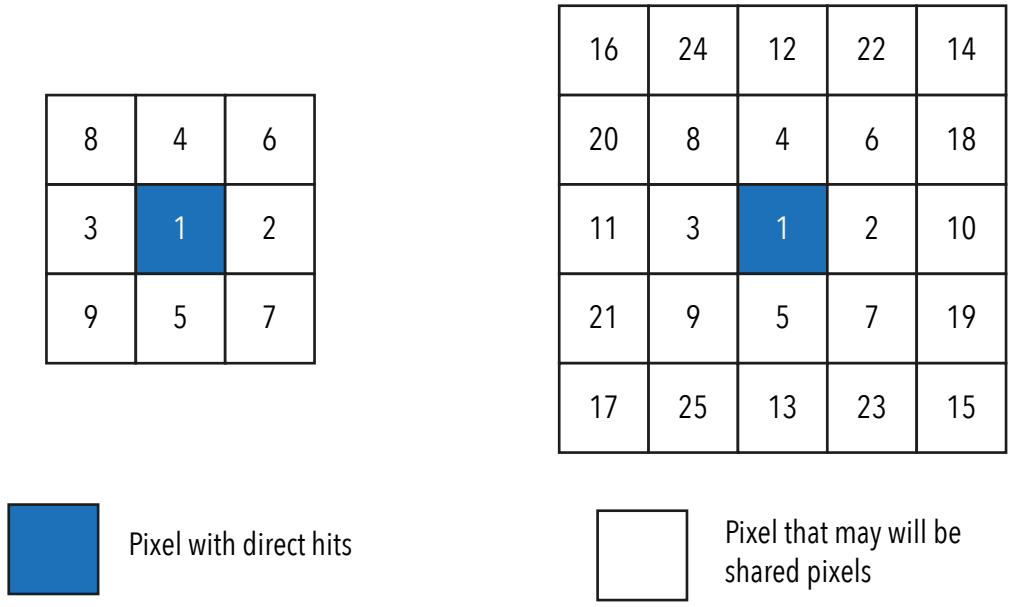

Figure A.1: Assignment of positions in pixel array returned from pixel_hit_simulator-function onto the 3×3 or 5×5 2d map of pixels

A.1 Droplet Size Simulation

In the droplet size simulation code, the first and second case (1 photon or 2 photons on the center pixel) can be realized very straight forward. The third case where two photons hit different pixels within a defined range has been coded by using the simulation data for two independent pixels as in case two and then by overlapping those in "dropletSizeSimulator_pileup2nd" (see ch. A.2.3) in a somewhat random way. Therefore ranges for the displacement of the center positions (maximum displacement limited by the bounds of the considered droplet area, 3×3 or 5×5) can be defined in that function, the pixel maps are placed on a 5×5 or 9×9 map and summed up. Then the standard procedure to find the size with the recursively applied function

"pixelWalker" (see ch. A.2.5) continues.

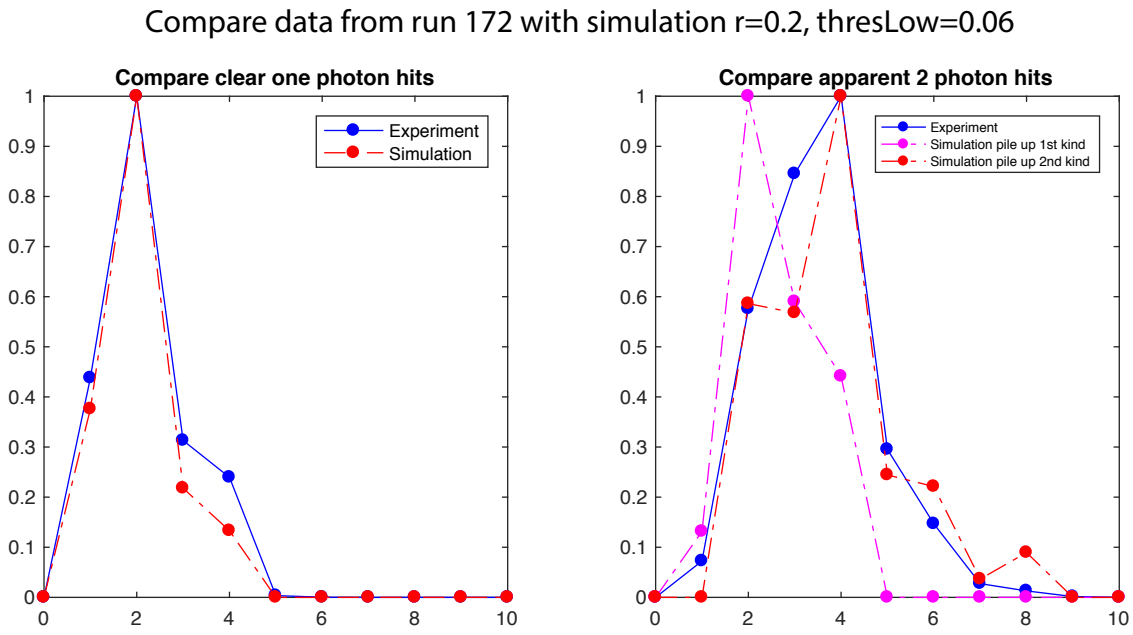

Figure A.2: Compare normalized droplet size distributions of experimental data (run 172) with simulation data (standard deviation 0.2 *pixel widths* equals 10 μm, threshold for shared pixel 0.06 *photons*. x-axis: droplet sizes, y-axis: normalized scale for number of droplets

The results of the simulation (one example shown in fig. A.2) show clearly that droplets with an area of up to 8 pixels can only be reached by the virtual pile-up caused by the data interpretation by standard droplet algorithm. The simulation verifies the arguments presented in chapter 4.1.3.

The simulation of second kind pile-up also shows that out of 25000 photons that hit pixel in maximum ±2 pixel to the right or left distance, only 5238 photons (ca. 21%) do not result in a pile-up. For only pile-up of second kind obviously only 20% of those hits would result in a pile-up. Assuming the range of that second kind pile-up is confined to ±2 pixel (but also not smaller) for any center pixel, it will give always a pile-up signal that is overestimated by a factor of ca. 4.

A.2 Code

Version of 09/19/2017 11:55 am.

A.2.1 Main Script

```
samples= 25000; %number of photons
n=400; % number of electrons simulated per photon
all_radii=[0.05,0.1,0.15,0.2]; % mean free path lengths to consider
threshold_droplet=0.12; % threshold for shared pixel
threshold_droplet_peak=0.2; % threshold for peak
extended=true; % allow droplet to spread on 5x5 (true) or 3x3 (false)
% arrays to store dropletsizes
dropletsizes=zeros(max(size(all_radii)),samples);
dropletsizes_2=zeros(max(size(all_radii)),samples);
dropletsizes_3=zeros(max(size(all_radii)),samples);

for j=1:max(size(all_radii))
    clear pixel
    clear pixel_2
    radius = all_radii(j);
    x_c=rand(samples,1);
    y_c=rand(samples,1);
    for i=1:samples
        pixel(i,:) = pixel_hit_simulator(x_c(i),y_c(i),radius,n,extended
    );
        pixel_2(i,:) = pixel_hit_simulator(x_c(i),y_c(i),radius,n,
    extended);
        a_count_2=0;
        [dropletsizes(j,i),a_count_2] = dropletSizeSimulator( pixel(i,:)
    ./n,threshold_droplet,threshold_droplet_peak,extended );
```

```
23          [dropletsizes_2(j,i),a_count_2] = dropletSizeSimulator( (pixel(i
    ,:)+pixel_2(i,:))./n,threshold_droplet,threshold_droplet_peak,
    extended );
24          [dropletsizes_3(j,i),adu_counter] =
    dropletSizeSimulator_pileup2nd( pixel(i,:)./n,pixel_2(i,:)./n,
    threshold_droplet,threshold_droplet_peak,extended );
25          if adu_counter<=1
26              dropletsizes_3(j,i)=-1;
27          end
28      end
29      pixel = pixel./n;
30      % option to plot hitmap for pixel 1
31      % figure(771)
32      % plot(x_c,y_c,'b.')
33
34      % plot histograms with one px hit as if no droplet applied
35      figure(772)
36      subplot(max(size(all_radii)),2,2*j-1)
37      h=histogram(pixel,0.12:0.01:1);
38      yy=h.Values;
39      yy_all=sum(yy);
40      yy1=sum(yy(end-50:end));
41      xlim([0,inf])
42      title(sprintf('overlaps - %.2f',radius))
43      set(gca,'yscale','log')
44      ylim([0.9,100000])
45      subplot(max(size(all_radii)),2,2*j)
46      h=histogram(pixel(:,1),0.12:0.01:1);
47      yy=h.Values;
48      yy2=sum(yy(end-50:end));
49      xlim([0,inf])
```

```
50      title(sprintf('overlaps center px - %.2f',radius))
51      set(gca,'yscale','log')
52      ylim([0.9,100000])
53
54      % plot droplet simulation, compare droplet sizes
55      figure(773)
56      subplot(max(size(all_radii)),1,j)
57      x_val=-1.5:10.5;
58      h1=histogram(dropletsizes(j,:),x_val)
59      drops_1=h1.Values;
60      h2=histogram(dropletsizes_2(j,:),x_val)
61      drops_2=h2.Values/2;
62      h3=histogram(dropletsizes_3(j,:),x_val)
63      drops_3=h3.Values/2;
64      cla;
65      plot(x_val(1:end-1)+0.5,drops_1,'bo-','MarkerSize',5,'
    MarkerFaceColor','b')
66      hold on
67      plot(x_val(1:end-1)+0.5,drops_2,'ro-','MarkerSize',5,'
    MarkerFaceColor','r')
68      hold on
69      plot(x_val(1:end-1)+0.5,drops_3,'mo-','MarkerSize',5,'
    MarkerFaceColor','m')
70      legend('1 hit', '2 hit','droplet_pileup_2nd 2 hit')
71      title(sprintf('dropletsizes px -r: %.2f -extended: %i ',radius,
    extended))
72      set(gca,'yscale','log');
73      ylim([0.9,100000]); xlim([-1,11]);
74  end
```

A.2.2 Function pixel_hit_simulator

```
function pixel = pixel_hit_simulator(x_c,y_c,radius,n,extended)
xmax=1;
ymax=1;
r=abs(normrnd(0,radius,[n,1]));
theta=rand(n,1)*2*pi;
x=x_c+r.*cos(theta);
y=y_c+r.*sin(theta);
pixel(1) = size(x(x<=1*xmax & x>0*xmax & y<=1*ymax & y>0*ymax),1);
pixel(2) = size(x(x<=2*xmax & x>1*xmax & y<=1*ymax & y>0*ymax),1);
pixel(3) = size(x(x<=0*xmax & x>-1*xmax & y<=1*ymax & y>0*ymax),1);
pixel(4) = size(x(x<=1*xmax & x>0*xmax & y<=2*ymax & y>1*ymax),1);
pixel(5) = size(x(x<=1*xmax & x>0*xmax & y<=0*ymax & y>-1*ymax),1);
pixel(6) = size(x(x<=2*xmax & x>1*xmax & y<=2*ymax & y>1*ymax),1);
pixel(7) = size(x(x<=2*xmax & x>1*xmax & y<=0*ymax & y>-1*ymax),1);
pixel(8) = size(x(x<=0*xmax & x>-1*xmax & y<=2*ymax & y>1*ymax),1);
pixel(9) = size(x(x<=0*xmax & x>-1*xmax & y<=0*ymax & y>-1*ymax),1);
if extended
    pixel(10) = size(x(x<=3*xmax & x>2*xmax & y<=1*ymax & y>0*ymax),1);
    pixel(11) = size(x(x<=-1*xmax & x>-2*xmax & y<=1*ymax & y>0*ymax),1)
    ;
    pixel(12) = size(x(x<=1*xmax & x>0*xmax & y<=3*ymax & y>2*ymax),1);
    pixel(13) = size(x(x<=1*xmax & x>0*xmax & y<=-1*ymax & y>-2*ymax),1)
    ;
    pixel(14) = size(x(x<=3*xmax & x>2*xmax & y<=3*ymax & y>2*ymax),1);
    pixel(15) = size(x(x<=3*xmax & x>2*xmax & y<=-1*ymax & y>-2*ymax),1)
    ;
    pixel(16) = size(x(x<=-1*xmax & x>-2*xmax & y<=3*ymax & y>2*ymax),1)
    ;
```

```
25      pixel(17) = size(x(x<=-1*xmax & x>-2*xmax & y<=-1*ymax & y>-2*ymax)
        ,1);
26      pixel(18) = size(x(x<=3*xmax & x>2*xmax & y<=2*ymax & y>1*ymax),1);
27      pixel(19) = size(x(x<=3*xmax & x>2*xmax & y<=0*ymax & y>-1*ymax),1);
28      pixel(20) = size(x(x<=-1*xmax & x>-2*xmax & y<=2*ymax & y>1*ymax),1)
        ;
29      pixel(21) = size(x(x<=-1*xmax & x>-2*xmax & y<=0*ymax & y>-1*ymax)
        ,1);
30      pixel(22) = size(x(x<=2*xmax & x>1*xmax & y<=3*ymax & y>2*ymax),1);
31      pixel(23) = size(x(x<=2*xmax & x>1*xmax & y<=-1*ymax & y>-2*ymax),1)
        ;
32      pixel(24) = size(x(x<=0*xmax & x>-1*xmax & y<=3*ymax & y>2*ymax),1);
33      pixel(25) = size(x(x<=0*xmax & x>-1*xmax & y<=-1*ymax & y>-2*ymax)
        ,1);
34  end
```

A.2.3 Function dropletSizeSimulator_pileup2nd

```
1  function [ drop_size,adu_counter ] = dropletSizeSimulator_pileup2nd(
       pixel_1,pixel_2,threshold,threshold_peak,extended )
2  pixel_bool=pixel_1;
3  pixel_bool2=pixel_2;
4  orientation=[1,0;0,1;-1,0;0,-1];
5      if extended
6          pixel_bool_map_1=[pixel_bool(16),pixel_bool(24),pixel_bool(12),
       pixel_bool(22),pixel_bool(14);...
7              pixel_bool(20),pixel_bool(8),pixel_bool(4),pixel_bool(6),
       pixel_bool(18);...
```

```
8               pixel_bool(11),pixel_bool(3),pixel_bool(1),pixel_bool(2),
    pixel_bool(10);...
9               pixel_bool(21),pixel_bool(9),pixel_bool(5),pixel_bool(7),
    pixel_bool(19);...
10              pixel_bool(17),pixel_bool(25),pixel_bool(13),pixel_bool(23),
    pixel_bool(15)];
11          pixel_bool_map_2=[pixel_bool2(16),pixel_bool2(24),pixel_bool2
    (12),pixel_bool2(22),pixel_bool2(14);...
12              pixel_bool2(20),pixel_bool2(8),pixel_bool2(4),pixel_bool2(6)
    ,pixel_bool2(18);...
13              pixel_bool2(11),pixel_bool2(3),pixel_bool2(1),pixel_bool2(2)
    ,pixel_bool2(10);...
14              pixel_bool2(21),pixel_bool2(9),pixel_bool2(5),pixel_bool2(7)
    ,pixel_bool2(19);...
15              pixel_bool2(17),pixel_bool2(25),pixel_bool2(13),pixel_bool2
    (23),pixel_bool2(15)];
16          pixel_bool_map=zeros(9,9);
17          pixel_bool_map(3:7,3:7)=pixel_bool_map_1;
18          center2(1)=5; %allow no variation in y direction
19          center2(2)=ceil(rand(1)*5)+2;
20          pixel_bool_map(center2(1)-2:center2(1)+2,center2(2)-2:center2(2)
    +2)=pixel_bool_map_2+pixel_bool_map(center2(1)-2:center2(1)+2,
    center2(2)-2:center2(2)+2);
21          pixel_map=pixel_bool_map;
22          pixel_bool_map(pixel_bool_map<threshold)=0;
23          pixel_bool_map(pixel_bool_map>=threshold)=1;
24          center=[5,5];
25          counter=0;
26          adu_counter=0;
27          pixel_bool_map_copy=pixel_bool_map;
```

```
28          [ pixel_bool_map_copy , drop_size ,adu_counter ] = pixelWalker(
    pixel_bool_map_copy ,pixel_map , counter ,adu_counter , center ,
    orientation );
29      else
30          pixel_bool_map=[pixel_bool(8) ,pixel_bool(4) ,pixel_bool(6) ;...
31              pixel_bool(3) ,pixel_bool(1) ,pixel_bool(2) ;...
32              pixel_bool(9) ,pixel_bool(5) ,pixel_bool(7)];
33          pixel_bool_map_2=[pixel_bool2(8) ,pixel_bool2(4) ,pixel_bool2(6)
    ;...
34              pixel_bool2(3) ,pixel_bool2(1) ,pixel_bool2(2) ;...
35              pixel_bool2(9) ,pixel_bool2(5) ,pixel_bool2(7)];
36          pixel_bool_map=zeros(5,5);
37          pixel_bool_map(2:4,2:4)=pixel_bool_map_1;
38          center2(1)=3; %allow no variation in y direction
39          center2(2)=ceil(rand(1)*3)+2;
40          pixel_bool_map(center2(1)-1:center2(1)+1,center2(2)-1:center2(2)
    +1)=pixel_bool_map_2+pixel_bool_map(center2(1)-1:center2(1)+1,
    center2(2)-1:center2(2)+1);
41          pixel_map=pixel_bool_map;
42          pixel_bool_map(pixel_bool_map<threshold)=0;
43          pixel_bool_map(pixel_bool_map>=threshold)=1;
44          center=[3,3];
45          counter=0;
46                  adu_counter=0;
47          pixel_bool_map_copy=pixel_bool_map;
48          [ pixel_bool_map_copy , drop_size ,adu_counter ] = pixelWalker(
    pixel_bool_map_copy ,pixel_map , counter ,adu_counter , center ,
    orientation );
49      end
50  end
```

A.2.4 Function dropletSizeSimulator

```
function [ drop_size,adu_counter ] = dropletSizeSimulator( pixel,
    threshold,threshold_peak,extended )
pixel_bool=pixel;
pixel_bool(pixel>=threshold)=1;
pixel_bool(pixel<threshold)=0;
orientation=[1,0;0,1;-1,0;0,-1];
if pixel(1)>=threshold_peak
    if extended
        pixel_bool_map=[pixel_bool(16),pixel_bool(24),pixel_bool(12),
    pixel_bool(22),pixel_bool(14);...
            pixel_bool(20),pixel_bool(8),pixel_bool(4),pixel_bool(6),
    pixel_bool(18);...
            pixel_bool(11),pixel_bool(3),pixel_bool(1),pixel_bool(2),
    pixel_bool(10);...
            pixel_bool(21),pixel_bool(9),pixel_bool(5),pixel_bool(7),
    pixel_bool(19);...
            pixel_bool(17),pixel_bool(25),pixel_bool(13),pixel_bool(23),
    pixel_bool(15)];
        center=[3,3];
        counter=1;
        pixel_bool_map_copy=pixel_bool_map;
        pixel_bool_map_copy(center(2),center(1))=0;
        [ pixel_bool_map_copy, drop_size,adu_counter ] = pixelWalker(
    pixel_bool_map_copy,pixel_bool_map, counter,0, center, orientation )
    ;
    else
```

```
19          pixel_bool_map=[pixel_bool(8),pixel_bool(4),pixel_bool(6);...
20              pixel_bool(3),pixel_bool(1),pixel_bool(2);...
21              pixel_bool(9),pixel_bool(5),pixel_bool(7)];
22          center=[2,2];
23          counter=1;
24          pixel_bool_map_copy=pixel_bool_map;
25          pixel_bool_map_copy(center(2),center(1))=0;
26          [ pixel_bool_map_copy, drop_size,adu_counter ] = pixelWalker(
    pixel_bool_map_copy,pixel_bool_map, counter,0, center, orientation )
    ;
27      end
28  else
29      drop_size=0;
30  end
31  end
```

A.2.5 Function pixelWalker

```
1  function [ pixel_bool_map_copy, counter, adu_counter ] = pixelWalker(
       pixel_bool_map_copy, pixel_map, counter, adu_counter, center,
       orientation )
2  for i=1:size(orientation)
3      x=center(2)+orientation(i,2);
4      y=center(1)+orientation(i,1);
5      if x>0 && y>0 && x<=size(pixel_bool_map_copy,2) && y<=size(
       pixel_bool_map_copy,1)
6          if(pixel_bool_map_copy(y,x))
7              counter=counter+1;
8              adu_counter=adu_counter+pixel_map(y,x);
```

```
9                pixel_bool_map_copy(y,x)=0;
10               [ pixel_bool_map_copy, counter, adu_counter ] = pixelWalker(
     pixel_bool_map_copy, pixel_map, counter,adu_counter, [y,x],
    orientation);
11           end
12       end
13   end
14   end
```

Appendix B

Angular acceptance at different pulse energies

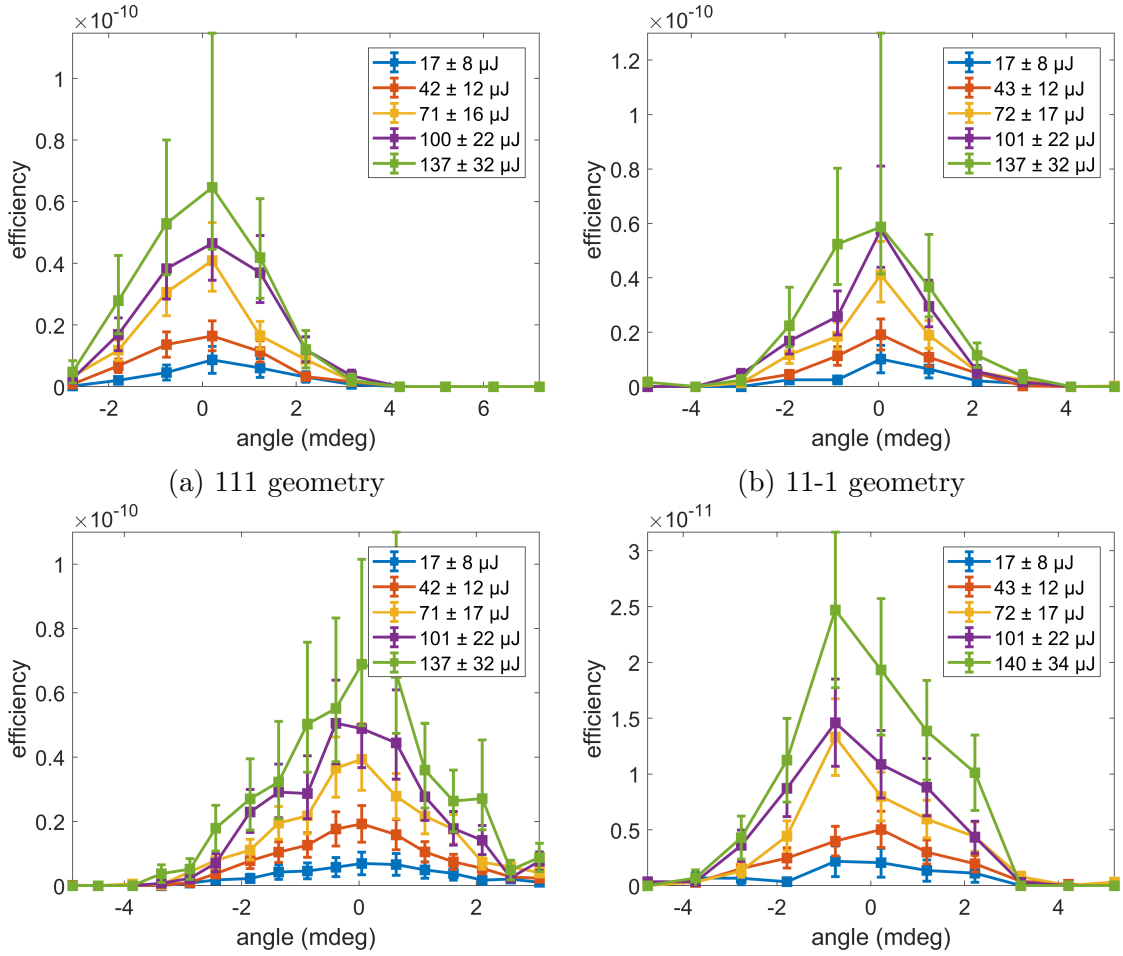

(a) 111 geometry

(b) 11-1 geometry

(c) 220 geometry

(d) 113 geometry

Figure B.1: rocking curves

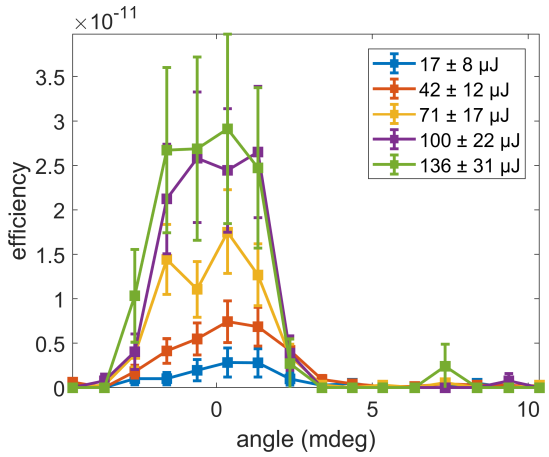

(a) 00-4 geometry

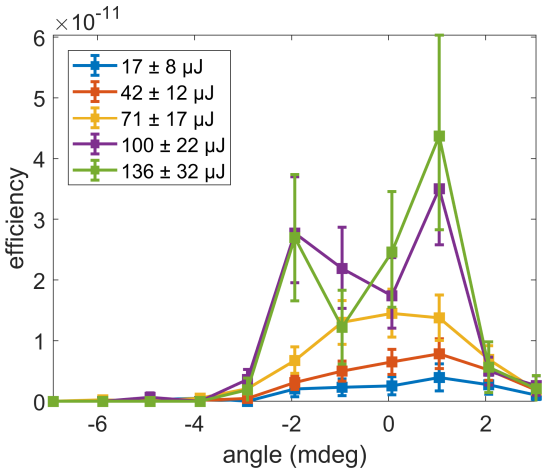

(b) 00-4 geometry

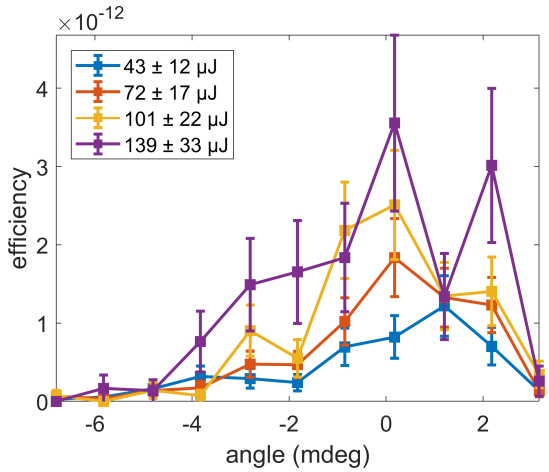

(c) 331 geometry

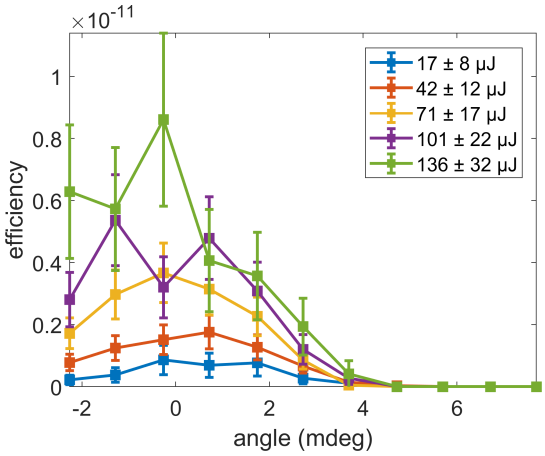

(d) 660 geometry

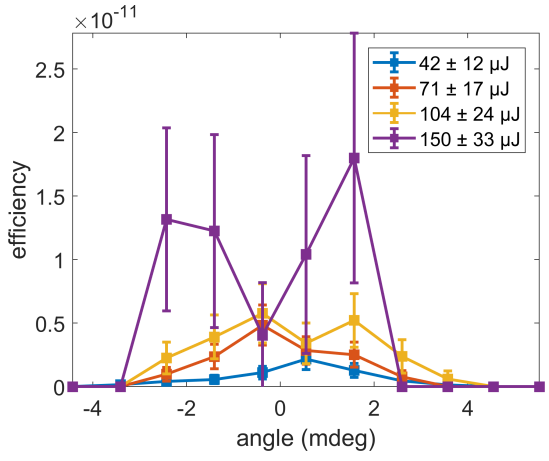

(e) 660 geometry

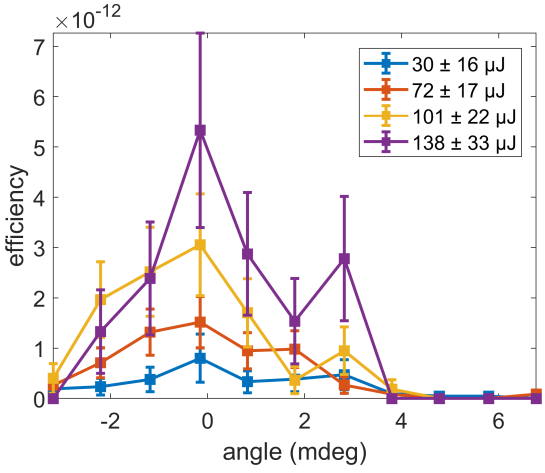

(f) 771 geometry

Figure B.2: rocking curves

Bibliography

[1] Canberra PIPS Detectors. http://www.canberra.com/literature/brochures/pdf/PIPS_Brochure_C47598.pdf.

[2] GITHUB: smalldata. https://github.com/slac-lcls/smalldata_tools.

[3] SLAC Confluence Common mode correction algorithms. https://confluence.slac.stanford.edu/display/PSDM/Common+mode+correction+algorithms.

[4] XPP Wiki. https://sites.google.com/site/xppwiki/.

[5] J. Als-Nielsen and D. McMorrow. *Elements of Modern X-ray Physics*. John Wiley & Sons, Inc., 2nd edition, 2011.

[6] J. Amann, W. Berg, V. Blank, F.-J. Decker, Y. Ding, P. Emma, Y. Feng, J. Frisch, D. Fritz, J. Hastings, Z. Huang, J. Krzywinski, R. Lindberg, H. Loos, A. Lutman, H.-D. Nuhn, D. Ratner, J. Rzepiela, D. Shu, Yu. Shvyd'ko, S. Spampinati, S. Stoupin, S. Terentyev, E. Trakhtenberg, D. Walz, J. Welch, J. Wu, A. Zholents, and D. Zhu. Demonstration of self-seeding in a hard-X-ray free-electron laser. *Nature Photonics*, 6(10):693–698, 2012.

[7] J. A. Arnaud, W. M. Hubbard, G. D. Mandeville, B. de la Clavière, E. A. Franke, and J. M. Franke. Technique for Fast Measurement of Gaussian Laser Beam Parameters. *Applied Optics*, 10(12):2775, 1971.

[8] H. R. Bilger and T. Habib. Knife-edge scanning of an astigmatic Gaussian beam. *Applied optics*, 24(5):686, 1985.

[9] G. Blaj, P. Caragiulo, G. Carini, S. Carron, A. Dragone, D. Freytag, G. Haller, P. Hart, J. Hasi, R. Herbst, S. Herrmann, C. Kenney, B. Markovic, K. Nishimura, S. Osier, J. Pines, B. Reese, J. Segal, A. Tomada, and M. Weaver. X-ray detectors at the Linac Coherent Light Source. *Journal of Synchrotron Radiation*, 22:577–583, 2015.

[10] G. Blaj, P. Caragiulo, A. Dragone, G. Haller, J. Hasi, C. J. Kenney, M. Kwiatkowski, B. Markovic, J. Segal, and A. Tomada. X-ray imaging with ePix100a: a high-speed, high-resolution, low-noise camera. In R. B. James, M. Fiederle, A. Burger, L. Franks, and S. A. Payne, editors, *Hard X-Ray, Gamma-Ray, and Neutron Detector Physics XVIII*, San Diego, California, United States, 2016.

[11] N. Bloembergen and P. S. Pershan. Light Waves At Boundary of Nonlinear Media. *Physical Review*, 128(2), 1962.

[12] M. Born and E. Wolf. *Principles of optics: electromagnetic theory of propagation, interference and diffraction of light*. Pergamon Press, Oxford, New York, 4th edition, 1970.

[13] C. Bostedt, S. Boutet, D. M. Fritz, Z. Huang, H. J. Lee, H. T. Lemke, A. Robert, W. F. Schlotter, J. J. Turner, and G. J. Williams. Linac Coherent Light Source: The first five years. *Reviews of Modern Physics*, 88(1), 2016.

[14] R. W. Boyd. Chapter 1 The Nonlinear Optical Susceptibility. In *Nonlinear Optics*, pages 1–67. 2008.

[15] R. W. Boyd. Chapter 2 Wave-Equation Description of Nonlinear Optical Interactions. In *Nonlinear Optics*, pages 69–133. 2008.

[16] W. H. Bragg and W. L. Bragg. The Structure of the Diamond. *Proceedings of the Royal Society of London. Series A*, 89(610):277 – 291, sep 1913.

[17] G. A. Carini, R. Alonso-Mori, G. Blaj, P. Caragiulo, M. Chollet, D. Damiani, A. Dragone, Y. Feng, G. Haller, P. Hart, J. Hasi, R. Herbst, S. Herrmann, C. Kenney, H. Lemke, L. Manger, B. Markovic, A. Mehta, S. Nelson, K. Nishimura, S. Osier, J. Pines, B. Reese, A. Robert, J. Segal, M. Sikorski, S. Song, J. Thayer, A. Tomada, M. Weaver, and D. Zhu. EPix100 camera: Use and applications at LCLS. In *AIP Conference Proceedings*, 2016.

[18] Gabriella Carini. personal communication.

[19] M. Chollet, R. Alonso-Mori, M. Cammarata, D. Damiani, J. Defever, J. T. Delor, Y. Feng, J. M. Glownia, J. B. Langton, S. Nelson, K. Ramsey, A. Robert, M. Sikorski, S. Song, D. Stefanescu, V. Srinivasan, D. Zhu, H. T. Lemke, and D. M. Fritz. The X-ray PumpProbe instrument at the Linac Coherent Light Source. *Journal of Synchrotron Radiation*, 22(3):503–507, 2015.

[20] J. E. Davis. Pile-up Fractions and Count Rates. *http://cxc.harvard.edu/csc/memos/files/Davis_pileup.pdf*, 2007.

[21] P. Eisenberger and S. L. McCall. X-ray parametric conversion. *Physical Review Letters*, 26(12):684–688, 1971.

[22] Y. Feng, J. M. Feldkamp, D. M. Fritz, M. Cammarata, R. Aymeric, C. Caronna, H. T. Lemke, D. Zhu, S. Lee, S. Boutet, G. Williams, K. Tono, M. Yabashi, and J. B Hastings. A single-shot intensity-position monitor for hard x-ray FEL

sources. In J. Dunn and A. Klisnick, editors, *X-Ray Lasers and Coherent X-Ray Sources: Development and Applications IX*. SPIE, sep 2011.

[23] P. A. Franken, A. E. Hill, C. W. Peters, and G. Weinreich. Generation of optical harmonics. *Physical Review Letters*, 7(4):118–119, 1961.

[24] M. Fuchs, M. Trigo, J. Chen, S. Ghimire, S. Shwartz, M. Kozina, M. Jiang, T. Henighan, C. Bray, G. Ndabashimiye, P. H. Bucksbaum, Y. Feng, S. Herrmann, G. A. Carini, J. Pines, P. Hart, C. Kenney, S. Guillet, S. Boutet, G. J. Williams, M. Messerschmidt, M. M. Seibert, S. Moeller, J. B. Hastings, and D. A. Reis. Anomalous nonlinear X-ray Compton scattering. *Nature Physics*.

[25] T. E. Glover, D. M. Fritz, M. Cammarata, T. K. Allison, S. Coh, J. M. Feldkamp, H. Lemke, D. Zhu, Y. Feng, R. N. Coffee, M. Fuchs, S. Ghimire, J. Chen, S. Shwartz, D. A. Reis, S. E. Harris, and J. B. Hastings. X-ray and optical wave mixing. *Nature*, 488(7413):603–8, 2012.

[26] J. M. Glownia, A. Natan, J. P. Cryan, R. Hartsock, M. Kozina, M. P. Minitti, S. Nelson, J. Robinson, T. Sato, T. van Driel, G. Welch, C. Weninger, D. Zhu, and P. H. Bucksbaum. Self-referenced coherent diffraction x-ray movie of ångstrom- and femtosecond-scale atomic motion. *Phys. Rev. Lett.*, 117:153003, Oct 2016.

[27] J. W. Goodman. *Speckle Phenomena in Optics: Theory and Applications*. Roberts & Company, 2007.

[28] S. P. Hau-Riege. *High-Intensity X-Rays - Interaction with Matter: Processes in Plasmas, Clusters, Molecules, and Solids*. Wiley-VCH Verlag GmbH & Co. KGaA, 2011.

[29] B.L. Henke, E.M. Gullikson, and J.C. Davis. X-Ray Interactions: Photoabsorption, Scattering, Transmission, and Reflection at E = 50-30,000 eV, Z = 1-92. *Atomic Data and Nuclear Data Tables*, 54(2):181–342, jul 1993.

[30] J. D. Jackson. *Classical Electrodynamics*. Wiley, 3rd edition, 1999.

[31] M. F. C. Ladd and R. A. Palmer. *Structure Determination by X-Ray Crystallography*. Plenum Press, New York and London, 2nd edition, 1985.

[32] B. F. Levine and I. Freund. Parametric down conversion of X-rays. *Optics Communications*, 1(9):419–422, 1970.

[33] T. H. Maiman. Stimulated Optical Radiation in Ruby. *Nature*, 187(4736):493–494, aug 1960.

[34] A. Marinelli, D. Ratner, A.A. Lutman, J. Turner, J. Welch, F.-J. Decker, H. Loos, C. Behrens, S. Gilevich, A.A. Miahnahri, S. Vetter, T.J. Maxwell, Y. Ding, R. Coffee, S. Wakatsuki, and Z. Huang. High-intensity double-pulse X-ray free-electron laser. *Nature Communications*, 6:6369, 2015.

[35] W. Massa. *Crystal Structure Determination*. Springer Berlin Heidelberg, Berlin, Heidelberg, 2nd edition, 2004.

[36] W. H. Miller and J. W. Parker. *A treatise on crystallography*. Printed at the Pitt Press, for J. & J.J. Deighton, Cambridge; London, 1839.

[37] M. P. Minitti, J. M. Budarz, A. Kirrander, J. S. Robinson, D. Ratner, T. J. Lane, D. Zhu, J. M. Glownia, M. Kozina, H. T. Lemke, M. Sikorski, Y. Feng, S. Nelson, K. Saita, B. Stankus, T. Northey, J. B. Hastings, and P. M. Weber. Imaging molecular motion: Femtosecond x-ray scattering of an electrocyclic chemical reaction. *Phys. Rev. Lett.*, 114:255501, Jun 2015.

[38] S. Moeller, J. Arthur, A. Brachmann, R. Coffee, F. Decker, Y. Ding, D. Dowell, S. Edstrom, P. Emma, Y. Feng, A. Fisher, J. Frisch, J. Galayda, S. Gilevich, J. Hastings, G. Hays, P. Hering, Z. Huang, R. Iverson, J. Krzywinski, S. Lewis, H. Loos, M. Messerschmidt, A. Miahnahri, H. Nuhn, D. Ratner, J. Rzepiela, D. Schultz, T. Smith, P. Stefan, H. Tompkins, J. Turner, J. Welch, B. White, J. Wu, G. Yocky, R. Bionta, E. Ables, B. Abraham, C. Gardener, K. Fong, S. Friedrich, S. Hau-riege, K. Kishiyama, T. Mccarville, D. Mcmahon, M. Mckernan, L. Ott, M. Pivovaroff, J. Robinson, D. Ryutov, S. Shen, R. Soufli, and G. Pile. Photon beamlines and diagnostics at LCLS. *Nuclear Instruments and Methods in Physics Research Section A: Accelerators, Spectrometers, Detectors and Associated Equipment*, 635(1):6 – 11, 2011.

[39] B. Nagler, U. Zastrau, R. R. Fäustlin, S. M. Vinko, T. Whitcher, A. J. Nelson, R. Sobierajski, J. Krzywinski, J. Chalupsky, Elsa. Abreu, S. Bajt, T. Bornath, T. Burian, H. Chapman, J. Cihelka, T. Döppner, S. Düsterer, T. Dzelzainis, M. Fajardo, E. Förster, C. Fortmann, E. Galtier, S. H. Glenzer, S. Göde, G. Gregori, V. Hajkova, P. Heimann, L. Juha, M. Jurek, F. Y. Khattak, A. R. Khorsand, D. Klinger, M. Kozlova, T. Laarmann, H. J. Lee, R. W. Lee, K.-H. Meiwes-Broer, P. Mercere, W. J. Murphy, A. Przystawik, R. Redmer, H. Reinholz, D. Riley, G. Röpke, F. Rosmej, K. Saksl, R. Schott, R. Thiele, J. Tiggesbäumker, S. Toleikis, T. Tschentscher, I. Uschmann, H.J. Vollmer, and J. S. Wark. Turning solid aluminium transparent by intense soft X-ray photoionization. *Nature Physics*, 2009.

[40] A. Nazarkin, S. Podorov, I. Uschmann, E. Förster, and R. Sauerbrey. Nonlinear optics in the angstrom regime: Hard-x-ray frequency doubling in perfect crystals. *Physical Review A*, 67(4):041804, 2003.

[41] Donald A. Neamen. Semiconductor Physics and Devices: Basics Aplications, 2012.

[42] Silke Nelson. personal communication.

[43] A. Rousse, C. Rischel, S. Fourmaux, I. Uschmann, E. Frster, P. Audebert, J. P. Geindre, J. C. Gauthier, and D. Hulin. Time-resolved femtosecond x-ray diffraction by an ultra-short pulse produced by a laser. *Measurement Science and Technology*, 12(11):1841, 2001.

[44] P. Schmüser, M. Dohlus, J. Rossbach, and C. Behrens. *Free-Electron Lasers in the Ultraviolet and X-Ray Regime - Physical Principles, Experimental Results, Technical Realization*. Springer Cham Heidelberg New York Dordrecht London, 2nd edition, 2014.

[45] Y.R. Shen. *Principles Of Nonlinear Optics*. J. Wiley, New York, 1984.

[46] S. Shwartz, M. Fuchs, J. B. Hastings, Y. Inubushi, T. Ishikawa, T. Katayama, D. A. Reis, T. Sato, K. Tono, M. Yabashi, S. Yudovich, and S. E. Harris. X-Ray Second Harmonic Generation. *Physical Review Letters*, 18, 2014.

[47] M. Sikorski, S. Song, A. Schropp, F. Seiboth, Y. Feng, R. Alonso-Mori, M. Chollet, H. T. Lemke, D. Sokaras, T. C. Weng, W. Zhang, A. Robert, and D. Zhu. Focus characterization at an X-ray free-electron laser by coherent scattering and speckle analysis. *Journal of Synchrotron Radiation*, 2015.

[48] Mark Sutton. personal communication.

[49] J. R. Taylor. *An Introduction to Error Analysis: The Study of Uncertainties In Physical Measurements*. University Science Books, 1997.

[50] R. W. Terhune, P. D. Maker, and C. M. Savage. Optical Harmonic Generation in Calcite. *Physical Review Letters*, 8(10):404 – 406, 1962.

[51] S. Yudovich and S. Shwartz. Second-harmonic generation of focused ultrashort x-ray pulses. *Journal of the Optical Society of America B*, 32(9):1894–1900, 2015.

[52] D. Zhu, Y. Feng, S. Stoupin, S. A. Terentyev, H. T. Lemke, D. M. Fritz, M. Chollet, J. M. Glownia, R. Alonso-Mori, M. Sikorski, S. Song, T. B. Van Driel, G. J. Williams, M. Messerschmidt, S. Boutet, V. D. Blank, Y. V. Shvyd'Ko, and A. Robert. Performance of a beam-multiplexing diamond crystal monochromator at the Linac Coherent Light Source. *Review of Scientific Instruments*, 85(6), 2014.

[53] Diling Zhu. personal communication.